MECHANOBIOLOGY OF CADHERIN-11 IN CALCIFIC AORTIC VALVE DISEASE

By

Meghan Allardyce Bowler

Dissertation

Submitted to the Faculty of the

Graduate School of Vanderbilt University

in partial fulfillment of the requirements

for the degree of

DOCTOR OF PHILOSOPHY

in

Biomedical Engineering

May 11, 2018

Nashville, Tennessee

Approved by:

W. David Merryman, Ph.D.

Craig L. Duvall, Ph.D.

Aron Parekh, Ph.D.

Albert B. Reynolds, Ph.D.

Matthew Walker III, Ph.D.

This work is dedicated to all animal research subjects, and especially the mice, pigs, and humans that directly contributed to this work.

ACKNOWLEDGEMENTS

I am indebted to my parents, Karen and Dennis Bowler, who have instilled in me the importance of education and especially the necessity of science and research. They have supported me emotionally and intellectually, and are still my go-to sounding boards. I would like to thank my brothers, Chris and Matt, for being such supportive and exceptional people. I am

grateful to my extended family for being present and thoughtful even though I am far away. I truly treasure the time we spend together. I wish to thank my friends, near and far, for their advice, for being interested in my work, for making complex schedules align, and for being invaluable humans that I get to know. I also need to thank Austin Oleskie for his incredible support emotionally and scientifically. I am so lucky you are in my life.

Finally, thank you, reader, for taking the time to peruse my work; I hope you take something valuable away from it.

TABLE OF CONTENTS

Page

Chapter

Appendix

LIST OF TABLES

LIST OF FIGURES

LIST OF ABBREVIATIONS AND ACRONYMS

Term	Description
5HT2B	5 Hydroxytryptamine Receptor 5B
ACE	Angiotensin Converting Enzyme
AFM	Atomic Force Microscopy
ALP	Alkaline Phosphatase
ANOVA	Analysis of Variance
αSMA	Smooth Muscle Alpha-Actin
AVECs	Aortic Valve Endothelial Cells
AVICs	Aortic VICs
aVICs	Activated VICs
BMP2	Bone Morphogenic Protein 2
BSA	Bovine Serum Albumin
CAVD	Calcific Aortic Valve Disease
CCB	Celecoxib
CDH1	Cadherin-1; E-cadherin
CDH2	Cadherin 2; N-cadherin
CDH5	Cadherin 5; VE-cadherin
CDH11	Cadherin-11; OB-cadherin
Chi3l1	Chitinase-3-Like Protein 1
CN	Calcific Nodule
COX2	Cyclooxygenase 2
DMC	Dimethyl Celecoxib
ECM	Extracellular Matrix
EDS	Energy-Dispersive X-Ray Spectroscopy
ELISA	Enzyme-linked Immunosorbent Assay
EMT	Endothelial to Mesenchymal Transformation
eNOS	Endothelial NO Synthase
ERK	Extracellular Signal-Regulated Kinase
ESEM	Environmental SEM
FACS	Fluorescence-Activated Cell Sorting
FGF-2	Fibroblast Growth Factor 2
GP130	Glycoprotein 130
GSK-3β	Glycogen Synthase Kinase-3 Beta
IL-6	Interleukin 6
JAKs	Janus Kinases
MVICs	Mitral VICs
NF-κB	Nuclear Factor Kappa-B
NO	Nitric Oxide
NOTCH1	Notch Homolog 1
obVICs	Osteoblastic VICs
OCT	Optimal Cutting Temperature
PAA	Polyacrylamide
PVICs	Pulmonary VICs
pVICs	Progenitor VICs

qVICs	Quiescent VICs
RANKL	Receptor Activator of NF-κB Ligand
RTKs	Receptor Tyrosine Kinases
SAVR	Surgical Aortic Valve Replacement
SEM	Scanning Electron Microscopy
STATs	Signal Transducers and Activators of Transcription
SYN0012	Monoclonal Antibody Against CDH11
TAVR	Transcatheter Aortic Valve Replacement
TEM	Transmission Electron Microscopy
TFM	Traction Force Microscopy
TGF-β1	Transforming Growth Factor Beta 1
TLR4	Toll-Like Receptor 4
TNFα	Tumor Necrosis Factor alpha
TVICs	Tricuspid VICs
VICs	Valve Interstitial Cells
V_{max}	Aortic Valve Peak Velocity
YAP1	Yes-Associated Protein 1

CHAPTER 1

Introduction and Motivation

1.1 – Calcific Aortic Valve Disease Prevalence and Cost

Prevalence of valvular disease increases with age, affecting ~12% of the total population over 75 and responsible for over 25,000 deaths in 2015 in the US alone. Aortic stenosis accounts for ~65% of those deaths and moderate to severe stenosis has an estimated prevalence of ~3% for those over 75 [1, 4]. Aortic stenosis is the narrowing of the aortic valve opening, which restricts blood flow and thus, causes the heart to work harder. The number of patients with calcific aortic stenosis is expected to double by 2050 and possibly triple by 2060 [5, 6]. Aortic stenosis is primarily caused by calcific aortic valve disease (**CAVD**), which encompasses the disease spectrum – from initiation through sclerosis to stenosis. Aortic sclerosis is defined as the thickening and calcification of an aortic valve without restricting blood flow. Aortic sclerosis affects 25% of those over 65 in the United States, making this a widespread problem [7]. The high prevalence of valve disease results in a multitude of hospital visits and costly procedures. Totals in 2013 were over 100,000 procedures at an average cost of $51,415, for a total monetary cost upwards of $5.2 billion [1]. These mortality and cost burdens motivate new solutions to prevent and treat CAVD.

1.2 – Calcific Aortic Valve Disease Treatment

CAVD progresses quickly from aortic sclerosis to aortic stenosis, with an approximated rate of progression of ~2% per year [8]. Currently, the only treatment available is total valve replacement, which necessitates surgery, an intervention fraught with complications especially for the older patient population that CAVD disproportionally affects [1]. Historically, this meant open-chest surgery, but recently, a minimally invasive approach has gained traction. Transcatheter aortic valve replacement (**TAVR**) deploys a bioprosthetic valve to replace the aortic valve without removing the patient's valve. The bioprosthetic, made of decellularized porcine or bovine valves, is collapsed in a catheter that can be delivered through the femoral artery or through a small incision in the chest and the heart apex. When the replacement valve is deployed, it pushes the calcified leaflets to the sides of the outflow tract, allowing blood flow throughout the procedure. TAVR has been associated with approximately four-day-shorter hospital stays and improved quality of life at one month post-operation compared to surgical valve replacement with thoracotomy [1]. This procedure has been approved for patients that are considered intermediate or high risk for the surgical intervention, thereby providing treatment for an otherwise untreatable population [9].

Before TAVR, the only option was surgical aortic valve replacement (**SAVR**), which involves implantation of a mechanical or bioprosthetic valve through a port or open-chest

Figure 1.1 – Aortic valve surgeries. TAVR procedures are slightly more common than SAVR, but both are far more common in adults than the Ross procedure [1-3].

surgery. Mechanical valves are durable but require continuous use of anticoagulants to prevent clot formation and the subsequent potential for myocardial infarction or stroke. This is not ideal because anticoagulants increase the risk of bleeding events, like a hemorrhagic stroke. Bioprosthetic valves do not require anticoagulants but have a reduced lifetime of approximately 10-20 years. In general, bioprosthetic valves are the typical choice, especially in aged populations [1].

The least common replacement surgery is the Ross technique. It involves the replacement of a patient's aortic valve with their own pulmonary valve. This is especially attractive for pediatric patients, as the pulmonary valve is able to grow and remodel with the child. The pulmonary valve is then typically replaced with a donor valve, which tends to last longer than if it were in the aortic position because the valve in the pulmonary position is under less mechanical stress than the valve in the aortic position. However, for adults, the complications of the procedure usually outweigh the benefit of longer valve lifetime.

Unfortunately, no preventative therapies or alternative pharmaceutical therapeutics are available, largely because the molecular mechanism of CAVD is poorly understood. Some of the earliest therapeutics evaluated were angiotensin-converting enzyme (**ACE**) inhibitors and statins, or HMG-CoA reductase inhibitors, a class of lipid-lowering medications. Results from statin studies were conflicting [10-12], prompting the large randomized, controlled trial, Simvastatin and Ezetimibe in Aortic Stenosis (SEAS). Unfortunately, this study found no significant effect of statin treatment on aortic stenosis progression and a higher incidence of cancer in stenotic patients treated with statins [13]. There was also debate over the effectiveness

of angiotensin converting enzyme (**ACE**) inhibitors [14]. However, a double-blind, randomized controlled trial, Ramipril In Aortic Stenosis (RIAS), demonstrated a modest reduction in left ventricular mass and trends toward slower stenosis [15]. Further validation in the form of a larger trial is required, but ACE inhibitors hold some promise. Genetic studies have recently identified lipoprotein(a) as a potential driver of aortic stenosis [16], motivating an early phase 1 trial (EAVaLL) to reduce the levels of lipoprotein(a) via Niacin in patients with aortic sclerosis or mild stenosis [17]. Though we are making progress in the prevention or slowing of aortic stenosis, we have not yet identified a strategy that yields conclusive improvement.

1.3 – Calcific Aortic Valve Disease Evaluation

Assessment of cardiac valves relies largely on echocardiography. It is cost-effective, portable, accessible, and usually provides enough information for therapy planning, though it depends on the skill of the technician. Magnetic resonance imaging allows quantification and better visualization of the valves, especially in patients with poor acoustic windows, but is less accessible and cannot be used in patients with contraindications, such as pacemakers. Computed tomographic angiography has been investigated as an imaging modality, but the improved visualization and anatomic evaluation of the valves are not usually worth the ionizing radiation required [18].

In addition to imaging, biomarkers are important diagnostic tools but are lacking for aortic stenosis. A robust serum biomarker could provide physicians with a tool to easily screen and track patients without the need for more than a routine blood draw. In a study of 60 patients with aortic stenosis and 20 without, calcification was found to positively correlate with serum matrix

metalloproteinase 2, matrix metalloproteinase 9, tumor necrosis factor alpha (**TNFα**), transforming growth factor β1 (**TGF-β1**), tenascin C, interleukin-2, sclerostin, osteopontin, osteoprotegerin, monocyte chemoattractant protein 1, and malondialdehyde, and negatively correlate with serum tissue inhibitor 1 of metalloproteinase, fetuin-A, and relaxin 2 [19]. Other studies have found correlation between calcification and elevated levels of B-type natriuretic peptide (compared to the expected value for age and gender or from 30 days prior), lipoprotein(a) and low-density lipoprotein-C, phosphate, leptin, tissue plasminogen activator, calcium phosphorus, and asymmetric dimethylarginine [20]. However, there are also studies that have found no relationship between stenosis progression and LDL [21] and conflicting data surrounding C-reactive protein [22, 23] and fetuin-A [24]. We clearly do not have a definitive serum biomarker for CAVD progression. At this point, the best we can do is choose some combination of these relationships and hope that they are specific enough to monitor calcification. Alternatively, further research may reveal a robust biomarker associated primarily with stenosis.

1.4 – Dissertation Overview

This clinical need has motivated my work, presented in the following thesis. Chapter 1 focuses on the burden of CAVD and lack of treatment and tracking strategies, motivating a deeper understanding of disease progression to identify methods of tackling these challenges. Chapter 2 is background information on what is currently known about disease progression, the aortic valve interstitial cells (**AVICs**) thought to mediate it, the initiators of disease, and the key signaling that the rest of the work involves. Chapter 3 addresses the role of cadherin-11 (**CDH11**) in CAVD caused by NOTCH1 mutation *in vivo* and provides motivation for understanding the

mechanism by which targeting CDH11 prevents CAVD. Chapter 4 delves into the effects of CDH11 on AVIC biology, characterizing phenotypes caused by genetic deletion and overexpression of CDH11. Chapter 5 examines the role of inhibiting cyclooxygenase-2 (**COX2**) versus blocking CDH11 on disease progression. Chapter 6 compares valve interstitial cells (**VICs**) from all four cardiac valves to gain insight into the cause of preferential aortic valve calcification. Chapter 7 details a genetic tool designed to isolate the effects of CDH11 from any compensatory mechanisms that have developed in AVICs isolated from mice after two months. Finally, Chapter 8 summarizes the impact of this work and contribution to society followed by suggestions for future studies. Overall, this project focuses on the mechanobiology of CDH11 in CAVD and the AVICs that mediate its progression.

CHAPTER 2

Background

Text for Chapter 2 was adapted from <u>Bowler MA</u> and Merryman WD. In vitro models of aortic valve calcification: solidifying a system. *Cardiovascular Pathology*. 24 (2015): 1-10. [25]

2.1 – Aortic Valve Development, Anatomy, and Disease

The aortic valve is a thin, tri-leaflet structure located at the base of the aortic root at the most distal portion of the left ventricular outflow tract. Functionally, the aortic valve serves to mediate the unidirectional flow of blood during the cardiac cycle, allowing flow from the left ventricle to the systemic vasculature during systole, and shutting to prevent backflow during diastole. The structure of the aortic valve is vital to maintaining its function. Human aortic valves consist of three histologic layers: 1) the fibrosa, which faces the aorta and is composed mostly of type I fibrillar collagen arranged circumferentially in parallel bundles in a matrix of elastin; 2) the spongiosa, which is the middle layer and is composed of glycosaminoglycans that act as shock absorbers for the valve; and 3) the ventricularis, which faces the left ventricle and is primarily composed of elastin fibers oriented radially [26].
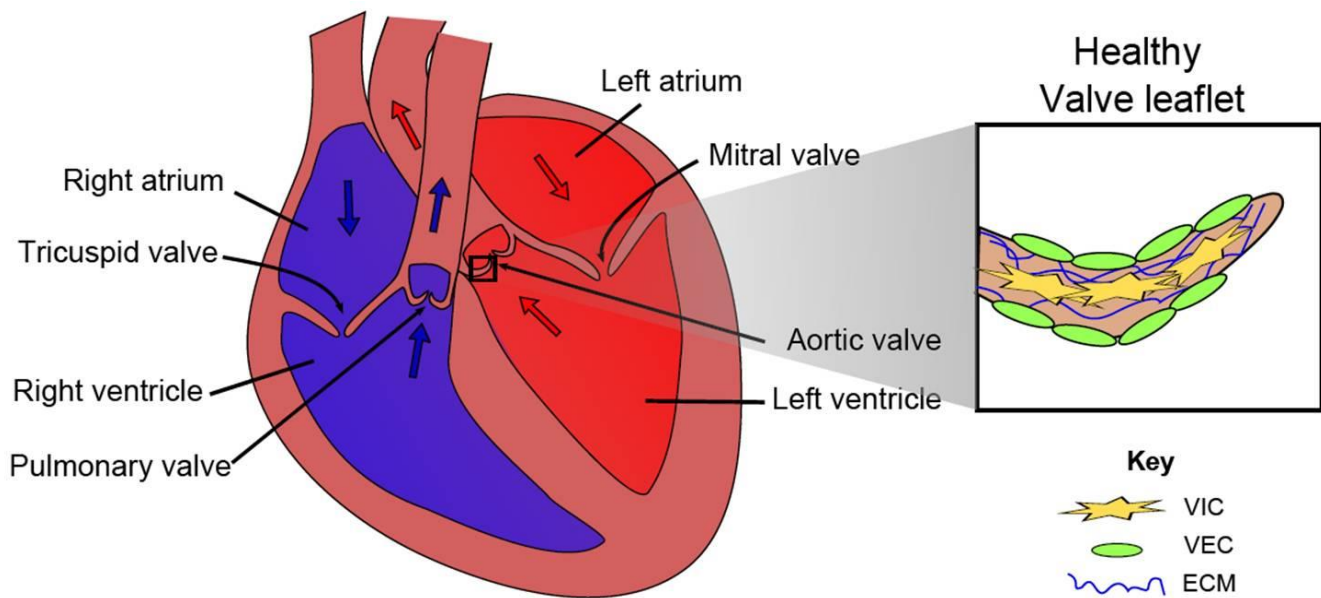
Figure 2.1 – Human heart and aortic valve leaflet anatomy. Adapted from Schroer AK and Merryman WD. Mechanobiology of myofibroblast adhesion in fibrotic cardiac disease. *Journal of Cell Science.* 128 (2015): 1865-75 [27].

Late stage CAVD is marked by obstruction of blood flow and aortic stenosis and has an estimated prevalence of 2% in patients between 70 and 80 years of age [28]. Prevalence of any aortic valve calcification is as high as 48% for those aged 75-76, and higher in 80–81 and 85–86 year-old cohorts [29]. The incidence of this age-related disease is expected to grow dramatically in the next 25 years as the proportion of people over 65 in the United States nearly doubles [30]. Calcific aortic valve stenosis is the main indication for the over 100,000 valve replacements performed annually in the US and necessitates surgical intervention [31], which is currently the only therapeutic option [32]. Unfortunately, given the advanced age of many CAVD patients, this intervention carries with it a high rate of morbidity and mortality and is therefore not recommended in elderly or fragile patients, leaving many to suffer the ill effects of progressively worsening heart function as CAVD advances [33]. A better understanding of the biological mechanism driving the valvular calcification process might allow us to develop well-tolerated, non-invasive pharmacologic therapies.

Once believed to be a passive process of degeneration, aortic valve calcification is now thought to be an active process of valvular remodeling mediated largely by the valve's resident cells, AVICs [34]. AVICs are a heterogeneous population of fibroblast-like cells present in all three layers of the aortic valve and important in the structural maintenance of the valve, especially in the maintenance of the extracellular matrix (**ECM**) [35, 36]. Gross pathologic progression of CAVD is characterized by the formation of calcific nodules (**CNs**), which are cellular aggregates comprised of a mixture of calcium phosphate phases [37]. Two hypothetical mechanisms of CN formation exist: 1) TGF-β1 mediates activation of myofibroblasts, causing dystrophic calcification via apoptotic mechanisms [38], and 2) a population of AVICs spontaneously transdifferentiate into osteoblast-like cells and subsequently regulate mineralization (Figure 2.2) [39, 40]. In a study of human valves, 83% of the group demonstrated evidence of dystrophic calcification and 13% of those valves had mature lamellar bone and evidence of active bone remodeling [41]. It is unclear whether these processes occur simultaneously, sequentially, or independently. Therefore, we will selectively focus on elucidating the mechanism of the more prevalent dystrophic pathway [42].
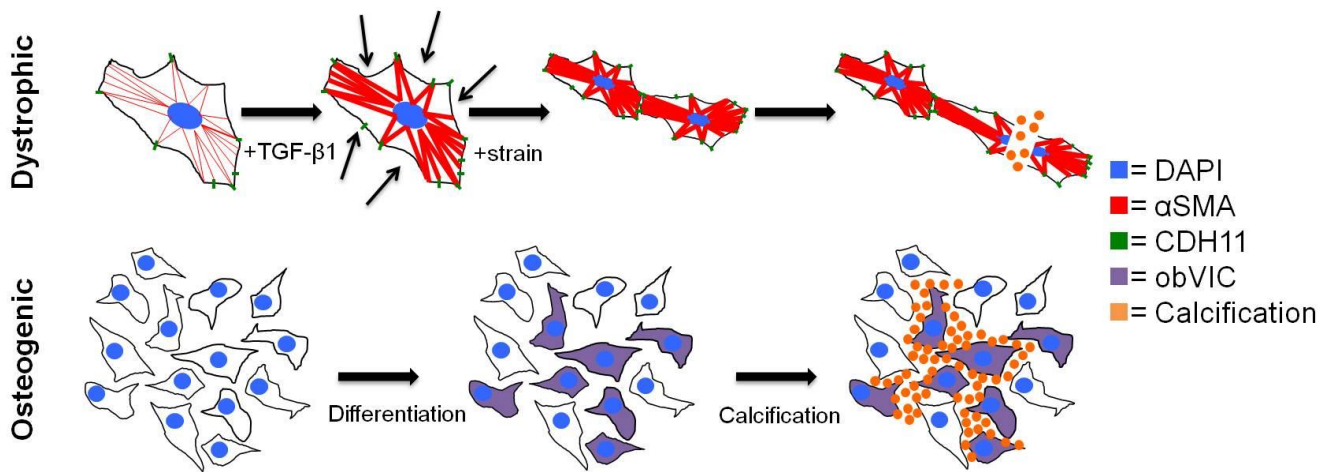
Figure 2.2 – Proposed mechanisms of valve calcification. The dystrophic pathway is mediated by a TGF-β1 induced increase in αSMA and cadherin-11, which increases the cells' contractility and strengthens their connections to each other. Under pathological strain, the increased and uneven tension tears cells apart, leading to calcification via apoptosis. The osteogenic pathway proceeds by osteogenic differentiation into obVICs, likely from qVICs. These obVICs actively form mineralized deposits. Adapted from Bowler MA and Merryman WD. In vitro models of aortic valve calcification: solidifying a system. *Cardiovascular Pathology.* 24 (2015): 1-10. [25]

As a human ages, the aortic valve remodels: AVIC density and proliferation decrease, elastin content increases, and collagen fibers become more aligned. In CAVD, however, elastin is fragmented and overall content is decreased, while collagen content increases and becomes disorganized, contributing to valve leaflet thickening [43]. Remodeling of the ECM and subsequent stiffening that is characteristic of CAVD have been shown to regulate cellular processes [44]. For example, AVICs cultured in the presence of TGF-β1 on type I fibrillar collagen gels, fibrin-coated tissue culture plastic, or hydrogels of ~25 kPa formed osteogenic CNs, whereas nodules on ~120 kPa formed through the dystrophic pathway via myofibroblastic differentiation [45, 46]. This suggests that after the initiation of disease, a positive feedback between activation of AVICs and substrate stiffness exacerbates disease progression, at least in the case of dystrophic remodeling.

CDH11 and smooth muscle alpha-actin (**αSMA**) are two mechanically active proteins involved in dystrophic calcification. CDH11, a mechanosensitive transmembrane protein involved in cell-cell adhesion, is thought to be responsible for mediating much of the intercellular tension integral to the dystrophic pathway [47], and αSMA is involved in cell motility and intracellular contractility [48]. When these proteins are upregulated in the diseased state, individual AVICs experience increased and regionally heterogeneous tension and contraction, resulting in membrane tearing and apoptosis-mediated calcification. This cell death provides increased imbalance in cellular forces and a local increase in substrate stiffness, acting as a nucleation event in the formation of a CN [47, 49].

Both CDH11 and αSMA are overexpressed in diseased human valves, though previous *in vitro* work suggests that their relative expression levels are inversely regulated at the level of individual cells [50]. While cadherins are known to complex with a family of mechanical adapter proteins called catenins intracellularly, further downstream signaling events are poorly understood. A better understanding of CDH11 signaling and activation, and how it interacts with contractile proteins to mediate CNs, could uncover potential therapeutic targets for CAVD.

2.2 – Contribution of Aortic Valve Interstitial Cells to Calcific Aortic Valve Disease

Since the AVIC population is heterogeneous, the various subpopulations may contribute to CAVD pathogenesis differently depending on their function. While a definitive categorization of AVICs subpopulations has remained elusive, recent efforts to classify AVICs based on their observed phenotypic behavior has yielded five groups: embryonic progenitor

endothelial/mesenchymal cells, quiescent VICs (**qVICs**), activated VICs (**aVICs**), progenitor VICs (**pVICs**), and osteoblastic VICs (**obVICs**) [51]. VICs predominantly come from a population of endocardial cells lining the endocardial cushion which undergo endothelial to mesenchymal transformation (**EMT**) early in embryonic development. These cells are crucial in valve development and there is evidence that these progenitors participate in adult valve repair [51]. qVICs are responsible for maintaining physiological valve structure and function. While the exact function of qVICs is undefined, they are believed to regulate ECM homeostasis and inhibition of angiogenesis [51]. pVICs are considered valve stem cells and they are likely responsible for VIC proliferation in response to tissue injury. pVICs may originate from aortic valve endothelial cells (**AVECs**) that undergo an EMT-like process [51-53]. These EMT-related events are likely directly mediated by the mechanical forces present in the valve. In a recent study using chick explanted atrioventricular canals, EMT was found to occur preferentially in higher regions of strain [54]. This developmental process is likely recapitulated in an unregulated fashion during CAVD progression. This suggests that as the valve stiffens, more AVECs are transformed into pVICs and qVICs, setting the stage for subsequent activation.

aVICs are qVICs that have become myofibroblasts, characterized by αSMA expression and increased contraction. This activation occurs under pathological injury cues or abnormal mechanical stress via cytokines and growth factors produced by activated AVECs and macrophages [51]. aVICs are associated with increased ECM secretion and degradation, matrix metalloproteinase and tissue inhibitor of metalloproteinase expression, proliferation and migration, and secretion of cytokines including TGF-β1. If apoptotic pathways become abnormal, aVICs can lead to calcification; this is referred to as the dystrophic pathway. obVICs are VICs that have undergone osteoblastic differentiation and promote calcification *in vitro*. The addition

12

of organic phosphate to culture media induces this differentiation and subsequent calcification depends on the upregulation of alkaline phosphatase (**ALP**) activity. Adding bone morphogenic protein 2 (**BMP2**) and 25-hydroxycholesterol increases the rate of CN formation, as does TGF-β1, which induces calcification via an apoptotic mechanism [55]. BMP2 has been shown to be higher in stenotic human aortic valves [56] and upregulates osteogenic pathways involving Msx2 and Wnt signaling [57] and Runt-related transcription factor 2/core-binding factor subunit alpha-1 (Runx2/CBFα1) [58]. It is likely that AVECs are regulating aVIC or obVIC function and that, given the presence *in vivo* of both BMP2 and TGF-β1, a combination of osteogenic and dystrophic pathways is occurring. Therefore, we are most concerned with the transitions to and behavior of obVICs and especially aVICs.

Porcine aortic VICs have also been categorized by morphology *in vitro*. After clonal expansion, Chen et al. defined four major subpopulations of VICs: 1) S-type are tightly connected, swirling fibroblast-like cells enriched for osteogenic progenitors (defined by presence of ALP in CNs), 2) loosely-packed fibroblast-like cells, 3) small, flat cells, and 4) large, flat cells [59]. More quantitative characterization of these subtypes was performed on porcine AVICs and pulmonary VICs (**PVICs**) via fluorescence-activated cell sorting (**FACS**). The percentage of VICs expressing most markers probed did not differ between AVIC and PVIC populations, though PVICs did express more SSEA4 (a marker of human embryonic stem cells, or pVIC-like) [60]. These characterizations may correlate well with some of the previously defined VIC subpopulations, but the contribution of CDH11-expressing VICs to calcification is unknown.

While AVICs are the primary cell type implicated in CAVD pathogenesis, it is likely that several other distinct native and non-native cell populations also play important roles. AVECs

sheath the surface of the leaflets and are oriented circumferentially and form a single cell monolayer, expressing Von Willebrand factor and nitric oxide (**NO**) [61-63]. Circulating cells have recently been implicated in the progression of calcification as well; elevated levels of endothelial progenitor cells with an osteoblastic phenotype and osteogenic precursor cells have been associated with severe and early heterotopic ossification, respectively [64, 65]. Early stages of CAVD develop lesions similar to those observed in atherosclerosis, suggesting a role for inflammatory signaling [66, 67]. Consistent with this observation are regularly observed elevated levels of macrophages and T-lymphocytes in human calcified aortic valves [41, 44, 68, 69]. These cell populations all contribute to CAVD progression, but it is likely that they influence AVIC behavior through the secretion of various bioactive agents.

2.3 – The Appropriate Model Organism

The ideal *in vitro* model would use primary human AVICs, but availability is the chief limiter of using human-derived samples. The next best cell would retain all characteristics of the human cells important to CAVD. Since it is believed that the important mediators of calcification are AVICs, we can narrow our search to finding a species with AVICs comparable to human AVICs.

Non-human primates are a logical choice because of their genetic similarity. However, maintenance of these organisms requires more space, time, money, and permissions than other organisms. Likely for these reasons, non-human primate AVICs have not been isolated, though *Macaca nemestrina* aortic smooth muscle cells have been isolated to investigate proteoglycan expression [70]. Porcine hearts are both anatomically and physiologically similar to human hearts. The growth of the heart in swine from birth to four months is analogous to that in humans

from birth to mid-teens [71] and remodeling in atherosclerosis of micropigs closely resembles human pathology [72]. Interestingly, their valves contain the same αSMA-positive population of cells in the ventricularis [35]. Swine can also develop spontaneous valvular atherosclerotic lesions, a precursor to calcification [40, 73]. The first isolation of porcine AVICs noted that they appear more homogenous than murine or leporine VICs and had a high recovery rate after being frozen, leading to the extensive use of porcine AVICs in *in vitro* studies [74]. Though these cells are widely used and multiple research groups have reported calcification and mineralization, Cloyd et al. reported that porcine AVICs cultured in osteogenic media with TGF-β1 (which should activate both dystrophic and osteogenic pathways) did not form mineral deposits. They used Raman spectroscopy to show that even Alizarin Red-positive nodules did not exhibit mineralization [37]. While pig anatomy is highly similar to human anatomy, porcine AVICs *in vitro* is still a limited model. One important limitation specific to *in vitro* cell culture systems is the age of the cells. In 20% of long-term cell culture, AVICs become contact-inhibited monolayers and behave unstably [75]. Also, the metabolic activity of porcine AVICs was found to be passage number dependent [76]. Late-stage cultured AVICs demonstrated higher numbers of myofibroblasts [77, 78]. Thus, porcine AVICs are generally used no later than passage 7. Though porcine AVICs have limitations, they are the best available model.

Ovine AVICs have been shown to form CNs when treated with TGF-β1 within 72 hours, and to calcify, assayed via Alizarin Red staining, within two weeks [38, 79]. Canine AVICs were also considered early in the development of CAVD research [55]. Specifically, beagles demonstrate age-related changes in aortic valves, including calcification; changes were especially apparent in the fibroblasts, suggesting a similar mechanism to human calcification [80]. *In vitro*, canine AVICs spontaneously formed CNs containing hydroxyapatite over two to three weeks, compared to human AVICs developing nodules in about six weeks under the same

conditions [55]. Also, while an imperfect model, many similarities exist between canine and human myxomatous mitral valve disease, reinforcing the likeness between human and canine valves [81]. While canine AVICs were deemed very similar to humans', they are not often used, likely as a function of convenience – dogs have longer life spans than small animal models and are not maintained at a large scale for another purpose, as pigs are for food. Rabbits are used for *in vivo* studies, but not as often *in vitro*, likely because they require high cholesterol diets to develop calcification [32, 82-84].

Mice are another popular model organism, perhaps because of their low cost, easy management, short life spans, and availability of genetic mutants. Murine cell lines can be easily immortalized, allowing for near indefinite expansion and use without regard for passage limitations. AVICs could be harvested from a variety of genetically-altered models such as ApoE$^{-/-}$, Notch1$^{+/-}$, and LDLr$^{-/-}$ [40, 85-90]. Though some of these models are the only ones to exhibit the hemodynamic effects of aortic valve stenosis, murine valvular structure is significantly different from human [40, 91]. Specifically, human valves have trilaminar structure, but murine valves only have a fibrosa and spongiosa [91]. While non-ideal, murine AVICs would provide a convenient model that facilitates genetic manipulation allowing for further exploration of CAVD mechanisms. A summary of the advantages and limitations of the AVICs derived from each model organism can be found in Table 2.1.

Table 2.1 – Examination of advantages and disadvantages associated with AVICs derived from common model organisms.

Organism	How are its AVICs useful?	Why are they imperfect?	Who has used these AVICs?
Human	Most appropriate	Difficult to obtain	[44, 55, 58, 92-100]
Porcine	Similar anatomy to human; easy to obtain; swine spontaneously develop calcification precursors	More homogenous than human	[36, 37, 42, 45-48, 73, 76-78, 101-112]
Ovine	CNs develop more quickly than human	More difficult to obtain than porcine	[38, 79, 113-115]
Canine	CNs develop more quickly than human; pathology naturally occurs	Difficult to obtain; require ageing	[55]
Leporine	Many osteogenic markers upregulated; easy to obtain	Require high cholesterol diets over time	

2.4 – Biochemical Cues Relevant to Calcific Aortic Valve Disease

A number of cytokines are known to modulate AVIC behavior, including inducing disease progression *in vitro*. Activation of the Wnt signaling pathway, involving Wnt3a, Wnt7a, and nuclear translocation of β-catenin, has been shown to promote calcification [116]. Wnt receptor LRP5 and β-catenin, factors in canonical Wnt signaling, also showed increased expression in diseased human aortic valves [117]. Both TGF-β1 and substrate stiffness have been shown to regulate signaling through MAPKs, p38 and extracellular signal-regulated kinase (**ERK**), both of which have been shown to promote the myofibroblast phenotype [118]. TNFα, interleukin1-β, and interleukin-6 (**IL-6**) have been shown to regulate Notch signaling [119], which enhances toll-like receptor 4 (**TLR4**) stimulation in human AVICs via nuclear factor kappa-B (**NF-κB**) [99]. Interestingly, IL-6 has been shown to be upregulated by CDH11 engagement [120]. In human AVICs, TNFα has been shown to accelerate calcification, assayed via ALP activity, Alizarin Red, and von Kossa [98]. Silencing TLR4 attenuates BMP2 expression, and stimulating TLR2 or TLR4 induces CN formation in human AVICs [97]. Receptor activator of NF-κB ligand (**RANKL**), a

surface-bound molecule of the TNF family, has also led to increased calcification *in vitro* [94, 121]. Together, these data support a role for inflammatory signaling in CAVD progression.

Porcine AVECs are able to inhibit AVIC calcification via NO secretion, inhibiting the differentiation to obVICs. Increasing the expression and activity of endothelial NO synthase (**eNOS**) in hypercholesterolaemic leporine aortic valves led to decreased calcification [122]. Additionally, blocking NO led to increased calcification even in 3D AVEC-AVIC co-culture [109]. *Ex vivo* culture of porcine aortic valve cusps in osteogenic media demonstrated significantly more CN formation on the fibrosa side than the ventricularis, which was exacerbated with NO inhibition. In healthy human valves, eNOS levels are much higher on the ventricularis than the fibrosa, further supporting the important protective effect of NO [109].

TGF-β1 is upregulated in diseased human valves and, when given exogenously *in vitro*, exacerbates nodule formation [38]. TGF-β1 has been shown to activate myofibroblasts in valves leading to increased αSMA expression via Smads and p38 [107, 123]. As these myofibroblasts become more contractile, they likely activate latent TGF-β1 from the ECM [124]. This positive feedback loop provides a strong potential mechanism for dystrophic disease progression. Some experiments have shown that fibroblast growth factor 2 (**FGF-2**) treatment can block nodule formation and matrix contraction of AVICs, effectively counteracting TGF-β1 treatment [79]. In addition, antagonism of 5 hydroxytryptamine receptor 2B (**5HT2B**), a TGF-β1-dependent cardiopulmonary serotonin receptor, has been shown to prevent myofibroblast differentiation and CN formation in porcine AVICs by inhibiting downstream TGF-β1-mediated signaling [123]. Another recent strategy is to target CDH11, a protein believed to mediate cell-cell tension in

CAVD and that has higher expression in calcified human valves; siRNA knockdown of CDH11 *in vitro* prevented TGF-β1-mediated CN formation [47].

2.5 – Mechanical Environment of the Aortic Valve

Many traditional CAVD *in vitro* studies have occurred in a static environment, but the valves exist in a dynamic mechanical state; this likely affects calcification mechanisms. Interestingly, calcific lesions occur preferentially on the aortic side of the valve in the fibrosa, which is normally the stiffer of the two surfaces [125-127]. As the aorta stiffens with age, axial stiffening and circumferential compliance increase [128]; this results in higher mechanical loads placed on the circumferentially-aligned collagen fibers of the fibrosa, along which AVICs reside [129]. Also, an increase in transvalvular flow greater than 0.3 m/s per year is a clinical predictive marker for patients who might benefit from surgery, suggesting that increased flow contributes to pathological progression [130]. NO release by AVECs is regulated by flow; under laminar shear stress, NO is released and helps maintain valvular homeostasis via signaling to AVICs. However, low and oscillating shear stress, as would occur on the aortic side of a diseased valve, inhibits this release [131]. Also, while the AVICs themselves are not directly exposed to fluid flow, it has been shown that flow alone can differentiate fibroblasts (the majority cell type of the AVIC population) into myofibroblasts [106]. This positive feedback of a stiffening valve that can no longer properly regulate its AVICs to maintain homeostasis is evidence of the importance of the dynamic environment on disease progression.

Substrate composition has also been shown to affect calcification. AVICs cultured on fibrin or tissue culture polystyrene exhibited significantly more CNs than on collagen, fibronectin,

or laminin [102]. In addition, the presentation of RGD to AVICs resulted in far more calcification than the presentation of YIGSR or DGEA. RGD, YIGSR, and DGEA are ECM-derived peptide sequences derived from fibronectin/fibrin/laminin/collagen, laminin, and collagen, respectively. Their receptors are $\alpha v\beta 3/\alpha 5\beta 1/\alpha 1\beta 1$ integrins, 67 kDa laminin receptor, and $\alpha 2\beta 1$ integrin, respectively. Further investigation showed that disruption of the $\alpha 5\beta 1$ integrin- or 67 kDa laminin receptor-mediated binding between AVICs and ECM results in increased calcification [102]. Fibronectin-coated tissue culture polystyrene suppresses calcification markers, while fibrin-coated tissue culture plastic enhances calcification as demonstrated by CN number, ALP activity, αSMA expression, CBFα1 expression, and calcium content via the o-cresolphthalein complexone method. However, both fibronectin and fibrin coating of soft hydrogels suppresses calcification [132]. This suggests that substrate stiffness may be more important than specific ECM component interactions. However, the method in which stiffness is modulated (i.e. by increasing crosslinking) is often coupled to the presentation of ECM components.

Several groups have begun probing CAVD progression using dynamic *in vitro* models. Fisher et al. showed that CN formation is strain dependent and that strain drastically reduces the time to nodule formation – 48 hours versus three to 21 days [133]. At the tissue level, in a bioreactor under cyclic strain, porcine aortic valve cusps showed greater evidence of calcification under 15% (pathologic) strain than 10% strain (physiologic) [134]. In a related study of vascular calcification, 7% cyclic, equibiaxial strain yielded greater mineralization than unstrained calcifying vascular cells [135]. Strain alone is able to induce higher levels of myofibroblastic phenotype as measured by αSMA and collagen synthesis than untreated, unstrained cells, suggesting that strain exacerbates calcification via the dystrophic pathway [48]. In 3D cultures of porcine AVICs, osteogenic media alone was unable to induce calcification, but the addition of

mechanical stress via anchoring the gel led to significant calcification, as well as increases in

αSMA, *Runx2*, and *osteocalcin* mRNA levels [109]. These studies demonstrate the critical role

that mechanical stress and strain has on AVICs, and how such stress can lead to disease.

2.6 – Cadherin Signaling

Cadherins are a family of single-pass transmembrane glycoproteins involved in calcium-

mediated homotypic cell-cell adhesion. Their extracellular portion is comprised of highly

homologous repeat domains of approximately 110 amino acids each and Ca^{2+} binding sites

between each domain. Extracellular homotypic interactions can occur at the membrane of the

same cell, termed cis interactions, or between neighboring cells, termed trans [136]. The

intracellular region of cadherins is subdivided into a cytoplasmic binding domain and a

juxtamembrane domain and is known to complex with β-catenin, p120-catenin, γ-catenin, and

angiomotin. These provide connection to the cytoskeleton through α-catenin and are required

for full strength homotypic bonds to persist. More functions of these associated proteins are

discussed later but are poorly understood in the context of CAVD.

Five subgroups of cadherins exist. Type I classical cadherins (Cadherin-1, Cadherin-2,

Cadherin-3, etc.) are defined by five extracellular domains, five Ca2+ binding domains, and short

cytoplasmic domains. Type II atypical cadherins (Cadherin-5, Cadherin-7-12, etc.) are different

from type I classical cadherins in that they lack an HAV (His-Ala-Val) adhesion recognition

sequence [137]. Desmosomal cadherins bind to γ-catenin and desmoplakin and are linked to

keratin intermediate filaments [138]. Flamingo cadherins have eight extracellular cadherin

regions, seven passes through the membrane, and their intracellular interactions are unknown [139]. Protocadherins are the largest subgroup and contain clustered and non-clustered types. They are primarily observed in the developing nervous system, lack the adhesive sites of classical cadherins, and have unique loop structures [140].

Cadherins that complex with catenins, the classical subgroup, form a specialized type of adhesion junction called an adherens junction. β-catenin binds the cytoplasmic binding domain and regulates the extracellular bond strength while also providing physical interaction through α-catenin with the actin cytoskeleton [141]. Sequestration of β-catenin at the membrane also prevents its nuclear translocation and affects its involvement in canonical Wnt signaling and yes-associated protein 1 (**YAP1**). However, β-catenin can recruit RhoGEFs and/or compete with Arp2/3 [142]. α-catenin can regulate Wnt canonical signaling as well as Ras-MAPK and YAP1 [143]. p120-catenin binds the juxtamembrane domain and regulates cadherins' persistence at the cell membrane. This is accomplished by p120-catenin masking an endocytotic signal as it is bound to the cadherin tail, therefore preventing internalization [144]. p120-catenin complexing with engaged cadherins locally down-regulates RhoA [145]. Also, when cadherins engage in a trans interaction, PIP_3 accumulates, leading to local Rac1 activation [146]. Rho-associated protein kinase (**ROCK**) is required in epithelial cells for recruitment of myosin light chain II (**MLC II**) to adherens junctions [147]. p120-catenin normally inhibits transcriptional repressor KAISO and regulates Rho-GTPases and NF-κB signaling, so its sequestration at the membrane also has widespread effects on contractility [148]. Interactions between Wnt and p120-catenin signaling may prove relevant. p120-catenin complexing with cadherin-1 (**CDH1**) has been shown to control the sequestration of Wnt factor, glycogen synthase kinase-3 beta (**GSK-3β**) [149].

CDH11 has been shown to interact intracellularly with angiomotin in mammalian cells. Angiomotin is a member of the Motin family and is involved in for cell polarity, migration, and the Hippo pathway. Deletion of the angiomotin binding domain of CDH11 resulted in weaker adhesion between L cells in an aggregation assay, providing evidence that angiomotin plays a role in regulating CDH11 binding strength. Deletion of the binding domain also demonstrated that angiomotin is required for CDH11-mediated migration [150]. Cadherins can also interact with receptor-type tyrosine kinases (**RTKs**) to promote many growth and proliferative signaling pathways; CDH1 associates with EGFR, cadherin-5 (**CDH5**) associates with VEGFR2, and cadherin-2 (**CDH2**) can stimulate FGFR signaling [148]. Collectively, these interactions provide a springboard for pathways to probe in AVICs.

Several cadherins have been observed to shed their extracellular domain (~75 kDa), leaving their transmembrane, juxtamembrane, and cytoplasmic domains available to subsequent cleavage by γ-secretase [151]. This shedding has been associated with diseases such as rheumatoid arthritis [151], pulmonary fibrosis [152], breast cancer [153], and the process of apoptosis [154, 155]. Different mechanisms have been reported for the initial cleavage of the cadherin ectodomain [152, 154, 156], but the enzyme responsible for CDH11 shedding has not yet been conclusively identified [151, 157]. The biological function of these shed ectodomains is not fully investigated, but there is some correlation with invasion and migratory behavior, and CDH11 engagement leads to upregulation of IL-6 secretion [151, 153, 156, 157]. Regardless, this phenomenon provides an interesting mechanism for paracrine signaling as well as a potential biomarker of disease.
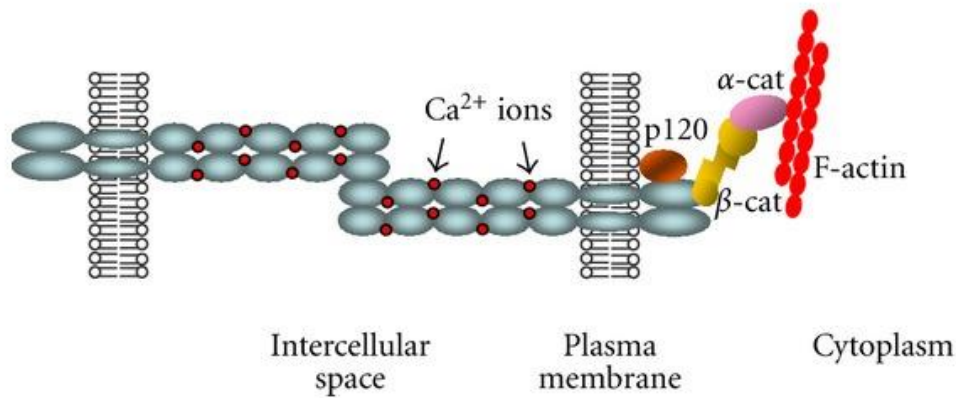
Figure 2.3 – Classical cadherins forming an adherens junction between cells. Adapted from Gama, A. and F. Schmitt. Cadherin cell adhesion system in canine mammary cancer: a review. *Veterinary medicine international.* (2012): 357187 [158].

For this work, we focus on CDH11 because we have demonstrated its necessity for producing CNs in porcine AVICs *in vitro* and it is upregulated in human calcified valves (Figure 2.4). The Merryman Mechanobiology Laboratory has validated the importance of CDH11 expression and engagement *in vitro* as well. siRNA knockdown of CDH11 prevented the formation of CNs when porcine AVICs were subjected to TGF-β1 treatment and equibiaxial strain (Figure 2.5A) [47]. When AVICs were treated with dimethyl celecoxib (**DMC**), an inactive analog of the COX2 inhibitor, celecoxib, to block CDH11 homotypic interactions, the number of CNs formed was significantly reduced (Figure 2.5B-C) [159]. Additionally, a murine model of heritable CAVD, the Notch1$^{+/-}$ mouse, has higher CDH11 expression in its AVICs [160] and a CDH11 overexpression mouse demonstrates evidence of CAVD [161]. Together, these findings support an important role of CDH11 in CAVD.
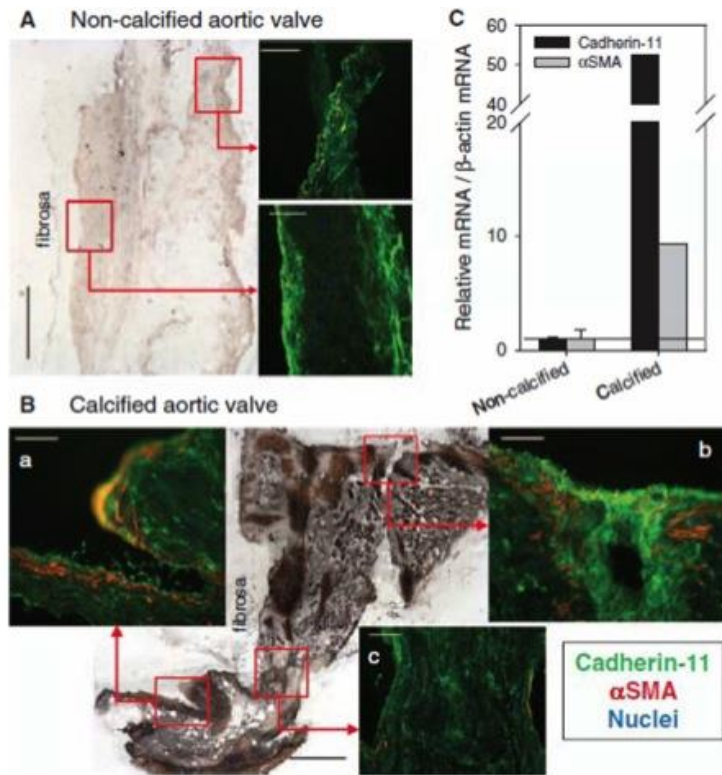
Figure 2.4 – Calcified human valves display elevated CDH11 and αSMA. CDH11 and αSMA protein expression (**A**, **B**) and transcription (**C**) is upregulated in diseased human aortic valves. Adapted from Hutcheson JD, Chen J, Sewell-Loftin MK, Ryzhova LM, Fisher CI, Su YR, and Merryman WD. Cadherin-11 regulates cell-cell tension necessary for calcific nodule formation by valvular myofibroblasts. *Arteriosclerosis, Thrombosis, and Vascular Biology*. 33 (2013). [47]
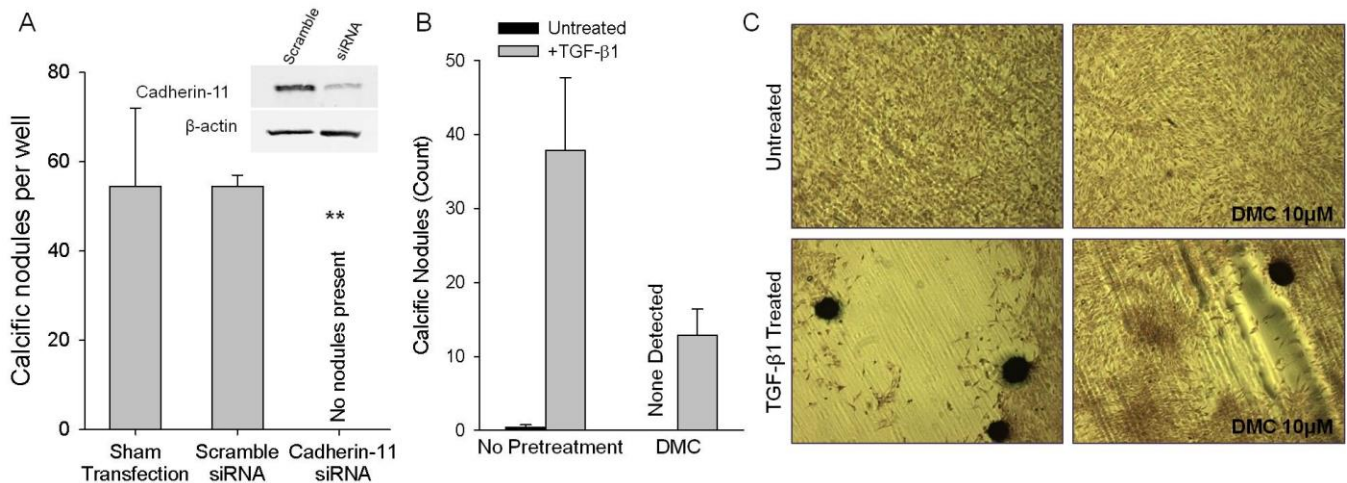
Figure 2.5 – CDH11 is required for CN formation. CDH11 expression knockdown (**A**) or blocking CDH11 engagement (**B**) each prevents CN formation (**C**). (**A**) is adapted from Hutcheson JD, Chen J, Sewell-Loftin MK, Ryzhova LM, Fisher CI, Su YR, and Merryman WD. Cadherin-11 regulates cell-cell tension necessary for calcific nodule formation by valvular myofibroblasts. *Arteriosclerosis, Thrombosis, and Vascular Biology*. 33 (2013). [47]

CDH11, or osteoblast-cadherin, was identified in 1994 in a murine osteoblastic line and differs from its human variant at only 17 amino acids [162]. It is an atypical classical cadherin, meaning it contains the five extracellular domain repeats, but no HAV sequence. In addition to expression in the heart, CDH11 has been identified at high levels in reproductive tissues as well as smooth muscle, lung, and cerebral cortex [163, 164]. CDH11 overexpression is associated with the early stages of breast cancer as well as gastrointestinal, brain, and central nervous system tumors. It is also a target for rheumatoid arthritis, a common inflammatory disease [165].

CDH11 is unique from other cadherins because of several key characteristics. Homotypic bonds formed by CDH11 are two-fold stronger than those formed by CDH2, another mesenchymal cadherin, and also far stronger than bonds formed by CDH1 and CDH5 [166]. CDH11 is also the only cadherin known to participate in focal adhesions, making regulation of cell-substrate interactions as well as the classical cell-cell interactions relevant. In both primary human fibroblasts and neural crest cells, CDH11 (but not CDH2 or C-cadherin) was observed to localize to focal adhesions. Langhe et al. demonstrated the requirement of CDH11's transmembrane and cytoplasmic domains in concert with the extracellular portion of syndecan-4 to adhere to fibronectin [167]. Syndecan-4 is a transmembrane heparan sulfate proteoglycan of ~20 kDa that binds fibronectin and can regulate focal adhesion formation through Rho family GTPase and protein kinase C [168-170].
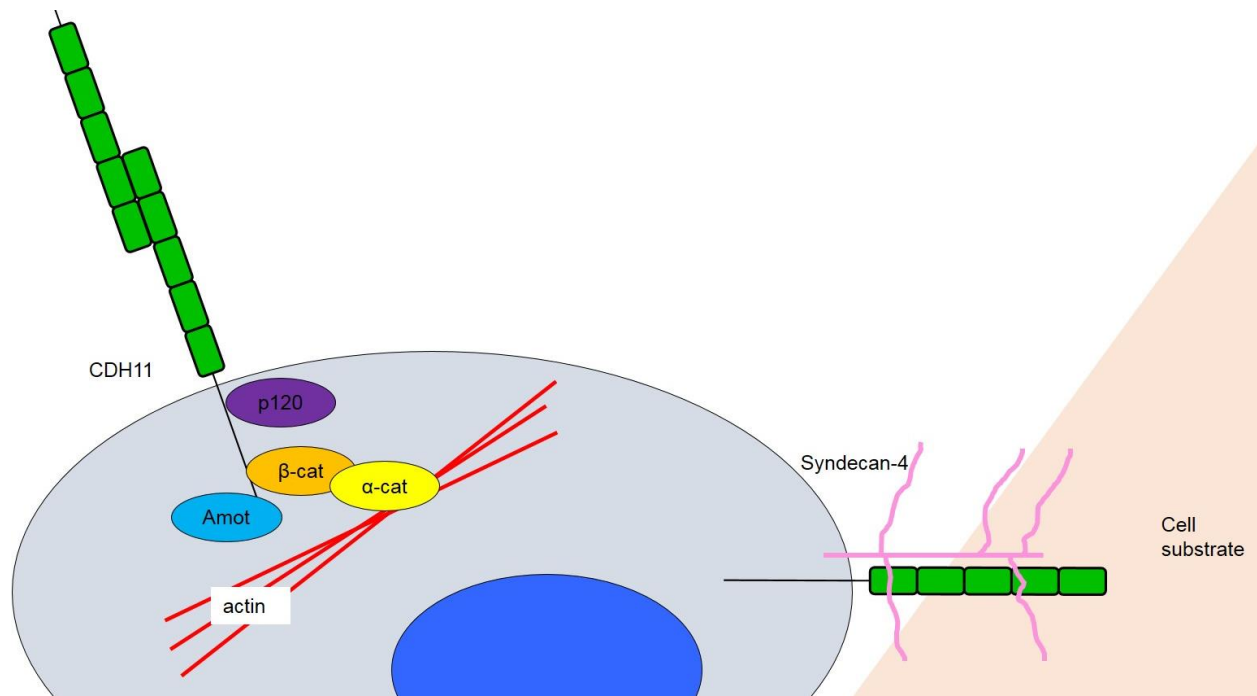
Figure 2.6 – CDH11 is a unique cadherin. CDH11 uniquely participates in both cell-cell and cell-substrate interactions.

2.7 – Notch1 Signaling

Mutations in Notch1 in humans have been correlated with an increased risk of aortic stenosis [171], and Notch1 has recently been shown to be silenced by long noncoding RNA *H19* in cases of idiopathic CAVD [172], making it a relevant signaling pathway to disease. Notch signaling is a highly conserved system comprised of four notch receptors in mammals (Notch1-4). The receptor is a single-pass transmembrane protein that binds to ligands Delta-like and Jagged and can then be cleaved via γ-secretase. This causes release of the intracellular domain which translocates to the nucleus and can affect cell maintenance, proliferation, and apoptosis [160]. Notch1 haploinsufficiency has also been shown to result in higher CDH11 expression in murine AVICs, providing another link between CDH11 and CAVD. Figure 2.7 summarizes recent findings in the crosstalk between Notch1 and CDH11 in the context of CAVD [160].
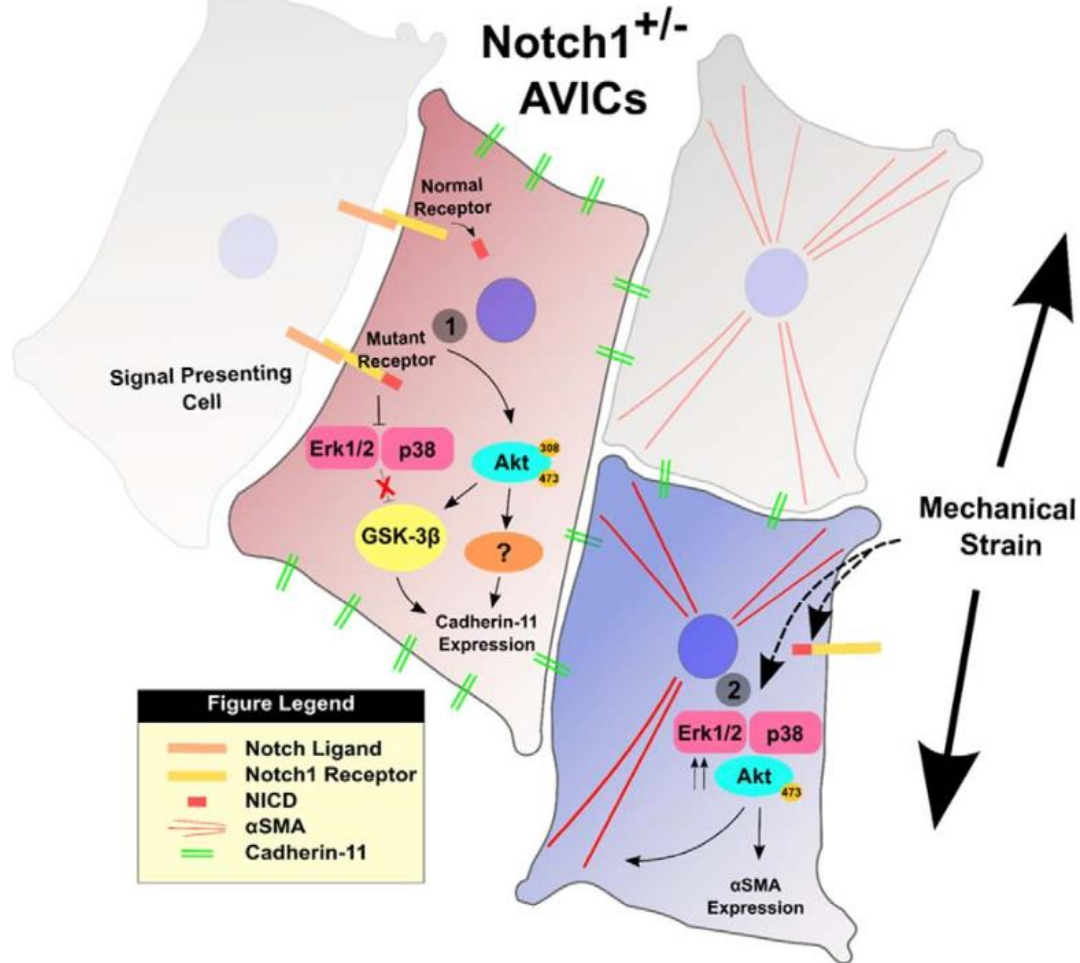
Figure 2.7 – Mechanism of Notch1$^{+/-}$ AVIC activation. Adapted from Chen J, Ryzhova LM, Sewell-Loftin MK, Brown CB, Huppert SS, Baldwin HS, and Merryman WD. Notch1 mutation leads to valvular calcification through enhanced myofibroblast mechanotransduction. *Arteriosclerosis, Thrombosis, and Vascular Biology*. 35 (2015). [160]

2.8 – Interleukin-6 Signaling

CDH11 engagement is known to increase the secretion of IL-6, suggesting an inflammatory role of CDH11 as well. IL-6 is a complex ~25 kDa cytokine, acting in both pro- and anti-inflammatory capacities. Typically secreted by macrophages, fibroblasts, and endothelial cells, IL-6 can also be secreted by osteoblasts, smooth muscle cells, and adipose tissue [173]. IL-6 complexes with IL-6Rα and glycoprotein 130 (**GP130**), resulting in a signaling cascade

through Janus kinases (**JAKs**) and signal transducers and activators of transcription (**STATs**) (Figure 2.8). Chitinase-3-like protein 1 (**Chi3l1**) is downstream of STAT3 and is a secreted inflammatory glycoprotein with unclear function, but association with a variety of cardiovascular diseases [174, 175]. It has also been shown to regulate IL-6-mediated STAT3 phosphorylation, suggesting positive feedback that could exacerbate inflammation [176]. IL-6 has been found to play a role in diseases such as rheumatoid arthritis, atherosclerosis, and prostate cancer [177-179]. Many anti-IL-6 therapeutics are under investigation, but the first to be FDA-approved is tocilizumab for rheumatoid arthritis, Castleman's disease, and systemic juvenile idiopathic arthritis [180-182].
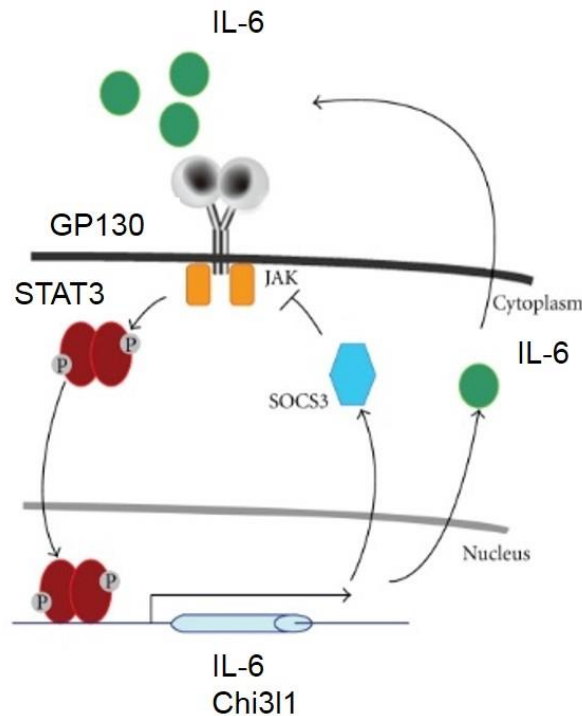
Figure 2.8 – IL-6 signaling axis. IL-6 complexes with GP130 to signal through JAKs and phosphorylate STAT3. STAT3 then causes the transcription of IL-6 and Chi3l1, which can itself cause phosphorylation of STAT3 through IL-6, providing a positive feedback loop of inflammatory signaling. Adapted from Ozawa Y, Kurihara T, Tsubota K, and Okano H. Regulation of posttranscriptional modification as a possible therapeutic approach for retinal neuroprotection. *Journal of Opthalmology.* (2011): 506137. [183]

2.9 – Considerations for Evaluation of *In Vitro* Calcification

Calcium Assays

Evaluation of valve calcification can be separated into two categories: direct, in which the level of calcium or mineralization is directly measured, and indirect, in which markers of the proposed dystrophic and/or osteogenic pathways toward calcification are measured. Direct evaluation has the advantage of determining whether the assay leads to a pathological outcome functionally, whereas the indirect measurements yield more mechanistic information (Table 2.2).

Direct evaluation techniques include von Kossa staining [39, 47, 93, 94, 98, 101, 133, 184-186], Alizarin Red staining [37, 46, 47, 79, 84, 92, 97, 98, 101-103, 106-109, 111, 112, 115, 133, 186-188], energy-dispersive X-ray spectroscopy (**EDS**) [39, 189], Raman spectroscopy [37, 190, 191], scanning electron microscopy (**SEM**) [37, 84, 189], transmission electron microscopy (**TEM**) [37, 96, 189], atomic absorption [115, 192], arsenazo III [84, 133, 184], and o-cresolphthalein complexone [94, 102, 115] measurements. While these are all used as measures of calcification, not all are perfectly specific and thus are often used in concert. The gold standard for calcium detection is atomic absorption spectroscopy. Atomic absorption spectroscopy is based on the principle that different elements absorb different wavelengths of light and it works by atomizing the sample, sending light usually from a hollow cathode lamp of a specific wavelength through the vaporized sample, and measuring the amount absorbed [193]. Samples with increased mineralization content exhibit higher absorbance levels compared to controls.

Probably the most common measure of calcification, Alizarin Red, or 1,2-dihydroxyanthraquinone, stains hydroxyapatite mineralized matrix red-orange. Calcium, but also

magnesium, manganese, barium, strontium, and iron, forms complexes with the dye in a chelation process, and results in a birefringent stain. Calcium is usually in much higher concentration than the other elements, allowing the inference that the areas stained have calcium present. Alizarin Red is often used to stain CNs to verify their mineralization and to help quantify the nodule assay, either by making the nodules easier to count or by extracting the dye for more rigorous quantification. Typical methods for quantifying the amount of dye involve staining of the cells or tissue, washing extensively, extracting via acetic acid or cetylpyridinium chloride, neutralization with ammonium hydroxide, and colorimetric detection at 405nm or 550nm. The acetic acid-ammonium hydroxide method is three times more sensitive than the cetylpyridinium method and results in a better signal to noise ratio, especially for weakly stained samples [46, 194]. This method is also advantageous over Arsenazo III quantification because it has a higher and wider linear range of detection [194].

Von Kossa is another common stain for mineralization, especially in tissue sections. The stain works by reducing the calcium ions with light and replacing them with silver deposits that appear dark grey or black in tissue [195]. This method is not specific for calcium phosphates [196], though it has been suggested that the yellow precipitates are specific [197]. Von Kossa can be further confused if performed on a C57BL/6 mouse, which has melanocytes that appear black in the aortic valve. Thus, von Kossa is performed frequently in combination with Alizarin Red staining.
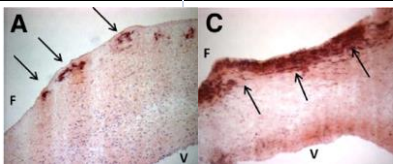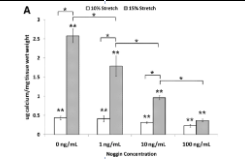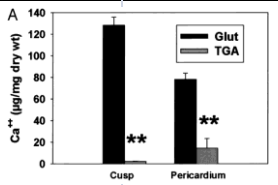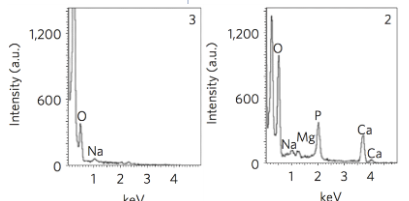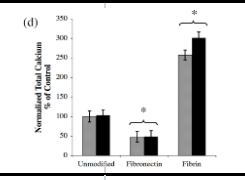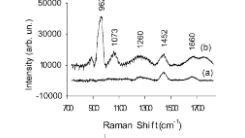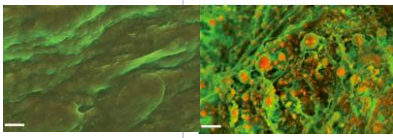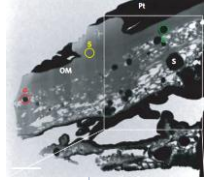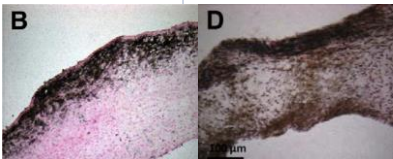
Calcium content can be measured more directly by various methods, but it is important to note that these methods all require lysing of the sample, meaning that calcium from mineralized areas or calcific lesions is not differentiated from intracellular calcium. Arsenazo III is a metallochromogen that complexes with calcium at pH 6.75 without interference from any

other cations commonly present in serum or plasma, and is measured at 650nm [198]. When compared with the o-cresolphthalein complexone method, accuracy and calibration stability increased [199]. The o-cresolphthalein complexone method involves a reaction of Ca^{2+} ions with o-cresolphthalein complexone in an alkaline solution (8-Hydroxyquinoline at pH 10.6) and reading the sample absorbance at 660nm [200]. While these methods do not have a range of detection as large as Alizarin Red quantified via the acetic acid-ammonium hydroxide method, they are still useful for samples with low levels of calcium.

Other elemental methods include SEM, TEM, and Raman spectroscopy. SEM yields topographical and compositional information about the sample's surface with a resolution on the order of nanometers. It can be performed on fixed, dehydrated, and gold-/platinum-/or carbon-sputter-coated samples or in wet conditions via environmental SEM (**ESEM**) [201]. TEM yields information about the sample's chemical identity based on how it absorbs electrons and has a resolution on the order of picometers [202]. It can be performed on fixed, dehydrated, and stained samples. EDS analysis allows one to determine particular elements and their proportions in the sample. It functions on the principle that different elements will absorb different energy X-rays and the amount absorbed corresponds to the amount of element present [203]. EDS can be performed during SEM and ESEM; the advantage to using ESEM is that the samples do not have to be coated and high accelerating voltages can be used. EDS performed during ESEM is better because of the lack of interference from the coating and because the lack of sample preparation yields more authentic data. EDS coupled with ESEM yields quantitative data as well as qualitative [201, 203]. Raman spectroscopy is unique in that it can be performed on live cells. This allows calcification to be measured over time. Raman has also been shown to be an effective diagnostic for human heart valve calcification. Given the appropriate training data, an

algorithm based on spectral shifts could predict whether the tissue was calcified with 100% sensitivity and specificity [190, 191].

Table 2.2 – Summary of direct techniques for evaluating calcification *in vitro* including advantages, limitations, and expected results in the normal and pathological states of human or porcine aortic valves (or rat, for atomic absorption spectroscopy).

		Techniques for Evaluation of Calcification		
Technique	**Advantages**	**Limitations**	**Normal/Pathological Results**	**Notes on Images**
Alizarin Red	Easy to stain; relatively easy to quantify with large range; inexpensive	Other elements, like magnesium, iron, and manganese also stain red		Tissue sections from porcine aortic valves; F=fibrosa; V=ventricularis; Balachandran 2010.
Arsenazo III	No interference from cations commonly found in plasma; easy to quantify; more stable and accurate than o-cresolphthalein complexone	Cannot differentiate between intracellular and extracellular calcium		Porcine aortic valves; 10% strain is physiologic; 15% is pathologic; Balachandran 2010.
Atomic Absorption	Gold standard to determine sample composition	Requires vaporization of sample; expensive		Calcium in porcine cusp or bovine pericardium after glutaraldehyde or triglycidylamine crosslinking in transplant rat model; Connolly 2005.
Energy-Dispersive X-ray Spectroscopy	Easily quantifiable; can perform during SEM or ESEM; ESEM yields more authentic data (no coating interference)	Expensive		Human aortic valves; region with and without calcific lesions; Bertazzo 2013.
O-Cresolphthalein Complexone	Easily quantifiable	Not as stable and accurate as Arsenazo III		Porcine AVICs on various coated tissue culture polystyrene; withTGF-β1 is pathologic (black); Benton 2008.
Raman Spectroscopy	Can be performed on live cells; algorithms can use data to accurately diagnose valve calcification	Expensive		Human aortic valves; a is physiologic; b is pathologic; Otero 2004.
Scanning Electron Microscopy	Topographical and compositional information; resolution ~nm; can be performed on hydrated samples (ESEM)	Difficult to quantify without EDS; expensive		Human aortic valves; scale bar is 3μm; green to orange represents increasing intensity; Bertazzo 2013.
Transmission Electron Microscopy	Chemical composition information; resolution ~pm	Expensive; difficult to perform on hydrated tissue		Human aortic valves; scale bar is 2μm; S=spherical particles; OM=organic matter; Pt=platinum; Bertazzo 2013.
von Kossa	Easy to stain; inexpensive	Melanocytes in valves of a black or brown mouse will appear as false positive stain; not specific for calcium phosphate		Tissue sections from porcine aortic valves; black is calcification; Balachandran 2010.

Indirect Assays

In addition to quantifying mineralization, there are assays commonly employed to assess the progression of calcification by investigating mechanistic markers in the context of CAVD. For example, characterizing the phenotypic changes of AVICs toward myofibroblasts is commonly accomplished via immunofluorescence staining, western blotting, or ELISA for αSMA, collagen gel contraction assays, and wound assays. While ELISA is the most quantitative method for detecting changes in αSMA, immunofluorescence provides information about the protein's localization and both immunofluorescence staining and western blots provide a high enough resolution to see changes in expression level. Collagen gel contraction assays indirectly quantify the myofibroblastic differentiation of AVICs based on the principle that higher levels of αSMA will result in higher contractility, measured by the change in the size of the collagen gel after being seeded with cells. The wound assay involves disruption of a cell monolayer with a pipette tip and it measures the tension between cells via the wound area. The larger the wound, the more neighboring cells there are pulling on those that were disrupted [47].

Alternatively, the osteogenic process of calcification is often evaluated via ALP activity, RT-PCR, immunofluorescence staining, ELISA, and/or western blotting for Runx2 and osteocalcin. ALP activity is measured by how much p-nitrophenyl phosphate is dephosphorylated by ALP, which turns the solution yellow and can be quantified by absorbance at 405nm [204]. Runx2/CBFα1 is a transcription factor associated with osteoblast differentiation and osteocalcin/BGLAP is a protein secreted only by osteoblasts. Runx2 is often used as an early stage marker of osteoblast activity, and osteocalcin and ALP are later stage indicators of osteoblast activity. MMPs have also been investigated via zymography, collagenase activity, immunofluorescence staining, and western blots to determine which were most important for pathological matrix remodeling [95].

Atomic force microscopy (**AFM**) has also been used to characterize the composition of calcified valves *ex vivo* in an effort to better understand the mechanism of formation. The ultra-fine structure of calcified regions of a human aortic valve was examined on a nanometer scale and found to contain 30-70nm diameter closely connected crystals. They suggest the mechanism of formation is deposit from supersaturated interstitial fluid and the crystals then grow on the organic substrate regulated by volume diffusion of interstitial fluid [205]. Recently, an AFM technique for evaluating the mechanical stiffness of valves has also been developed. This technique allows researchers to characterize mechanical properties of small animal models of CAVD, which can be extended to larger animal models and other diseases as well, while leaving enough tissue for concurrent histological studies [125]. Also, AFM comparison of human aortic valves with current valve replacement materials can yield insight into the development of better prosthetics and a possible mechanism of the calcification that is common in prosthetics [206].

CHAPTER 3

Targeting Cadherin-11 Prevents Notch1-Mediated Calcific Aortic Valve Disease

---

3.1 – Introduction

CAVD accounts for ≈15,000 patient deaths per year in the United States, and intervention occurs only when severe stenosis requires surgical replacement of the valve. Recently, it was discovered that long noncoding RNA *H19* expression silences *NOTCH1* in cases of idiopathic CAVD [172], similar to the heritable form in patients with *NOTCH1* mutations [171]. We have previously reported that valves from idiopathic cases are enriched for the cell junction protein, CDH11 [47], and that valve interstitial cells from *Notch1*$^{+/-}$ mice overexpress CDH11 [160]. Thus, we speculate that CDH11 is downstream of NOTCH1 receptor dysfunction and may be a hallmark in both heritable and idiopathic CAVD [207]. Here, we sought to determine whether targeting CDH11, genetically or pharmacologically, would prevent CAVD in *Notch1*$^{+/-}$ mice.

3.2 – Methods

Notch1$^{+/+}$ and *Notch1*$^{+/-}$ mice were given a high-fat/high-cholesterol diet starting at ten weeks. At four months, 10 mg/kg SYN0012, a CDH11-blocking antibody, or IgG2a isotype control was administered by intraperitoneal injection once a week for eight weeks. In a separate cohort, wild-type, *Notch1*$^{+/-}$, and *Notch1*$^{+/-}$;*Cdh11*$^{+/-}$ mice started the high-fat/high-cholesterol

diet at six months and were aged to 12 months. Aortic valve peak velocity (V_{max}), ejection fraction, and left ventricular mass were measured from aortic pulsed-wave Doppler mode and parasternal short-axis M-mode echocardiographic images at four and six months in the drug treatment study or at 12 months in the genetic study. Valves were dissected and embedded in optimal cutting temperature (**OCT**) compound or flash-frozen and placed at $-80°C$. Then 7-µm sections were used for histology and stiffness measurements by AFM; RNA was isolated for cDNA synthesis and quantitative polymerase chain reaction [160]. ANOVA was used to determine statistical differences between groups within cohorts; the *t* test was used to compare SYN0012 and IgG2a treatments. All the above procedures were approved by the Institutional Animal Care and Use Committee at Vanderbilt University.

3.3 – Results

Notch1$^{+/−}$ mice administered IgG2a showed increased V_{max} from four to six months, whereas mice treated with SYN0012 demonstrated no change (Figure 3.1A). The ejection fraction velocity ratio at six months was decreased in mice treated with IgG2a compared with mice treated with SYN0012 (Figure 3.1A). Ejection fraction and left ventricular mass were not different between all groups at six months, suggesting a primary valve phenotype (Figure 3.1A). *Notch1*$^{+/−}$*;Cdh11*$^{+/−}$ mice had a lower V_{max} (not different from wild-type mice) and higher ejection fraction velocity ratio than 12-month-old, age-matched *Notch1*$^{+/−}$ mice, with no difference in left ventricular hemodynamics (Figure 3.1B). These data suggest that CDH11 drives aortic valve stenosis in mice with *Notch1* mutations.

Histology identified hyperplastic leaflets with calcified regions in *Notch1*$^{+/−}$ mice treated with IgG2a (Figure 3.1C). Conversely, SYN0012-treated mice had thin leaflets, indicative of healthier valve morphology. Immunofluorescence demonstrated increased IL-6, an inflammatory

cytokine, and decreased Sox9, an osteogenic repressor, in IgG2a-treated leaflets relative to SYN0012-treated leaflets (Figure 3.1C). Gene expression confirmed that *Il6* and *Chi3l1*, which encodes an inflammation-induced secreted glycoprotein, were decreased and that *Sox9* was increased with SYN0012 treatment (Figure 3.1C). AFM analysis of unfixed tissue sections revealed that leaflets from SYN0012-treated mice were significantly less stiff than those from IgG2a-treated mice (Figure 3.1D). In total, blocking CDH11 prevents valve stenosis, leaflet thickening and stiffening, and inflammatory gene expression. These data demonstrate that SYN0012 interrupts the pathological phenotype normally observed in $Notch1^{+/-}$ mice.

3.4 – Conclusions

It has long been known that *NOTCH1* mutations cause heritable CAVD, but Hadji et al. recently showed that idiopathic CAVD similarly results from repression of *NOTCH1* [172], suggesting a common mechanism between the two. Our current findings reveal that targeting CDH11 is a novel pharmacological strategy that may prevent disease progression in both heritable and idiopathic CAVD. Last, it is worth noting that the humanized version of the murine CDH11 antibody used in this study is currently in phase I clinical trials for rheumatoid arthritis. We believe that these results should motivate a future clinical trial examining the ability of CDH11 blockade to curtail the progression of CAVD from early aortic sclerosis into stenosis.
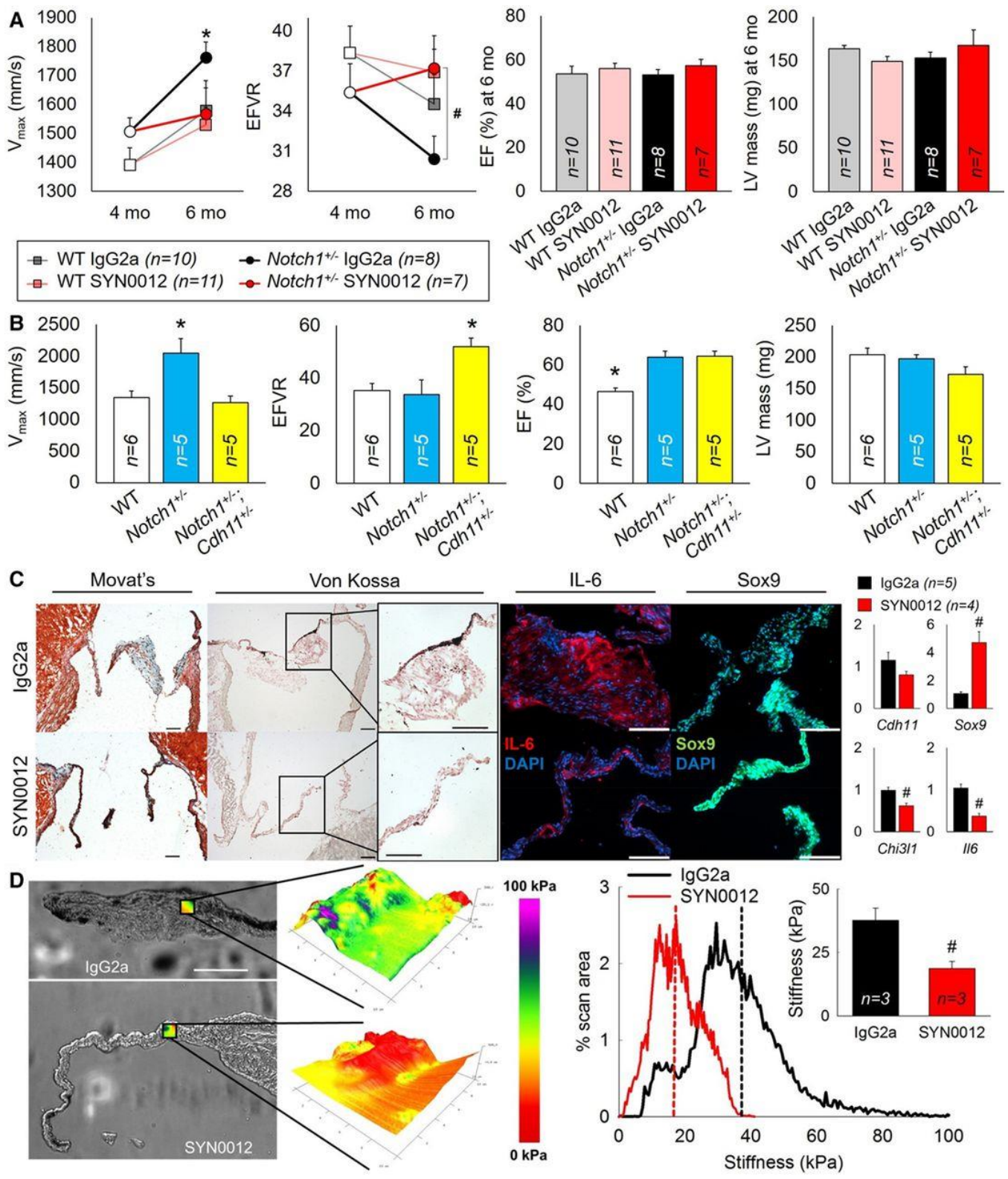
Figure 3.1. Effects of blocking CDH11 in a mouse model of CAVD. Pharmacological (**A**) or genetic (**B**) targeting of cadherin-11 prevents aortic valve stenosis in *Notch1*^+/−^ mice without altering left ventricular (LV) function by reducing leaflet hyperplasia and calcification, inflammatory signals (**C**), and tissue stiffening (**D**), all of which are hallmarks of calcific aortic valve disease. Scale bar=100 μm. EF indicates ejection fraction; EFVR, ejection fraction velocity ratio; IL-6, interleukin-6; LV, left ventricular; V~max~, aortic jet maximum velocity; and WT, wild-type. *$P<0.05$ vs all other groups. #$P<0.05$ for SYN0012 vs IgG2a.

40

CHAPTER 4

Cadherin-11 As A Regulator of Valve Myofibroblast Mechanobiology

Text for Chapter 4 was adapted from <u>Bowler MA</u>, Bersi MR, Ryzhova LM, Jerrell RJ, Parekh A, and Merryman WD. Cadherin-11 as a regulator of valve myofibroblast mechanobiology. In Revision.

4.1 – Abstract

<u>Objective:</u> CDH11 is upregulated in a variety of fibrotic diseases including CAVD. Our recent work identified CDH11 as a potential therapeutic target and a functional blocking antibody against CDH11 has been shown to prevent hallmarks of CAVD in mice. This current study investigates the role of CDH11 in regulating the mechanobiological behavior of VICs.

<u>Approach and Results:</u> Histology was performed on aortic valves from two and 12 month old Cdh11+/+, Cdh11+/-, and Cdh11-/- mice to identify key responses to CDH11 deletion in vivo. AVICs were harvested from Cdh11+/+, Cdh11+/-, and Cdh11-/- immorto-mice and a CDH11 overexpression cell line was generated by infection of WT cells with an mCherry-tagged CDH11 construct. Cells were subjected to inflammatory cytokines TGF- β1 and IL-6, in addition to physiological mechanical challenges, such as cyclic strain and substrate stiffness, to characterize their mechanobiological changes and the molecular mechanisms by which CDH11 regulates these changes.

Conclusions: We show that TGF-β1 and strain exacerbate the myofibroblast disease phenotype in a CDH11-dependent manner and that this phenotypic switch is potentiated through the IL-6 signaling axis.
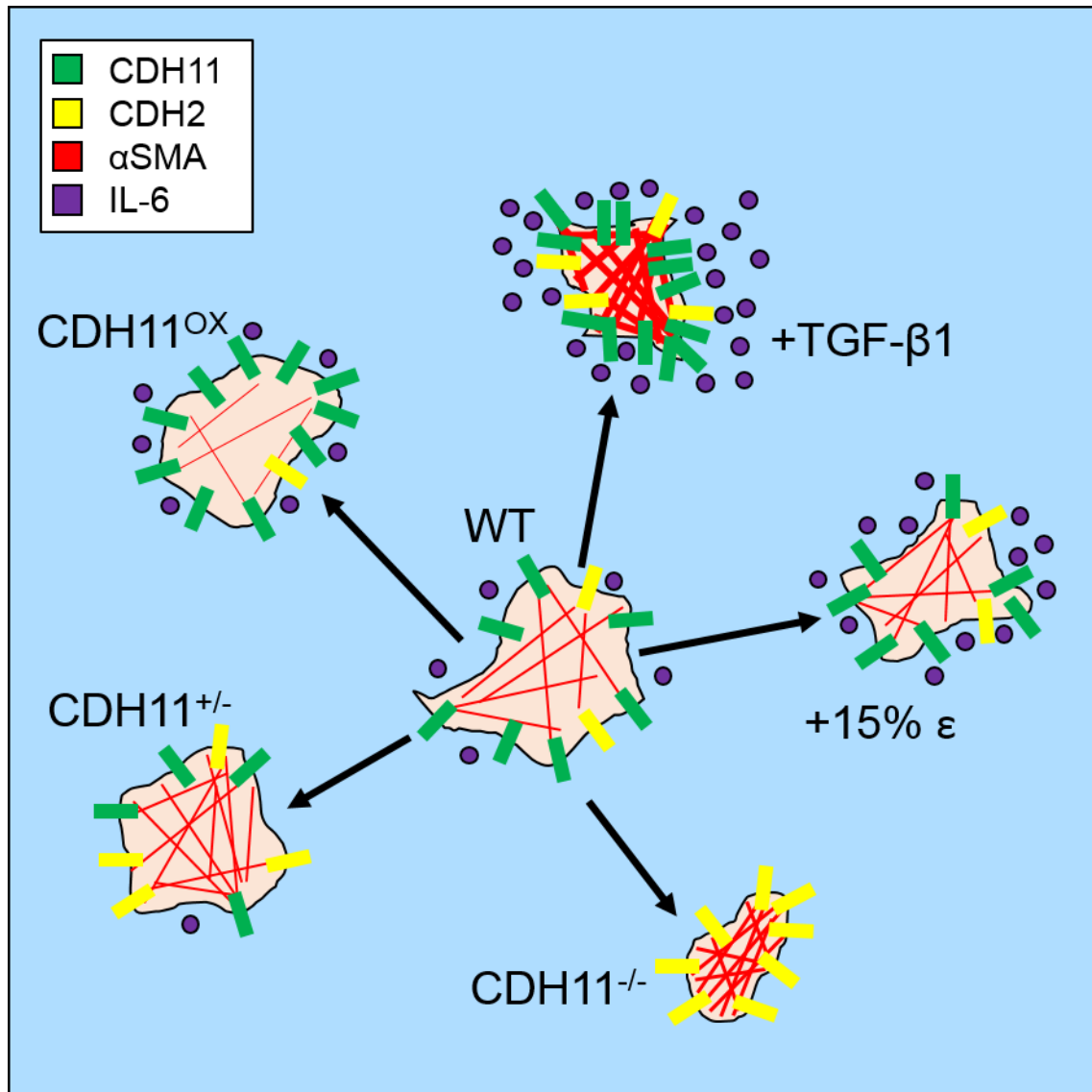
Figure 4.1 – Graphical abstract. Healthy AVICs maintain a balance of CDH11 with αSMA and CDH2 to regulate intracellular and intercellular tension. Exposure to strain and TGF-β1 increase IL-6 secretion, and leads to a more contractile phenotype high in CDH11 and αSMA.

4.2 – Introduction

Calcific aortic valve stenosis is the main indication for the > 100,000 valve replacements performed annually in the US and necessitates total valve replacement, either through SAVR or TAVR [32]. Unfortunately, given the advanced age of many CAVD patients, this intervention carries with it a high rate of morbidity and mortality and is often a procedure of last resort, leaving many to suffer the ill effects of progressively worsening heart function as CAVD advances [33]. A better understanding of the biological mechanism driving the valvular calcification process would allow the development of well-tolerated, non-invasive pharmacologic therapies.

Once believed to be a passive process of degeneration, aortic valve calcification is now thought to be an active process of valvular remodeling mediated largely by AVICs [34]. AVICs are a heterogeneous population of fibroblast-like cells present in all three layers of the aortic valve and important in the structural maintenance of the valve, especially in maintenance of the ECM [35, 36].

Many traditional *in vitro* studies of valve calcification have occurred in a static environment, but the valves exist in a dynamic mechanical state; which likely affects calcification mechanisms. Interestingly, calcific lesions occur preferentially on the aortic side of the valve in the fibrosa, the stiffest of the valve layers [125, 126]. Fisher et al. showed that CN formation is strain dependent and that strain drastically reduces the time to CN formation – 48 hours versus three weeks in static culture [38, 106]. Strain alone is able to induce higher levels of myofibroblast phenotype markers, such as αSMA and collagen synthesis than untreated, unstrained cells, suggesting that strain exacerbates calcification via the dystrophic pathway [48]. These studies demonstrate the critical role that mechanical stress and strain has on AVICs, and

how they can contribute to disease. TGF-β1 is upregulated in diseased human valves and, when given exogenously *in vitro*, exacerbates CN formation [38]. TGF-β1 has been shown to activate myofibroblasts in valves, leading to increased αSMA expression [107, 123]. As these myofibroblasts become more contractile, they likely activate latent TGF-β1 from the ECM [124]. This positive feedback loop provides a strong potential mechanism for dystrophic disease progression.

CDH11 was identified as a potential mediator of these mechanical cues when it was found enriched in calcified human aortic valves [47]. CDH11 is a mechanosensitive transmembrane protein involved in calcium-dependent cell-cell adhesion. The intracellular region of cadherin is subdivided into a cytoplasmic binding domain and a juxtamembrane domain and is known to complex with β-catenin, p120-catenin, γ-catenin, and angiomotin. These provide connection to the cytoskeleton through α-catenin and are required for full-strength homotypic bonds to persist. Homotypic bonds formed by CDH11 are two-fold stronger than those formed by CDH2, another mesenchymal cadherin, and also far stronger than bonds formed by CDH1 and CDH5 [166]. CDH11 is also the only cadherin known to participate in focal adhesions with its partner, syndecan-4 [167]. Together, these characteristics make CDH11 a unique mechanosensitive protein with the potential to sense cell-cell and cell-substrate interactions.

Investigation of CDH11's mode of action in CAVD is also motivated by previous work [47, 160, 208]. In these studies, the *Notch1*^{+/-} mutation was shown to cause a two-fold increase in CDH11 expression in murine aortic valves. Additionally, when *Notch1*^{+/-} mice on a high-fat/high-cholesterol diet were given a functional blocking antibody against CDH11, echocardiograms revealed a reduced maximal velocity across the valve and a higher ejection fraction velocity ratio with treatment, indicating better heart function. Genetic ablation of CDH11 yielded similar results.

The question remaining is why decreased CDH11 expression or activity leads to disease prevention. To answer this question, we examined how CDH11 influences AVIC behavior, especially in the context of mechanical and inflammatory cytokine cues relevant to the heart valve environment.

4.3 – Methods

Isolation of Murine Aortic Valve Interstitial Cells

AVICs were isolated from $Cdh11^{+/+}$ (wild-type, WT), $Cdh11^{+/-}$ (referred to as CDH11$^{+/-}$ throughout), and $Cdh11^{-/-}$ (referred to as CDH11$^{-/-}$ throughout) eight-week-old littermate immorto-mice harboring a temperature-sensitive SV40 tumor antigen gene. Creation of immortalized cultures of VICs decreased variables between cell experiments and lessened the number of animals needed to acquire cells. Immediately after euthanasia, hearts were excised and the aortic valve leaflets were digested in 2 mg/ml collagenase for 30 minutes at room temperature. Valves were pipetted out of the collagenase solution into DMEM supplemented with 10% fetal bovine serum (FBS), 1% Penicillin/Streptomycin (PenStrep) antibiotic, and 10 µg/ml recombinant murine γ-interferon (immorto media). Cells were allowed to adhere to 0.1% gelatin-coated 6-well tissue culture treated plates. To activate the SV40 T antigen and allow for sustained growth, the cells were cultured at 33°C and 5% CO_2 in immorto media when not plated for experiments. All animal procedures were approved by the Institutional Animal Care and Use Committee (IACUC) at Vanderbilt University.

Generation of a Stable CDH11 Overexpression Model

WT AVICs were infected by pLL-CDH11-mCherry to overexpress human CDH11. The infected population was purified via FACS and expanded (referred to as CDH11^{OX} throughout)

(Figure 4.2). More details of this strategy can be found in the supplemental material (Appendix D). This overexpression model is a powerful tool for elucidating CDH11 signaling and robust complement to our knockdown and knockout models [209, 210].
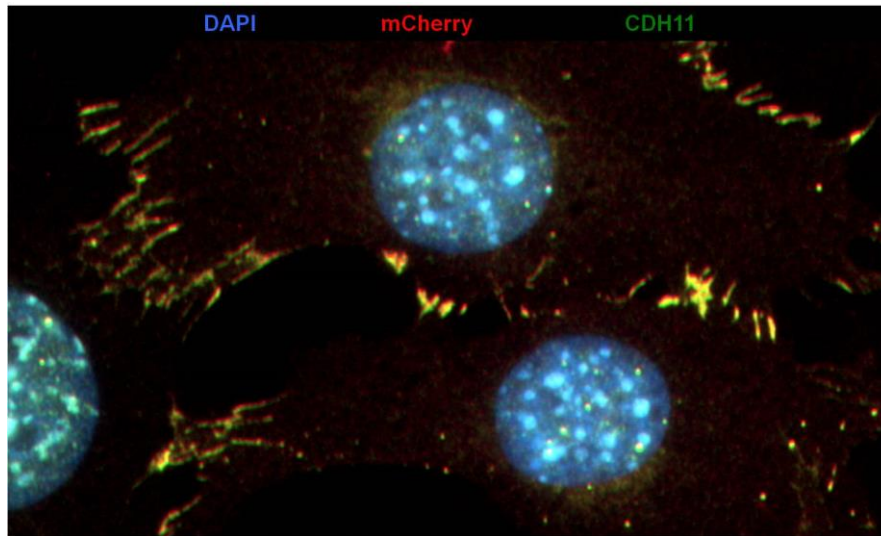
Figure 4.2 – Generation of CDH11^{OX}. WT+CDH11-mCherry AVICs stained for CDH11 (green) and with nuclear stain (blue) show clear co-localization of CDH11 stain and mCherry tag.

Alizarin Red Assay

Tissue was thawed and rinsed with 1X PBS-/- and then diH$_2$O to remove the OCT. A fresh solution of 14mM Alizarin Red S (Sigma-Aldrich A5533) in ultrapure H$_2$O was made and filtered with a 0.45 µm filter. Slides were incubated in the 14mM solution for 30 minutes and then rinsed in diH$_2$O. Slides were then dehydrated in sequential incubations with acetone, acetone:xylene (1:1), and xylene. Tissue was mounted in Permount (Fisher SP15-100) and allowed to dry overnight.

Von Kossa

Tissue was thawed and rinsed with 1X PBS-/- and then diH$_2$O to remove the OCT. Slides were dried and tissue was carefully outlined in a PAP pen (Biotium 22006). ~100 µl AgNO$_3$

solution was pipetted onto the tissue and incubated for 45 minutes under a 60W bulb while sitting on aluminum foil. The silver nitrate was aspirated and the slides were rinsed in diH$_2$O. Tissue was then incubated in ~100 µl sodium thiosulfate solution for two minutes before being aspirated. The slides were washed in diH$_2$O and incubated in ~100 µl filtered nuclear fast red for 10 minutes. The slides were rinsed in diH$_2$O and then dehydrated with sequential washes in 100% ethanol and xylene. Tissue was mounted in Permount (Fisher SP15-100) and allowed to dry overnight.

Immunofluorescence

Tissue from n ≥ 3 mice was embedded in OCT within 30 minutes of dissection and sectioned at 7µm. Cultured cells were plated on fibronectin-coated coverslips, fixed and permeabilized in 4% PFA + 0.1% Triton, blocked in 5% bovine serum albumin (**BSA**), and incubated with primary antibody in 1% BSA overnight for 4°C. Coverslips were washed and incubated for 90 minutes in secondary antibody in 1% BSA before mounting in Prolong Gold with DAPI (Invitrogen P36931). Dilutions and product numbers of antibodies used can be found in the supplemental material (Appendix A). Vinculin-stained images were used to quantify focal adhesion length and number. Custom image processing analyses based on intensity thresholding and object separation [211] identified focal adhesions (at least 250 adhesions per image and at least six images per group), measured several properties, and fit a lognormal distribution to their measured lengths (Figure C.1). More detail can be found in the supplemental material (Appendix C).

Collagen Gel Contraction

Type I collagen (Advanced Biomatrix, 5005), 10X PBS-/-, and 0.1M NaOH in an 8:1:1 ratio was mixed and adjusted to pH 7.4 with 0.1 M HCl. 200 µl of this solution was then carefully

pipetted into the center of 0.5"-diameter Teflon rings which had been sterilized with 70% ethanol and UV light. After polymerization at 37°C for one hour, 40,000 cells in 200 µl DMEM supplemented with 10% FBS and 1% PenStrep antibiotic (complete media) were seeded on top of each gel and allowed to adhere at 37°C for 30 minutes. Complete media with or without 1 ng/ml recombinant murine TGF-β1 (Fisher Scientific 7666MB005) was then added around the gels and the gels were detached from the rings and the bottom of the tissue culture plate. After equilibration for 30 minutes, free-floating gels were imaged on a Leica dissection scope and this was considered t=0. Gels were imaged at least every 24 hours and media was changed every 48 hours for up to five days. Gel size was quantified via ImageJ [212].

Traction Force Microscopy

High-resolution traction force microscopy (**TFM**) was used to quantify the cell-matrix traction forces generated by each cell line (CDH11^{OX}, WT, CDH11$^{+/-}$, CDH11$^{-/-}$) (n ≥ 72 for single cells and n ≥ 25 for cell pairs). TFM was performed using experimental and computational methods similar to those described previously [213-217]. AVICs were plated sparsely on polyacrylamide gels (Young's modulus E = ~23 kPa [218]) containing fibronectin and embedded fluorescent microbeads (excitation/emission of 560/645nm) and allowed to adhere for 14 hours [219]. The media was changed to L-15 media for at least one hour prior to imaging. Comparisons of the bead distributions below each cell before and after detachment were used to compute gel displacement fields via an optical flow-based image correlation technique [213]. Combined with polyacrylamide gel material properties, the computed displacements were used to reconstruct traction forces on the surface of the polyacrylamide gel using a regularized Fourier transform traction cytometry (reg-FTTC) framework [220-222]. Total force generated by each cell was calculated as the integral of the traction magnitude within the cell boundary [223], and cell-cell interaction forces between cell pairs were estimated based on a traction imbalance that arises

at the contact border [224]. Further details of this strategy can be found in the supplemental material (Appendix B).

Mechanical Strain

AVICs were plated in complete media as a confluent monolayer at 800,000/well on pronectin-coated BioFlex® plates and allowed to equilibrate overnight. The plate was then subjected to 15% equibiaxial cyclic strain at 1 Hz for 24 or 48 hours using the Flexcell FX-5000 Tension System (Hillsborough, NC) to assess changes in cytokine secretion, protein expression, or collagen deposition.

Polydimethylsiloxane Substrate Stiffness

Polydimethylsiloxane (PDMS) substrates were made at various stiffnesses by modifying the ratio of Sylgard 184 elastomer base:Sylgard 184 curing agent (Dow Corning):silicone oil (Sigma-Aldrich 378364) – 10:1:2 for 940 kPa and 20:1:0 for 370 kPa. 2 mL of PDMS solution were aliquoted into each 6-well plate well and a pressure of -15mmHg was applied for at least 30 minutes. The plates were left to cure overnight in the vacuum. Before plating cells, plates were sterilized under UV light for at least 45 minutes and were coated in 1 µg/ml fibronectin (Sigma F0895) for at least one hour. Cells were then plated at 10,000/cm^2 for 48 hours before being lysed for western blot.

Western Blot

Cells were lysed in RIPA buffer and frozen at -80°C. Protein lysate was linearized by the addition of β-mercaptoethanol and heat (five minutes at 100°C) and run on an 8% or 12% polyacrylamide gel to separate proteins by size. Proteins were then transferred to a nitrocellulose membrane (LI-COR 926) and blocked with Odyssey Blocking Buffer (LI-COR 927) to prevent

non-specific antibody binding. Membranes were incubated serially in primary antibody against proteins of interest followed by secondary antibodies conjugated to a fluorescent tag. Details can be found in the supplemental material (Appendix A). Membranes were scanned on a LI-COR Odyssey fluorescent scanner. Proteins were quantified with densitometry (Image Studio Lite) and normalized to αTubulin or total protein if evaluating phosphorylation.

ELISAs

Cells were plated at 10,000/cm^2 and conditioned media was harvested after 48 or 96 hours. Media was centrifuged at 1,500 rpm for 10 minutes at 4°C. ELISAs for IL-6 (R&D Systems, DY406) and Chi3l1 (R&D Systems, DY2649) were performed on the supernatant from each sample. Optical densities were read at 450nm with densities at 562nm subtracted to correct for optical imperfections in the plate. Standards were fit to a four parameter logistic and used to calculate sample concentrations using MyAssays [225].

Picrosirius Red Assay

Cells were plated at 10,000/cm^2 and grown for 96 hours with media changes every 48 hours. Cells were rinsed with PBS-/-, fixed in 90% methanol at -20°C overnight, washed in PBS-/-, and then incubated with picrosirius red stain (Electron Microscopy Sciences 26357-02) for one hour. To elute the stain for quantification, cells were rinsed in acidified water (0.5% acetic acid) and incubated with 0.1M NaOH for one hour. 200µl from each sample was transferred to a 96-well plate and optical densities were read at 540 nm. Optical densities were normalized to untreated samples or proliferation, as indicated in figures.

<u>Fluorescence-Activated Cell Sorting</u>

AVICs were lifted with 0.05% trypsin for no more than 10 minutes and resuspended in HBS FACS buffer (20mM HEPES + 137mM NaCl + 3mM KCl + 1mM $CaCl_2$ + 2% FBS in MilliQ H_2O). Cells were centrifuged at 350 x g for 10 minutes at 4°C, strained through a 100µm filter (Sigma-Aldrich CLS431752), and aliquoted at 500,000 live cells/tube. Cells were centrifuged at 350 x g for 10 minutes at 4°C and resuspended in 100 µl of primary antibody against CDH11 (1.25 µg/ml 23C6; gift from Michael Brenner) for one hour. Cells were washed in 1 ml HBS FACS buffer with 1:20,000 DAPI (Life Technologies D1306) and centrifuged at 350 x g for 10 minutes at 4°C. Samples were then incubated with 100 µl secondary antibody (1.25 µg/ml IgG1-PE; BioLegend 406607) for 30 minutes in the dark. Cells were washed in HBS FACS buffer and then incubated in Transcription Factor Fixation/Permeabilization working solution (Tonbo Biosciences TNB-0607-KIT) for 30 minutes in the dark. After this, all washes and incubations were performed in Permeabilization buffer (Tonbo Biosciences TNB-0607-KIT) to facilitate diffusion through the fixed cells. Cells were centrifuged at 350 x g for 10 minutes at 4°C and resuspended in 100 µl conjugated antibody against αSMA (1:500 αSMA-647; Novus Biologicals NBP2-34522AF647) for 30 minutes in the dark. Cells were washed in Permeabilization buffer and centrifuged at 350 x g for 10 minutes at 4°C before being resuspended in 0.5 ml HBS FACS buffer and analyzed.

<u>Statistics</u>

All conditions were n ≥ 3 unless otherwise noted. Differences were analyzed via one-way ANOVA in SigmaPlot Version 11.0 and a p-value < 0.05 was considered statistically significant. Data were presented as a mean ± SEM. If the data was non-normal, the Kruskal-Wallis ANOVA on ranks was performed and significance was defined as p-value < 0.05.

4.4 – Results

<u>Calcification is associated with increased myofibroblasts and IL-6 signaling</u>

Positive staining of Alizarin Red and von Kossa (i.e., calcification) is apparent in the leaflets of *Cdh11$^{+/+}$*, *Cdh11$^{+/-}$*, and *Cdh11$^{-/-}$* mice as early as 2 months of age. However, it appears that the staining intensity increases with increasing age up to 12 months with the exception of the *Cdh11$^{-/-}$* mice that display no evidence of calcification (Figure 4.3A-B). 12 month old mice have higher αSMA expression (Figure 4.3C) and lower CDH11 expression (Figure 4.3D) than 2 month olds. CDH2 is higher in the 12 month old mice, and of these, the *Cdh11$^{-/-}$* have the highest expression, followed by *Cdh11$^{+/-}$* and then *Cdh11$^{+/+}$* (Figure 4.3E). Older mice demonstrate drastically higher expression of STAT3 (Figure 4.3F), a downstream transcription factor of IL-6 that regulates T cell differentiation, indicating more active IL-6 signaling, correlating with CDH11 expression (Figure 4.3F), though there are not consistent differences in IL-6 expression (Figure 4.3G).
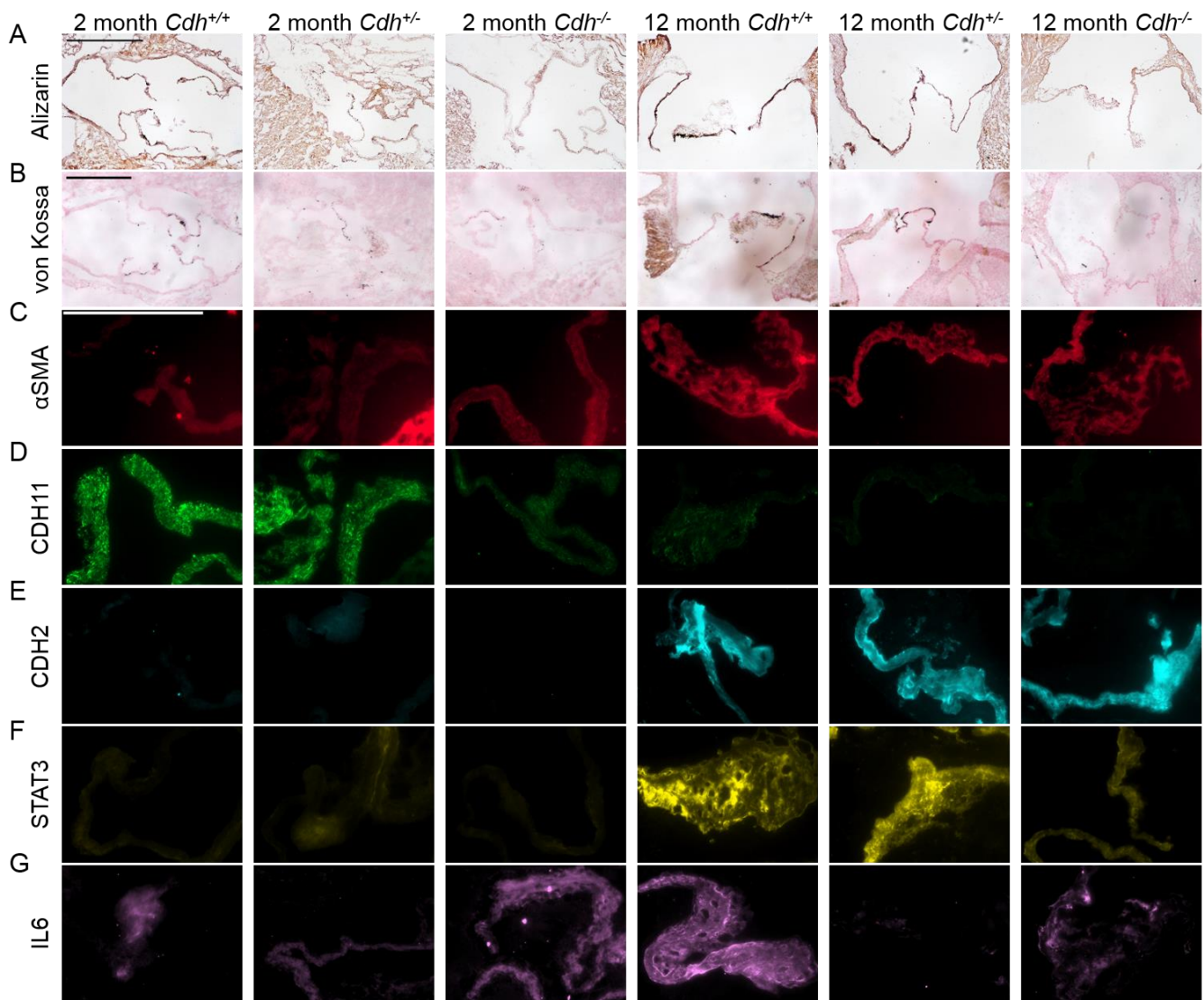
Figure 4.3 – 12 month old mice show an increase in myofibroblast markers and IL-6 signaling. Histology (**A-B**) and immunofluorescence (**C-G**) of *Cdh11*$^{+/+}$, *Cdh11*$^{+/-}$, and *Cdh11*$^{-/-}$ murine aortic valves at 2 and 12 months. Scale bars are 500 µm.

<u>Cadherin-11 regulates αSMA, collagen deposition, and cadherin switching</u>

Given that reduction of CDH11 affects the propensity for valve calcification and contractile marker expression *in vivo*, we wanted to examine the intrinsic effect of CDH11 expression on AVIC function by comparing the phenotypes of CDH11^{OX}, WT, CDH11$^{+/-}$, and CDH11$^{-/-}$ cell lines. Assessment of these cell lines via collagen gel assay indicated that both loss and overexpression of CDH11 results in decreased contraction at the population level (Figure 4.4A), suggesting the WT AVICs express a set point of CDH11 that results in the highest contractility. Quantification

of αSMA, the myofibroblast marker often associated with contractility, revealed that CDH11 expression (Figure 4.4B) is inversely correlated with αSMA expression (Figure 4.4C). Collagen deposition matched the gel contraction trends (Figure 4.4D), consistent with a myofibroblast phenotype.
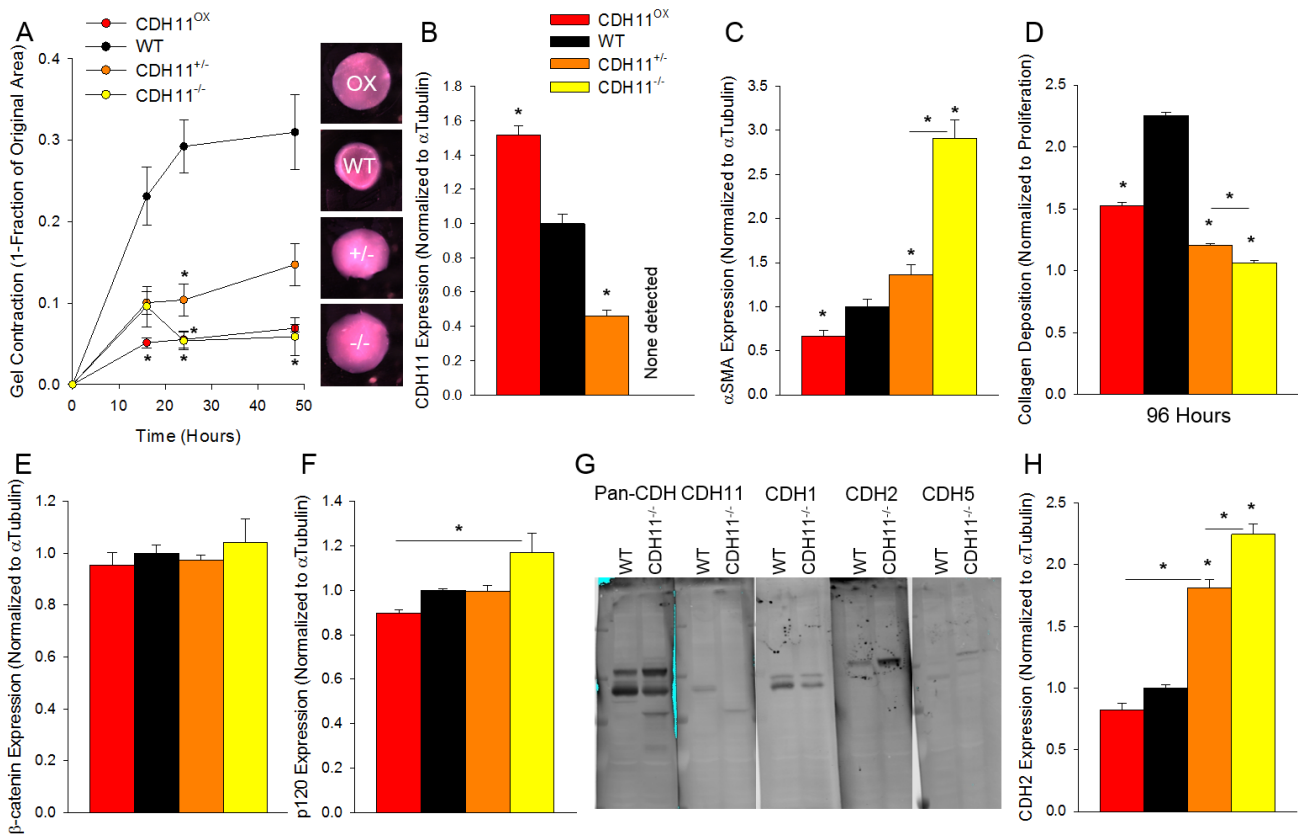
Figure 4.4 – CDH11 regulates AVIC phenotype through αSMA, collagen, catenins, and cadherin switching. Loss and overexpression of CDH11 result in reduced contractility (**A**), but an inverse relationship with αSMA (**B-C**). The most contractile, WT AVICs are also the most active in collagen deposition (**D**). Loss of CDH11 expression results in increased p120-catenin expression (**F**), indicating cadherin switching. Investigation of other cadherin expression in WT and CDH11$^{-/-}$ AVICs pointed to an upregulation of CDH2 (**G-H**). * = p-value < 0.05 compared with WT unless otherwise indicated.

Since αSMA expression data did not correlate with gel contraction as expected, we looked to other molecules known to interact with cadherins, specifically β-catenin and p120-catenin (Figure 4.4E-F). Interestingly, while β-catenin was not different between groups, we observed that p120-catenin was also inversely correlated with CDH11 expression (Figure 4.4F). This

increase suggests that p120-catenin must be interacting with other cadherins and highlighted a potential for cadherin switching in CDH11$^{-/-}$ AVICs. Indeed, comparison of cadherin expression between WT and CDH11$^{-/-}$ AVICs revealed a clear switch from CDH11-dominated expression to a higher molecular weight, CDH2-dominated expression (Figure 4.4G). This inverse relationship was confirmed in the CDH11$^{+/-}$ and CDH11^{OX} lines (Figure 4.4H).

Cadherin-11 regulates cell-substrate force transmission as well as intercellular tension

CDH11 is distinct from other cadherins in that it can directly interact with the substrate and participate in focal adhesion complexes by binding with syndecan-4 [167]. To investigate cell-substrate interaction at the single cell level and isolate the mechanical effects of cell-substrate interactions from cell-cell interactions, we employed TFM on single and pairs of cells. Similar to the collagen gel contraction, both deletion and overexpression of CDH11 resulted in reduced mean traction forces in single cells (Figure 4.5A-B). Unsurprisingly, the interaction forces between pairs of cells trended with CDH11 expression (Figure 4.5C). Interestingly, when mean forces of single cells were normalized to cell area (Figure 4.5D), the differences between groups were eliminated.
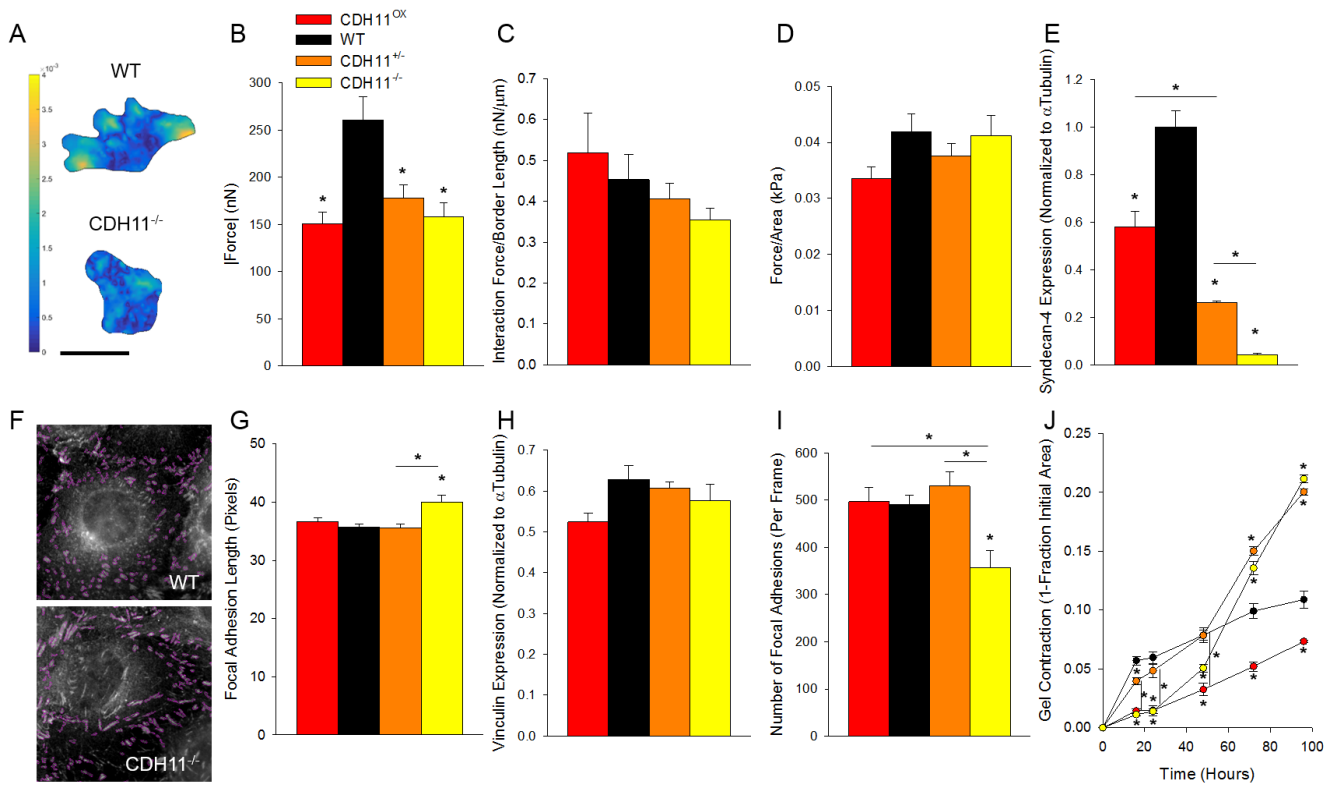
Figure 4.5 – CDH11 regulates contractility through focal adhesions. TFM was used to quantify mean force generated (**A**) based on gel displacement. Deletion or overexpression of CDH11 reduces mean generated force in single cells (**A-B**). Analysis of pairs of cells revealed a decrease in cell-cell interaction force with CDH11 (**C**). Differences between the single cells disappear when cells are normalized to their area (**D**). Syndecan-4 allows CDH11 to participate in focal adhesions, and its expression is CDH11-dependent (**E**). Lack of CDH11 results in longer focal adhesion lengths (**F-G**), but fewer focal adhesions (**I**), resulting in unchanged vinculin expression (**H**). When embedded in a gel, CDH11 expression has an inverse relationship with contractility by 96 hours (**J**). Scale bar = 50 μm * = p-value < 0.05 compared with WT unless otherwise indicated.

To determine if CDH11 regulates cell size through focal adhesions, we first evaluated syndecan-4 expression. Similar to the cell area data, the $CDH11^{OX}$, $CDH11^{+/-}$ and $CDH11^{-/-}$ lines produced significantly less syndecan-4 than WT AVICs (Figure 4.5E). Further investigation of focal adhesion proteins focused on vinculin, which has been observed to participate in focal adhesions with CDH11 [167]. Though the lengths of adhesions were different (Figure 4.5G), total vinculin expression remained constant between lines (Figure 4.5H). Accordingly, the average number of focal adhesions per field of view in the $CDH11^{-/-}$ cells was significantly less than the other AVICs (Figure 4.5I). To test the importance of cells' adhesion to the substrate, we performed another gel contraction but prepared the experiment with the AVICs embedded within

the gel (3D), as opposed to on top (2D). While the first 24 hours of the 3D gel contraction follow the same trends as the 2D gel contraction, by 48 hours the CDH11$^{+/-}$ and CDH11$^{-/-}$ AVICs overtook the WT AVICs (Figure 4.5J).

Effects of TGF-β1 on interstitial cell phenotype

Having established CDH11's effect on AVIC phenotype in an *in vitro* environment, we wanted to study its role in mediating common disease initiators. TGF-β1 is upregulated in diseased valves and is known to induce the myofibroblast phenotype believed to be responsible for dystrophic calcification. In all cell lines, TGF-β1 treatment resulted in an increase in both CDH11 and αSMA expression consistent with the disease phenotype (Figure 4.6A-C). With similar levels of myofibroblast markers between CDH11^{OX} and WT lines, we would expect to see similar levels of contractility. However, 2D collagen gel contraction maintained the same trends with and without TGF-β1 treatment. Despite an overall increase in contractility due to TGF-β1 treatment, both loss and overexpression of CDH11 resulted in decreased contractility compared with WT AVICs (Figure 4.6D). CDH2 expression also trends up with TGF-β1 treatment (Figure 4.6E). After 24 hours of TGF-β1 treatment, the percentage of cells expressing αSMA increases (Figure 4.6F), whereas the percentage expressing CDH11 does not change (Figure 4.6G), as measured by FACS.
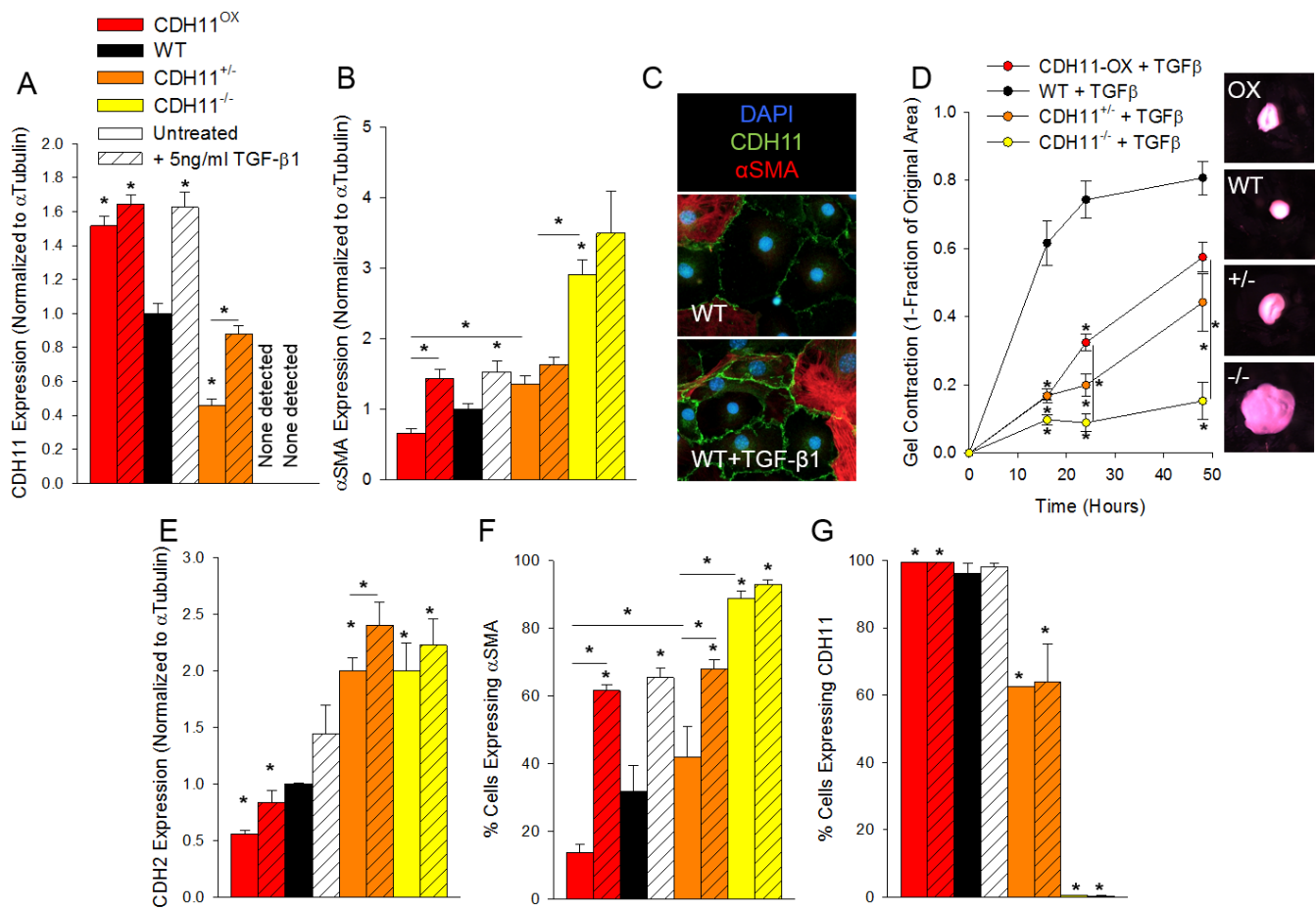
Figure 4.6 – TGF-β1 causes an increase in myofibroblast markers. TGF-β1 treatment increases both CDH11 and αSMA, overriding their inverse relationship (**A-C**). It also increases overall contractility but does not overshadow the effects of CDH11 genotype (**D**). TGF-β1 also causes a slight increase in CDH2 (**E**). FACS analysis reveals an increase in the percentage of cells expressing αSMA (**F**), but similar percentages of AVICs expressing CDH11 (**G**). * = p-value < 0.05 compared with WT unless otherwise indicated.

Effects of mechanical stimulation on interstitial cell phenotype

To complement this biochemical model, we also exposed AVICs to pathologic biomechanical environments. Strain is a key regulator of the dystrophic model of calcification and we therefore investigated the impact of pathologic strain (15%) on AVIC phenotype [134]. Pathologic strain causes αSMA expression to trend up in the CDH11-expressing cells, but not significantly (Figure 4.7A), while CDH11 expression decreases (Figure 4.7B). Overall, pathologic strain does not induce much change to the AVIC phenotype.
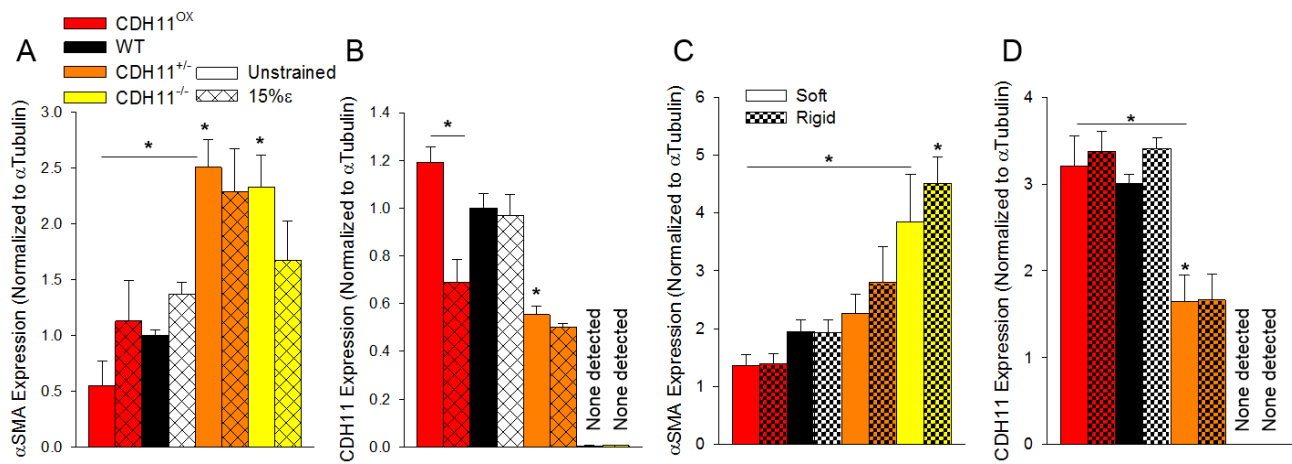
Figure 4.7 – AVIC myofibroblast markers are more sensitive to strain than substrate stiffness. Exposure to pathologic strain promotes CDH11-dependent upregulation of αSMA (**A**) and few changes to CDH11 (**B**). Increased substrate stiffness does not markedly change myofibroblast marker expression (**C-D**). * = p-value < 0.05 compared with WT unless otherwise indicated.

The aortic valve stiffens with increasing age and disease progression. To investigate the role of this change in mechanical environment, we compared protein expression between AVICs plated on a soft substrate (370 kPa) and rigid substrate (940 kPa). Stiffness values were informed by AFM measurements of healthy and diseased murine valves [125]. Stiffness does not appear to have an appreciable effect on myofibroblast differentiation of AVICs. αSMA and CDH11 expression are unchanged (Figure 4.7C-D).
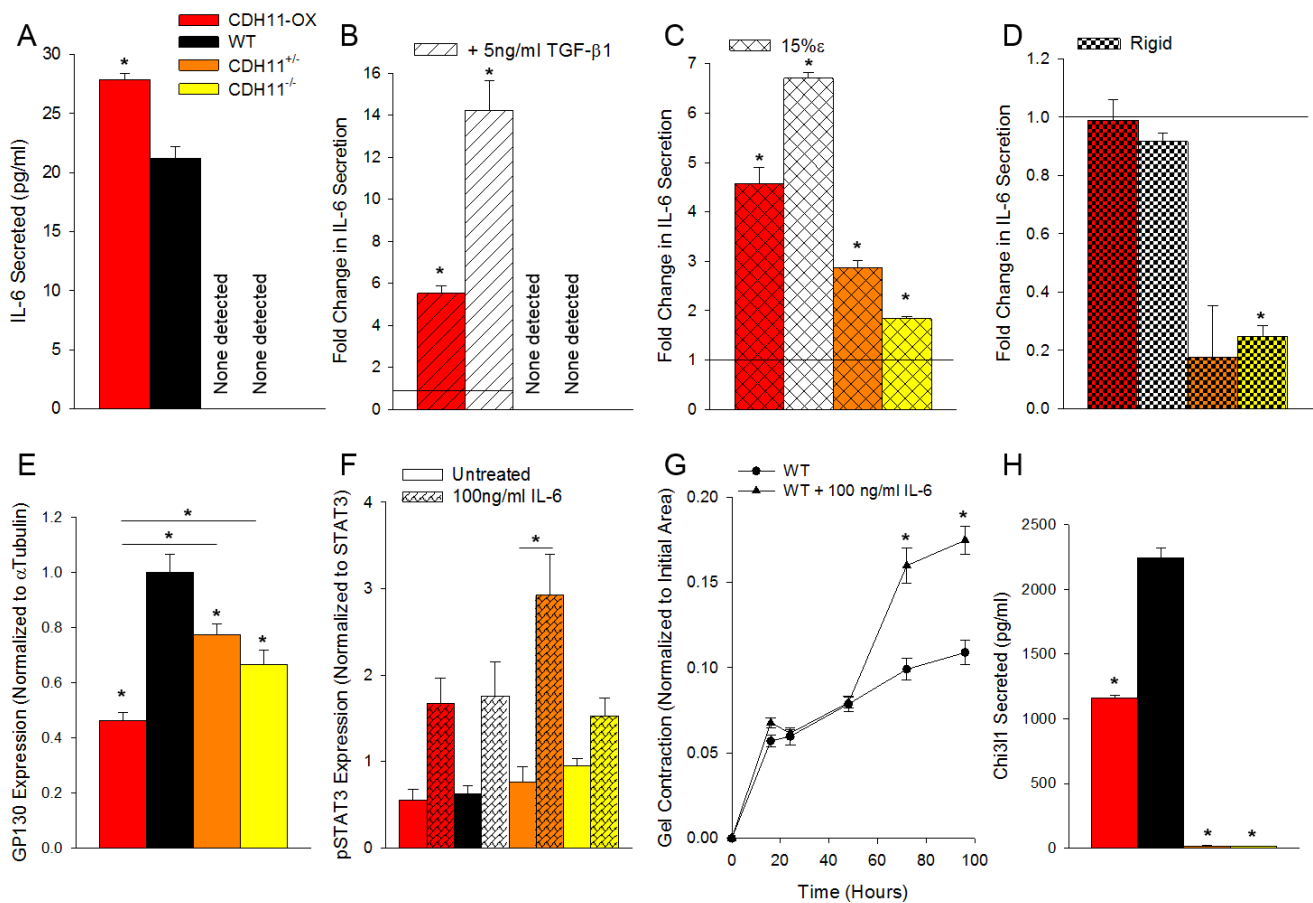
Figure 4.8 – CDH11 mediates contractility through IL-6 signaling axis. IL-6 secretion is correlated with CDH11 expression (**A**). IL-6 secretion is dramatically increased by disease initiators, TGF-β1 (**B**) and pathologic strain (**C**), but not substrate stiffness (**D**). IL-6 receptor GP130 is expressed in a CDH11-dependent manner (**E**) and IL-6 sensitivity was verified with an increase in STAT3 phosphorylation (**F**). IL-6 leads to increased contractility (**G**). Also correlating with contractility and downstream of STAT3 is Chi3l1 secretion (**H**). * = p-value < 0.05 compared with WT or the untreated case in fold change comparisons unless otherwise indicated.

Inflammatory response of disease initiators is dependent on IL-6 and cadherin-11

When CDH11 is engaged, even without mechanical stimulation, it causes fibroblasts to secrete IL-6 [226]. Thus, we were interested in whether the aforementioned disease initiators affect IL-6 production. At baseline, IL-6 secretion is correlated well with CDH11 expression (Figure 4.8A). IL-6 secretion increases with TGF-β1 treatment (Figure 4.8B) and pathologic strain (Figure 4.8C), but not substrate stiffness (Figure 4.8D). AVICs could be responsive to IL-6 because they express its receptor, GP130. Interestingly, GP130 expression (Figure 4.8E) correlates well with 2D collagen gel contraction (cf. Figure 4.4A) and traction force

measurements (cf. Figure 4.5B). We also see a marked increase in STAT3 phosphorylation with IL-6 treatment (Figure 4.8F). As a more functional readout of AVIC phenotype changes initiated by IL-6, we treated 3D collagen gels with IL-6 and observed an increase in AVIC contractility (Figure 4.8G). Also reported to be downstream of STAT3 and an indicator of various cardiovascular diseases [227, 228], Chi3l1 is secreted in the same trends as gel contraction and traction force (Figure 4.8H); reduced in the CDH11^{OX} AVICs and even lower in the CDH11$^{+/-}$ and CDH11$^{-/-}$ AVICs.

4.5 – Discussion

Previous work *in vivo* has shown that targeting CDH11 prevents CAVD [208] and that overexpression leads to this disease [161]. Given that AVICs are the mediators of CAVD, we are interested in understanding the intrinsic role of CDH11 in them. Myofibroblasts are the activated, disease-driving phenotype of AVICs and are characterized by increased contractility, collagen deposition, expression of αSMA, and the more recently identified CDH11. We expected that CDH11 and αSMA would work synergistically to promote disease, or contraction in the AVIC. When we evaluated collagen gel contraction, we were surprised to find WT AVICs were the most contractile (Figure 4.4A); both loss and overexpression of CDH11 resulted in decreased contractility. This suggests that CDH11 expression is delicately balanced and perturbation of its homeostatic level results in dramatic functional changes. Evaluation of αSMA expression revealed an inverse relationship with CDH11 (Figure 4.4B-C), which was unexpected, but can be understood by considering the forces on the AVICs. CDH11 forms bonds stronger than any other cadherin and stronger than the integrity of the cell membrane [229]. If the intracellular tension is increasing with αSMA, the cells may be downregulating CDH11 to have lower

61

intercellular tension. Since our classical myofibroblast markers are inversely regulated, we looked at collagen deposition to further understand the AVIC phenotype. Unsurprisingly, collagen deposition correlated with collagen gel contraction (Figure 4.4D), supporting the finding that the WT AVICs are the most active or myofibroblastic phenotype.

To better understand the consequences of perturbing this CDH11 set point, we investigated catenins, proteins that commonly associate with all cadherins. To our surprise, p120-catenin showed inverse expression with CDH11 (Figure 4.4F). Since p120-catenin acts as a regulator of cadherin expression, preventing internalization by masking an endocytotic signal on the cadherin's intracellular domain, we hypothesized that another cadherin was compensating for loss of CDH11. When we blotted for all cadherins in the WT and CDH11^{-/-} AVICs, we noticed a distinct switch in intensity from a ~120 kDa band to a ~140 kDa band. Upon blotting for a panel of other cadherins, we found that CDH2 matched the higher molecular weight band and was increased in the CDH11^{-/-} AVICs (Figure 4.4G). We then confirmed that across all AVIC lines, there was an inverse relationship between CDH11 and CDH2 expression (Figure 4.4H). The switching between these two mesenchymal cadherins is likely instrumental in the formation of CNs. In the dystrophic calcification hypothesis, cells upregulate CDH11 and are thus very strongly bound to their neighbors. However, when subjected to strain, cells could tear their neighbors' membranes before releasing their homotypic CDH11 bond, leading to apoptosis. The fact that CDH11 is so strong presents a problem in cases of increased strain. Perhaps, there is normally a protective cadherin switching from CDH11 to CDH2 under these circumstances, allowing cells to disengage from their neighbors prior to membrane tearing and eventual creation of a CN. Indeed, we saw this switching *in vivo*, as the 12 month mice had a much higher ratio of CDH2:CDH11 than their younger counterparts (Figure 4.3D-E), possibly to counteract the increased intracellular tensions provided by αSMA (Figure 4.3C) with decreased intercellular

tension. The inverse relationship between CDH11 and αSMA expression is something we believe to hold in the healthy case. Since these mice are not old enough to be considered aged, the high CDH11 we see in calcified human valves could be something that is later onset. Alternatively, these animals could have started with high CDH11 and have been continuously trying to switch to CDH2 to prevent further progression of calcification. To understand when in disease progression CDH11 is most upregulated, and therefore targetable, we would need to evaluate it over time in a disease-prone animal.

CDH11 is unique in that it is the only known cadherin that participates in focal adhesions [167], thereby allowing it to directly sense the substrate in addition to neighboring cells. CDH11 complexes with syndecan-4, a plasma membrane proteoglycan that binds fibronectin. To isolate the cell-substrate interactions from all CDH11-mediated binding, we performed TFM on single and pairs of cells. The interaction forces between pairs of cells resulted in an expected decreasing trend with loss of CDH11 (Figure 4.5C). Like in the population-level gel contraction assay, single WT AVICs generated significantly higher forces than the CDH11 deletion and overexpression AVICs (Figure 4.5A-B). When we normalized these forces to the cell area however, the differences washed out (Figure 4.5D). This suggests that the cell area, and thereby available surface area for focal adhesion attachment, determines how much force the cell exerts. When we assayed the expression of CDH11's focal adhesion partner, syndecan-4, we observed the same trends as gel contraction and force generation – the WT AVICs have the highest expression (Figure 4.5E).

To probe the maturity of these focal adhesions, we quantified focal adhesion length from vinculin staining using custom image analysis tools (Figure 4.5F). CDH11^{-/-} AVICs had significantly longer (Figure 4.5G) but fewer focal adhesions (Figure 4.5I), so total vinculin

expression was unchanged (Figure 4.5H). This suggests that CDH11 plays an important role in the initiation and maturation of focal adhesions, possibly dictating cell spreading and migration. To control for cells' ability to initially bind to the gel, we embedded AVICs in collagen gels at a slightly higher concentration (50,000/gel) and performed a "3D" contraction assay. The first 48 hours look almost identical to the 2D contraction assay and TFM force measurements, with WT AVICs being the most contractile. Although, the CDH11$^{+/-}$ and CDH11$^{-/-}$ AVICs overtake the WT AVICs by 72 hours, and by 96 hours the contractility correlates with αSMA expression (Figure 4.5J). The initial contraction may be mediated by the AVICs' ability to bind the gel, and is therefore dominated by the WT line, but as time progresses, the other AVICs are able to form enough focal adhesions to anchor to the gel and are more contractile because of their much higher expression of αSMA (Figure 4.4C).

Having characterized CDH11-dependent changes under unstimulated conditions, we asked how CDH11 would regulate AVIC phenotype in the presence of disease initiators. TGF-β1 induces myofibroblast differentiation, so we used it as a biochemical model of disease initiation. Treatment induced upregulation of both CDH11 and αSMA, overriding their usual inverse relationship and creating a much more contractile, myofibroblastic phenotype (Figure 4.6A-C). However, though CDH11 and αSMA are increased to similar levels of expression and there is increased collagen gel contraction overall, the cell lines maintain the relationship of loss and overexpression of CDH11 leading to reduced contraction (Figure 4.6D). TGF-β1 also slightly increases CDH2 expression, indicating an overriding of the normal cadherin switching as well (Figure 4.6E). FACS analysis of AVICs also showed that the percentage expressing αSMA increased with TGF-β1 treatment (Figure 4.6F), indicating myofibroblast differentiation of a similar fraction of cells (though higher in the CDH11$^{-/-}$ AVICs). However, there are no changes in the percentage of CDH11-expressing AVICs (Figure 4.6G), likely because nearly all of the

CDH11^{OX} and WT AVICs express some CDH11 without TGF-β1 treatment. Strain and stiffness are crucial mechanical cues in the heart valve, but they direct AVIC phenotype much less than TGF-β1. Under pathologic strain or rigid substrates, myofibroblast markers do not change much (Figure 4.7A-D). Likely, the combination of mechanical and biochemical cues cause a more dramatic response, as we have seen in the context of CN formation *in vitro* [106].

IL-6 secretion is absent in AVICs with reduced or no CDH11 and is increased in CDH11^{OX} compared to WT AVICs (Figure 4.8A). Application TGF-β1 or pathologic strain causes a dramatic, CDH11-dependent increase in IL-6 secretion that mirrors 2D gel contraction and TFM force generation trends (Figure 4.8B-C). Further support of AVIC response being preferentially dictated by TGF-β1 and strain rather than stiffness is shown by the lack of change in IL-6 secretion by the CDH11^{OX} and WT AVICs (Figure 4.8D). To determine whether this secreted IL-6 is regulating the AVICs themselves or signaling to neighboring cells, we probed its receptor, GP130. Interestingly, GP130 expression correlated very well with contractility trends – highest in the WT AVICs (Figure 4.8E). This gives us reason to believe the IL-6 could be acting on the AVICs in a positive feedback or paracrine signaling mode, and evaluation of STAT3 phosphorylation confirms that all lines are responsive to IL-6 (Figure 4.8F). When 3D collagen gels were treated with IL-6, they were more contractile (Figure 4.8G), providing a mechanism by which CDH11 regulates AVIC contractility. Specifically, engagement of CDH11 causes secretion of IL-6, which signals through GP130 to phosphorylate STAT3 and result in contraction. This could even be a mechanism of myofibroblast differentiation, with CDH11-expressing cells secreting IL-6 to activate the contractility of their neighbors. Also, recall that there is an increase in STAT3 expression in 12 month old murine valves (Figure 4.3F), providing evidence of increased IL-6 signaling within the valve.

Downstream of STAT3 is Chi3l1, a secreted inflammatory glycoprotein with unclear function, but association with a variety of cardiovascular diseases [174, 175]. Chi3l1 secretion mirrors contractility trends and thereby presents an interesting future direction of study (Figure 4.8H). Its serum levels have been used to predict prognosis in humans and could be a quick and inexpensive method for tracking or initially screening patients with CAVD, provided that a robust signal in the systemic circulation can be detected. Though it is not likely a disease initiator [175], it could be important in the progression of calcification and therefore a potential therapeutic target. Thus, further study of Chi3l1 and its human analog, YKL-40, is needed.

Together, this data suggests that CDH11 regulates AVIC phenotype through IL-6. Functionally blocking CDH11 could provide a therapeutic alternative to valve replacement by modulating the inflammatory cues leading to a myofibroblastic phenotype.

4.6 – Acknowledgements

Disclosures

The authors have nothing to disclose.

CHAPTER 5

Cyclooxygenase-2 Inhibition Promotes Calcific Nodule Formation by Inducing a Myofibroblast Phenotype in Aortic Valve Interstitial Cells

---

5.1 – Introduction

Over 25% of the US population over 65 is affected by CAVD [7]. This progressive disease eventually requires surgical replacement of the aortic valve, as there are no therapeutic strategies proven effective. This lack of alternatives to surgery is mostly a result of our superficial understanding of the disease mechanism. CAVD is believed to be mediated by AVICs, which become activated by TGF-β1 into myofibroblasts, characterized by increased contractility, collagen deposition, and expression of αSMA and CDH11. These myofibroblasts are then subjected to strain, as is normal in the cardiac valve environment, which results in membrane tearing, leading to apoptosis-mediated cell death. This process has been termed the dystrophic pathway of calcification and was evident in 83% of excised human aortic valves [41], making it the most widespread hypothesized mechanism.

Recent work has identified COX2 expression to be significantly increased in calcified human aortic valves, and its inhibition in a murine model of CAVD to be beneficial in preventing calcification [230]. Interestingly, the COX2 inhibitor used, celecoxib (**CCB**), brand name Celebrex, was predicted and validated to interact with CDH11 [159]. CDH11 is a mechanosensitive transmembrane cell adhesion protein known to have increased expression in calcified human aortic valves [47], to be increased in the AVICs of the Notch1$^{+/-}$ murine model

of CAVD [160], and to be necessary for formation *in vitro* of the CNs characteristic of CAVD [47]. Additionally, recent work has shown that blocking CDH11 with a monoclonal antibody in the Notch1^{+/-} model prevents CAVD progression [208]. We hypothesized that the CDH11 interaction function of CCB was at least as important as its COX2 inhibitory function in preventing CAVD.

To evaluate this hypothesis, we treated porcine AVICs with COX2 inhibitor CCB or its inactive analog also shown to bind CDH11, DMC. Cells were also treated with TGF-β1 to biochemically induce myofibroblast differentiation. AVICs were then subjected to functional assays such as CN formation and collagen gel contraction as well as evaluated for myofibroblast markers αSMA and CDH11.

We found that COX2 inhibition exacerbated CN formation. It similarly caused an increase in both αSMA and CDH11, pointing to an induction of the myofibroblast phenotype. However, CDH11 interaction in the absence of COX2 inhibition prevented TGF-β1-induced CN formation without changing the expression of myofibroblast markers αSMA and CDH11. We conclude that while COX2 inhibition promotes the myofibroblast phenotype and leads to the formation of CNs, the CDH11 interaction function retained by DMC results in fewer CNs. This suggests that DMC would be a safer therapeutic option for patients with CAVD or other CDH11-mediating diseases than would CCB.

5.2 – Methods

Cell Isolation

Porcine aortic valve interstitial cells were isolated from aortic valve leaflets obtained from a local abattoir. Leaflets were excised from pigs within 10 minutes of slaughter and stored in

sterile phosphate-buffered saline (PBS-/-) with 1% ABAM at 4°C to ensure survival. Within three hours of excision, the endothelium was physically removed, and the leaflet was diced and digested in a 600U/ml collagenase solution (Worthington Biochemical Corporation, LS004176) for one hour at 37°C and 5% CO_2. Cell solution was passed through a 100 μm cell strainer to remove tissue chunks and centrifuged at 1500 RPM for 5 minutes before resuspending the pellet in DMEM supplemented with 10% FBS and 1% PenStrep antibiotic. Cells incubated at 37°C and 5% CO_2 with media changes every 2-3 days. Cells were frozen and stored after the second passage and not used past passage 7.

Nodule Assay

AVICs were seeded at 500,000 cells/well in pronectin-coated Flexcell plates in 10μM CCB, 10μM DMC, or in plain media and grown to confluence. Cells were treated with fresh inhibitors ± 1ng/ml TGF-β1 for 24h and then exposed to 15% cyclic biaxial strain for 24 hours via the Flexcell-4000 tension system (Flexcell International Corporation). Calcific nodules were quantified via Alizarin Red Staining. Cells were rinsed in PBS-/-, fixed for 15 minutes in 3.7% neutral buffered formaldehyde, rinsed in diH_2O, and incubated with 1 ml 14mM Alizarin Red Stain (after filtering through a 0.45μm filter). After washing with diH_2O, round nodules of diameter ≥ 100μm and sufficiently intense staining were counted as positive.

Gel Contraction

Type I collagen (Advanced Biomatrix, 5005), 10X PBS-/-, and 0.1M NaOH in an 8:1:1 ratio was mixed and adjusted to pH 7.4 with 0.1 M HCl. 200 μl of this solution was then carefully pipetted into the center of 0.5"-diameter Teflon rings which had been sterilized with 70% ethanol and UV light. After polymerization at 37°C for one hour, 40,000 cells in 200 μl DMEM supplemented with 10% FBS and 1% PenStrep antibiotic (complete media) and 10μM CCB

(Tocris 3786), 10µM DMC (Sigma-Aldrich D7196), or no CDH11 inhibitor were seeded on top of each gel and allowed to adhere at 37°C for 30 minutes. 2 ml of complete media with or without inhibitors and ± 1 ng/ml recombinant porcine TGF-β1 (R&D Systems 101-B1) was then added around the gels and the gels were detached from the rings and the bottom of the tissue culture plate. After equilibration for 30 minutes, free-floating gels were imaged on a Leica dissection scope and this was considered t=0. Gels were imaged at least every 24 hours and media was changed every 48 hours for up to five days. Gel size was quantified via ImageJ [212].

Western Blot

AVICs were seeded at 500,000 cells/well in pronectin-coated Flexcell plates in 10µM CCB, 10µM DMC, or no CDH11 inhibitor in complete media and incubated at 37°C in 5% CO_2 for 24 hours. Cells were treated with fresh inhibitors ± 1ng/ml TGF-β1 for 24 hours and then lysed in RIPA buffer and frozen at -80°C. Protein lysate was linearized by the addition of β-mercaptoethanol and heat (five minutes at 100°C) and run on an 8% or 12% polyacrylamide gel to separate proteins by size. Proteins were then transferred to a nitrocellulose membrane (LI-COR 926) and blocked with Odyssey Blocking Buffer (LI-COR 927) to prevent non-specific antibody binding. Membranes were incubated serially in primary antibody against αSMA (1:1000, Abcam 5694), αTubulin (1:1000, Vanderbilt MCBR Core Lot #2), and CDH11 (1:1000, Cell Signaling Technologies 4442BF) followed by secondary antibodies 680 anti-rabbit (1:20,000, ThermoFisher A10043) or 790 anti-mouse (1:10,000, Jackson ImmunoResearch 115-655-146). Membranes were scanned on a LI-COR Odyssey fluorescent scanner. Proteins were quantified with densitometry (Image Studio Lite) and normalized to αTubulin.

<u>Immunofluorescence</u>

AVICs were plated on fibronectin functionalized coverslips at 50,000 cells/cm^2 in 10µM CCB, 10µM DMC, or no inhibitor and allowed to adhere. Cells were then treated with (plain media, 10µM CCB, 10µM DMC) ± 1ng/ml TGF-β1 for 24h. Cells were fixed and permeabilized in 4% paraformaldehyde with 0.1% Triton X-100 and blocked in 1% bovine serum albumin for 1 hour at 25°C. Coverslips were incubated with primary antibody against cadherin-11 (1:400, Invitrogen 717600) overnight at 4°C. After washing with PBS, 647 anti-rabbit (1:400, ThermoFisher A21245) and a conjugated antibody against αSMA (1:300, Sigma 6198) were added to the coverslips for 1.5 hours at 25°C. Coverslips were washed and then sealed with ProLong Gold antifade reagent with DAPI (Invitrogen P36931) for 24 hours before imaging.

<u>Statistics</u>

All conditions were n ≥ 3 unless otherwise noted. Differences were analyzed via one-way ANOVA in SigmaPlot Version 11.0 and a p-value < 0.05 was considered statistically significant. Data were presented as a mean ± SEM.

5.3 – Results

The CN formation assay is the *in vitro* method most similar to the process of dystrophic calcification *in vivo*. Alizarin red staining of calcium shows the characteristic rounded morphology of CNs (Figure 5.1A). As expected, treatment with TGF-β1 increases the number of CNs under all conditions (Figure 5.1A-B). CCB pre-treatment causes a greater increase in CN number, whereas DMC pre-treatment significantly prevents TGF-β1-induced CN formation (Figure 5.1A-B).
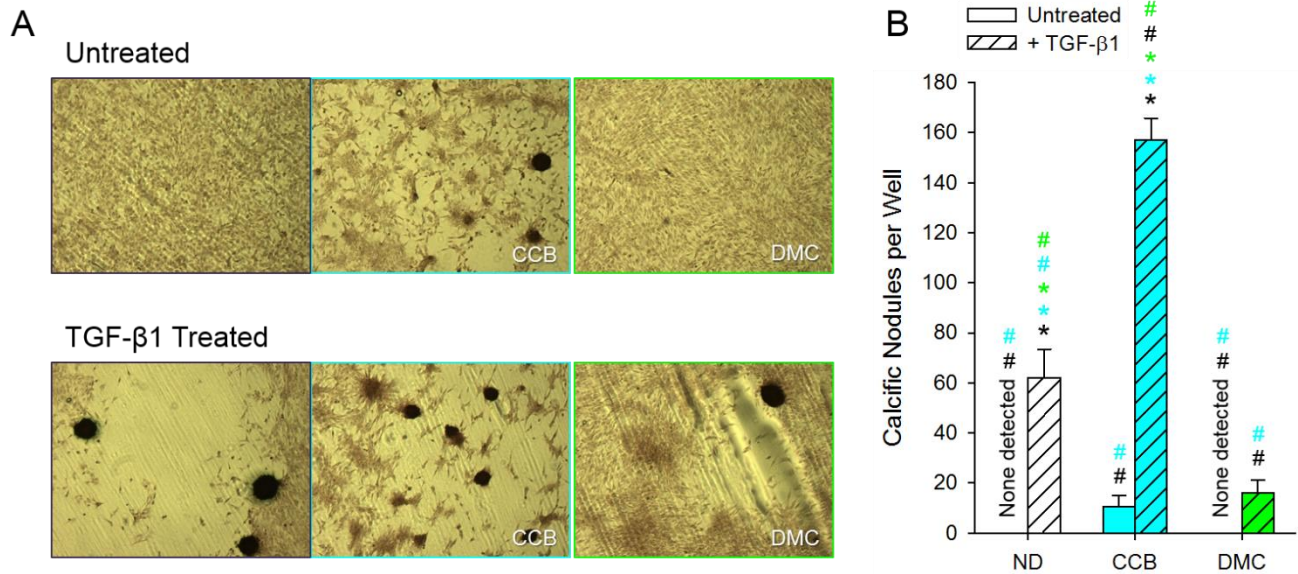
Figure 5.1 – CN formation in AVICs. (**A**) Cyclic biaxial strain and TGF-β1 induce CN formation, identified by Alizarin Red staining. (**B**) Treatment with CCB increases the number of CNs formed in the untreated and TGF-β1 treated cases. DMC treatment reduces the number of TGF-β1 induced CNs. n ≥ 3, ND indicates no drug pretreatment, * indicates $p < 0.001$ different from pre-treatment of indicated color, # indicates $p < 0.001$ different from TGF-β1 treated with pre-treatment of indicated color.

Gel contraction assay revealed that CCB treated AVICs are more contractile than their untreated or DMC treated counterparts (Figure 5.2A). Unsurprisingly, TGF-β1 treatment increased contractility as well (Figure 5.2A).

Expression of myofibroblast markers αSMA and CDH11 was evaluated by western blot (Figure 5.2B-C) and immunofluorescence (Figure 5.2D). Both methods demonstrated a significant increase in both markers only in the CCB pre-treated AVICs (Figure 5.2B-D).
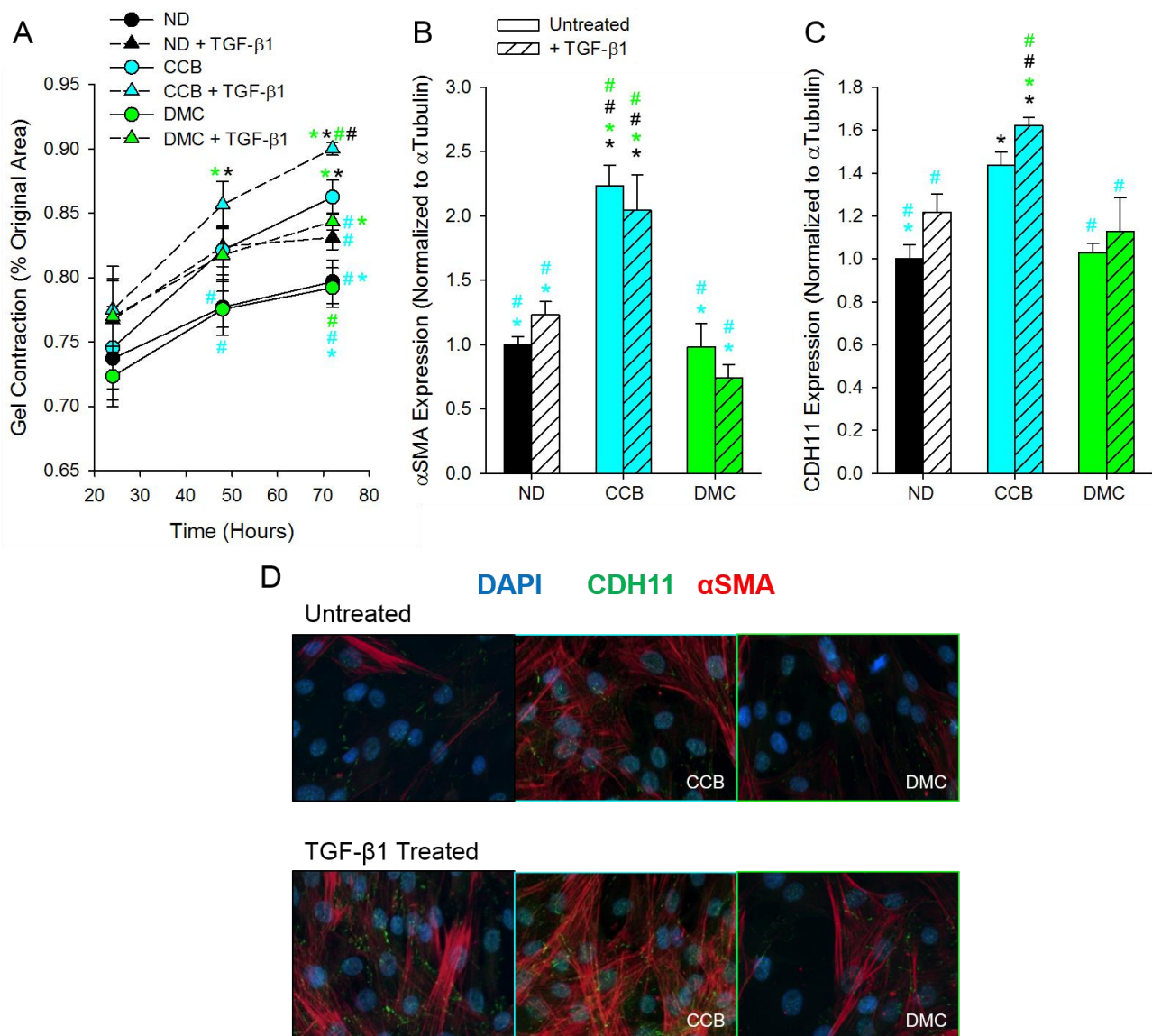
Figure 5.2 – Myofibroblast phenotype of AVICs. (**A**) TGF-β1 treatment decreases collagen gel size, indicating increased contractility. CCB alone also increases contractility to the level of TGF-β1 treatment. (**B**) Treatment with CCB increases expression of αSMA (**B**, **D**) and CDH11 (**C-D**). n ≥ 3, ND indicates no drug pretreatment, * indicates $p < 0.05$ different from pre-treatment of indicated color, # indicates $p < 0.05$ different from TGF-β1 treated with pre-treatment of indicated color.

5.4 – Discussion

We have shown that porcine AVICs respond to COX2 inhibition by upregulating myofibroblast markers αSMA and CDH11, increasing contractility, and most convincingly upregulating CN formation. This supports a protective role for COX2 in dystrophic nodule

formation. Interestingly, treatment of AVICs with CCB's inactive analog, DMC, did not merely show a lack of effect. While DMC treatment does not appear to change the AVIC phenotype – contractility, αSMA expression, and CDH11 expression remain unchanged – it does significantly reduce CN formation. Since we know DMC interacts with CDH11, we hypothesize that this beneficial effect is the result of DMC preventing homotypic interactions of CDH11 between neighboring cells, thereby reducing the tension AVICs can exert on one another, eventually leading to apoptosis and CN formation.

Though COX2 inhibition has been shown in the *Klotho* deficient mouse to lead to decreased aortic valve calcification via an osteogenic mechanism, we have shown that COX2 inhibition can promote CN formation in porcine AVICs through the more prevalent dystrophic pathway of calcification. Also, COX2 is upregulated in human calcified valves but we do not know if this is an initiating condition or response to try to counteract disease. Our data support further investigation of the role of COX2 in more relevant models of CAVD. Human AVIC *in vitro* studies of mechanism and the addition of other murine CAVD models such as Notch1^{+/-} or Apoe^{-/-} treated with CCB and DMC would help clarify whether the role of COX2 is protective or disease-driving.

CHAPTER 6

Valve Interstitial Cells are a Heterogeneous Plastic Population

---

6.1 – Introduction

The aortic valve is unique because it is by far the valve most prone to calcification. Of the over 100,000 valve replacements annually, most are aortic and over 85% of mortality resulting from valve pathologies are aortic in origin (Figure 6.1). To this end, we wanted to determine if the discrepancy in calcification is driven by well-characterized differences in mechanical cues or some other underlying biological variation.
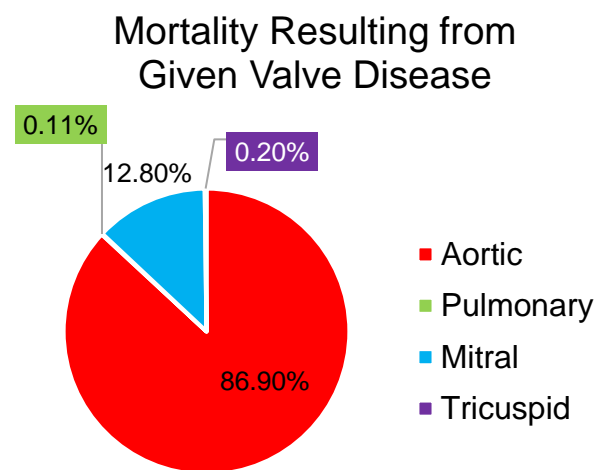
Figure 6.1 – Mortality resulting from given valve disease. Aortic valve pathologies account for almost 87% of all valve pathologies resulting in death [1].

To answer this question, we have evaluated how myofibroblast-like WT VICs from each cardiac valve are. Defining the heterogeneous population of AVICs has been attempted [51, 59, 60], but there is no widely accepted paradigm. There is also debate over whether VICs contained heretofore unidentified subpopulations or have a plastic phenotype [231]. However, the field agrees that VICs are the resident fibroblast-like cells present in all three layers of heart valves and are responsible for maintenance of the valve's ECM. They are also believed to be activated into αSMA-expressing myofibroblasts, the mediators of calcification in CAVD. The purpose of

this work is two-fold: 1) to better define the heterogeneous population of VICs, and 2) to determine if and how the AVICs differ from other VICs.

Better characterization of VICs is necessary to identify key drivers of valvular diseases, which would allow for more specific therapeutic targeting. Identification of differences between VICs may clarify any biological factors contributing to the development of calcification, as it occurs predominantly in the aortic valve. Conversely, lack of significant phenotypic differences between VICs would be a strong indication that the valve environment is a more important driver of disease than the inherent biology of cells.

6.2 – Methods

Isolation of Murine Valve Interstitial Cells

VICs from the aortic (AVICs), pulmonary (PVICs), mitral (**MVICs**), and tricuspid (**TVICs**) valves were isolated from wild-type eight-week-old littermate immorto-mice harboring a temperature-sensitive SV40 tumor antigen gene. After being euthanized in accordance with our IACUC protocol, the murine hearts were excised and the valve leaflets were digested in 2 mg/ml collagenase for 30 minutes at room temperature. Valves were pipetted out of the collagenase solution into DMEM supplemented with 10% FBS and 1% PenStrep antibiotic, and 10 μg/ml recombinant murine γ-interferon (immorto media). Cells were allowed to adhere to 0.1% gelatin-coated 6-well tissue culture treated plates. To activate the SV40 T antigen and allow for sustained growth, the cells were cultured at 33°C and 5% CO_2 in immorto media when not plated for experiments.

Collagen Gel Contraction

Type I collagen (Advanced Biomatrix, 5005) was mixed with 10X PBS-/- and 0.1M NaOH in an 8:1:1 ratio and then adjusted to pH 7.4 with 0.1M HCl. 200 μl of this solution was pipetted carefully into the center of each 0.5"-diameter Teflon ring, which had been ethanol and UV sterilized. After gels were allowed to solidify at 37°C for one hour, 40,000 cells in 200 μl DMEM supplemented with 10% FBS and 1% PenStrep antibiotic (complete media) were seeded on top and allowed to adhere at 37°C for 30 minutes. Complete media was then added around the gels and the gels were detached from the rings and the bottom of the tissue culture plate. After equilibration for 30 minutes, the free-floating gels were imaged on a Leica dissection scope and this was considered t=0. Gels were imaged at least every 24 hours and media was changed every 48 hours for up to five days. Gel size was quantified via ImageJ [212] and differences were analyzed via one-way ANOVA in SigmaPlot Version 11.0. Data were presented as a mean ± SEM and a p-value < 0.05 was considered statistically significant.

Western Blot

Briefly, cells were lysed in RIPA buffer and frozen at -80°C. Protein lysate was linearized by the addition of β-mercaptoethanol and heat (five minutes at 100°C) and then run on an 8% polyacrylamide gel to separate proteins by size. Proteins were then transferred to a nitrocellulose membrane (LI-COR 926) and blocked with Odyssey Blocking Buffer (LI-COR 927) to prevent non-specific antibody binding. Membranes were incubated serially in primary antibody against proteins of interest and secondary antibody conjugated to a fluorescent tag. Membranes were scanned on a LI-COR Odyssey fluorescent scanner. Proteins were quantified with densitometry (Image Studio Lite) and normalized to αTubulin. These values were then normalized to the given animal's aortic valve value to control for inter-animal variability. Differences were analyzed via one-way ANOVA in SigmaPlot Version 11.0 and a p-value < 0.05 was considered statistically

significant. Data were presented as a mean ± SEM. Correlation between protein expression and gel contraction was assessed using Spearman Rank Order Correlation in SigmaPlot Version 11.0. Data were presented as a mean ± SEM and a p-value < 0.05 was considered significant.

Fluorescence-Activated Cell Sorting

WT AVICs were lifted with 0.05% trypsin for no more than 10 minutes and resuspended in HBS FACS buffer (20mM HEPES + 137mM NaCl + 3mM KCl + 1mM $CaCl_2$ + 2% FBS in MilliQ H_2O). Cells were centrifuged at 350 x g for 10 minutes at 4°C, strained through a 100 μm filter (Sigma-Aldrich CLS431752), and aliquoted at 500,000 live cells/tube. Cells were centrifuged at 350 x g for 10 minutes at 4°C and resuspended in 100 μl of primary antibody against CDH11 (1.25 μg/ml 23C6; gift from Michael Brenner) for one hour. Cells were washed in 1 ml HBS FACS buffer with 1:20,000 DAPI (Life Technologies D1306) and centrifuged at 350 x g for 10 minutes at 4°C. Samples were then incubated with 100 μl secondary antibody (1.25 μg/ml IgG1-PE; BioLegend 406607) for 30 minutes in the dark. Cells were washed in HBS FACS buffer and centrifuged at 350 x g for 10 minutes at 4°C before being resuspended in 0.5 ml HBS FACS buffer. If the cells were being analyzed for αSMA as well (all but the initial sort), which requires fixation, the first steps proceeded as above, but the cells were then incubated in Transcription Factor Fixation/Permeabilization working solution (Tonbo Biosciences TNB-0607-KIT) for 30 minutes in the dark. After this, all washes and incubations were performed in Permeabilization buffer (Tonbo Biosciences TNB-0607-KIT) to facilitate diffusion through the fixed cells. Cells were centrifuged at 350 x g for 10 minutes at 4°C and resuspended in 100 μl conjugated antibody against αSMA (1:500 αSMA-647; Novus Biologicals NBP2-34522AF647) for 30 minutes in the dark. Cells were washed in Permeabilization buffer and centrifuged at 350 x g for 10 minutes at 4°C before being resuspended in 0.5 ml FACS buffer and analyzed. After

the initial sort, cell populations were seeded at equal densities, maximizing the number of cells without exceeding 100,000 cells/p100 dish.

6.3 – Results

To evaluate differences in disease potential between VICs, we quantified various defining myofibroblast characteristics. Collagen gel contraction assays revealed no significant differences in VIC contractility (Figure 6.2A), αSMA expression (Figure 6.2B), or CDH11 expression (Figure 6.2C). Since these metrics were normalized within each animal, we were curious if CDH11 or αSMA normalized only to total protein correlated with collagen contraction. While CDH11 was not correlated, αSMA expression correlated significantly with gel contraction at 48 hours (Figure 6.2D). This correlation between αSMA and contraction is expected, though the lack of CDH11 expression correlation with αSMA is surprising.
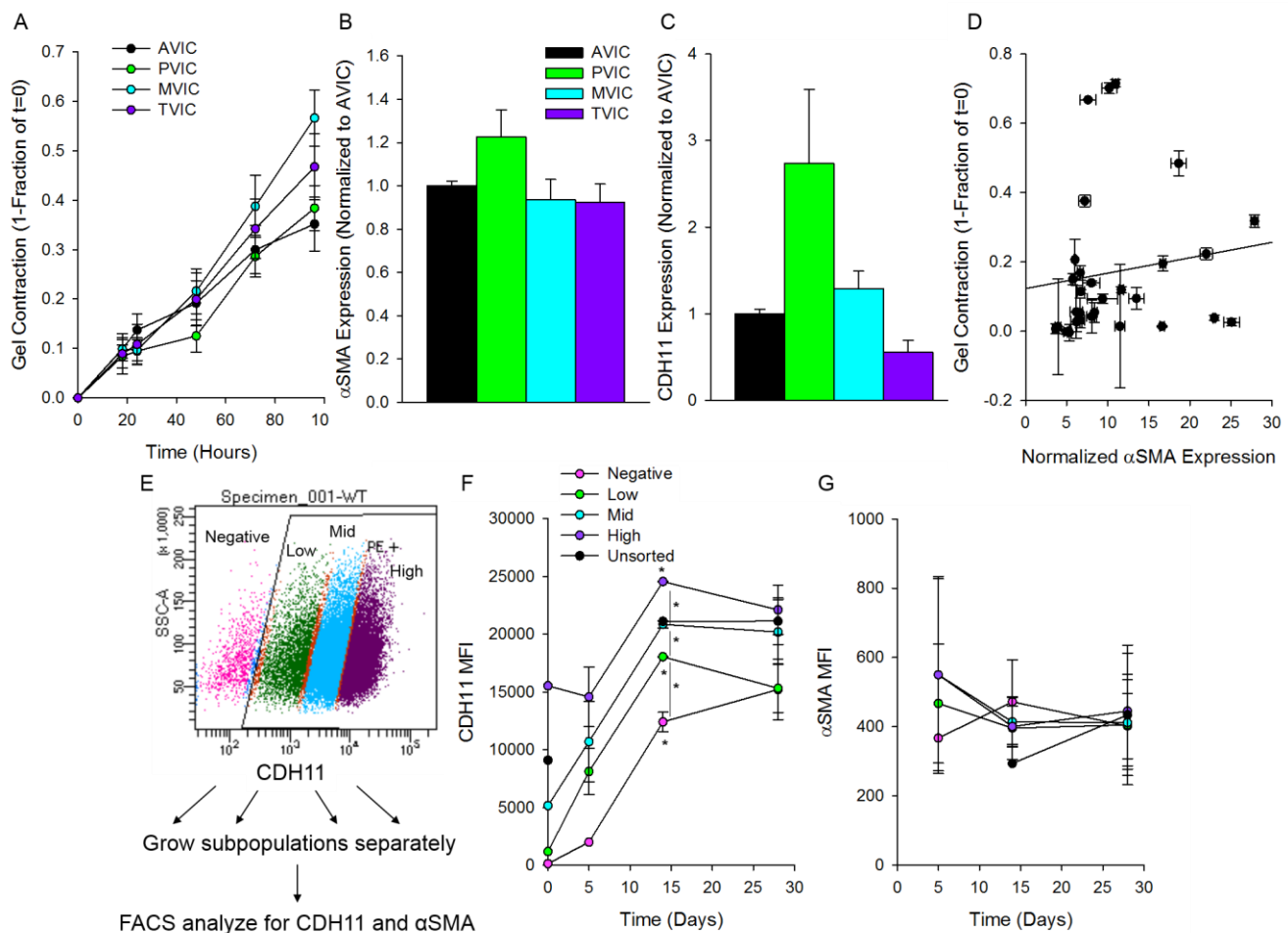
Figure 6.2 – Evaluation of VIC myofibroblasticity and plasticity. VICs from all four cardiac valves showed no significant differences in contractility (**A**), αSMA expression (**B**), or CDH11 expression (**C**). αSMA expression normalized to αTubulin was significantly correlated with gel contraction at 48 hours (**D**). Division of WT AVICs by CDH11 expression (**E**) yielded subpopulations that maintained varied CDH11 expression out to 28 days (**F**), but showed no differences in αSMA expression as early as five days (**G**). * = p-value < 0.05 compared to unsorted population unless otherwise noted.

We were also interested in whether CDH11 expression clearly defines a distinct cell population within VICs or if the VIC phenotype is plastic. To test this, we sorted AVICS into low-, mid-, high-, and non-CDH11 expressing subpopulations and cultured them separately, then reanalyzed them at later time points for changes to their basal expression of CDH11 and αSMA (Figure 6.2E). We found that αSMA expression was not significantly different between subpopulations within five days of sorting (Figure 6.2G). However, CDH11 subpopulations still had distinct CDH11 expression at 14 days (Figure 6.2F). Not until nearly a month after sorting

were the populations no longer significantly different in CDH11 expression. This indicates that the VIC population is heterogeneous and the phenotype is relatively plastic. Of importance, changes to the valve environment tend to be slowly progressing, but irreversible. The slowly worsening valve environment coupled with the VICs' plasticity could be a key relationship in the positive feedback mechanisms that likely drive CAVD (i.e. strain leads to increased αSMA expression, which correlates with contractility, thereby applying more strain on neighboring VICs).

6.4 – Discussion

We have addressed the importance of cell identity within VIC populations and find no significant differences between interstitial cells. This suggests a crucial role of the local valve environment; environmental factors are far more potent drivers of calcification than any inherent differences between interstitial cells of different valves. While this work investigated differences in baseline VIC phenotype, significant changes may emerge in response to disease initiating stimuli, such as TGF-β1, 15% strain, and IL-6. Future studies should investigate the differential response to these stimuli in the VICs from each valve.

We also probed the plasticity of the myofibroblast phenotype in AVICs. Sorting the WT AVICs by CDH11 yielded results that support the hypothesis that AVICs are a heterogeneous population of fibroblasts and myofibroblasts that transition between phenotypes relatively quickly. We demonstrated that αSMA correlates with contractility, two key indicators of myofibroblasts, and that αSMA expression is not different between any groups within five days

of sorting. CDH11 does tend to increase over time, and this is because of increasing seeding density. The subpopulations were seeded at the same densities as each other, but especially at early time points, cells were limited, resulting in unusually low CDH11 expression. CDH11, on the other hand, takes longer to return to its homeostasis. This is in part because we sorted by CDH11, so the subpopulations were better delineated at the experiment's start, but also possibly an intrinsic characteristic of CDH11. This provides some support for targeting CDH11 as a therapeutic, as is being investigated for CAVD [208]. If the plasticity of CDH11-expressing AVICs is not particularly high, then blocking with a functional blocking antibody would be effective for longer periods of time (assuming the antibody binding kinetics are strong and slow). Theoretically, this means longer times between treatments because the functionally-inhibited, CDH11-expressing AVICs would stay functionally inhibited and the non-CDH11-expressing AVICs would take a substantial amount of time to upregulate their CDH11 expression.

6.5 – Acknowledgements

CHAPTER 7

Generation of an Inducible and Titratable Murine Cadherin-11 Vector

---

7.1 – Design Rationale

Though VICs are the most biologically relevant cell to CAVD, their heterogeneous nature and complexity introduce variables to any *in vitro* experiment. These cells existed in an animal throughout its development and for enough time to allow compensatory mechanisms to take hold. While they are critical for understanding cardiac valve biology, they are perhaps too complex to easily clarify the immediate reactions to CDH11 perturbation. To address this concern, we have designed a plasmid that allows for induction and titration of a mEos3.2-tagged murine CDH11. The mEos3.2 tag is a monomeric photoactivatable fluorescent protein that normally fluoresces in the GFP channel (506nm/519nm), but upon exposure to 405 nm laser for 30 seconds, photoconverts to fluoresce in the TxRed channel (573nm/584nm) [232]. Mitochondria tagged with mEos3.2 in a HeLa cell is imaged before and after photoconversion (Figure 7.1B). This enables tracking of CDH11 recycling and potentially creative live-cell imaging.

7.2 – Methods

A full-length murine CDH11 open reading frame was amplified from an existing vector using primers which preserved a 5' NheI restriction site, disrupted the terminal stop codon, and

incorporated a 3' AgeI site for the fragment to be cloned upstream and in frame with mEos3.2 (Figure 7.1C). This mCDH11-mEos3.2 fragment was then cloned into the SparQ vector (System Biosciences QM800A-1) with NheI/SwaI (Figure 7.1A). The vector was then verified via sequencing (Figure 7.1D).
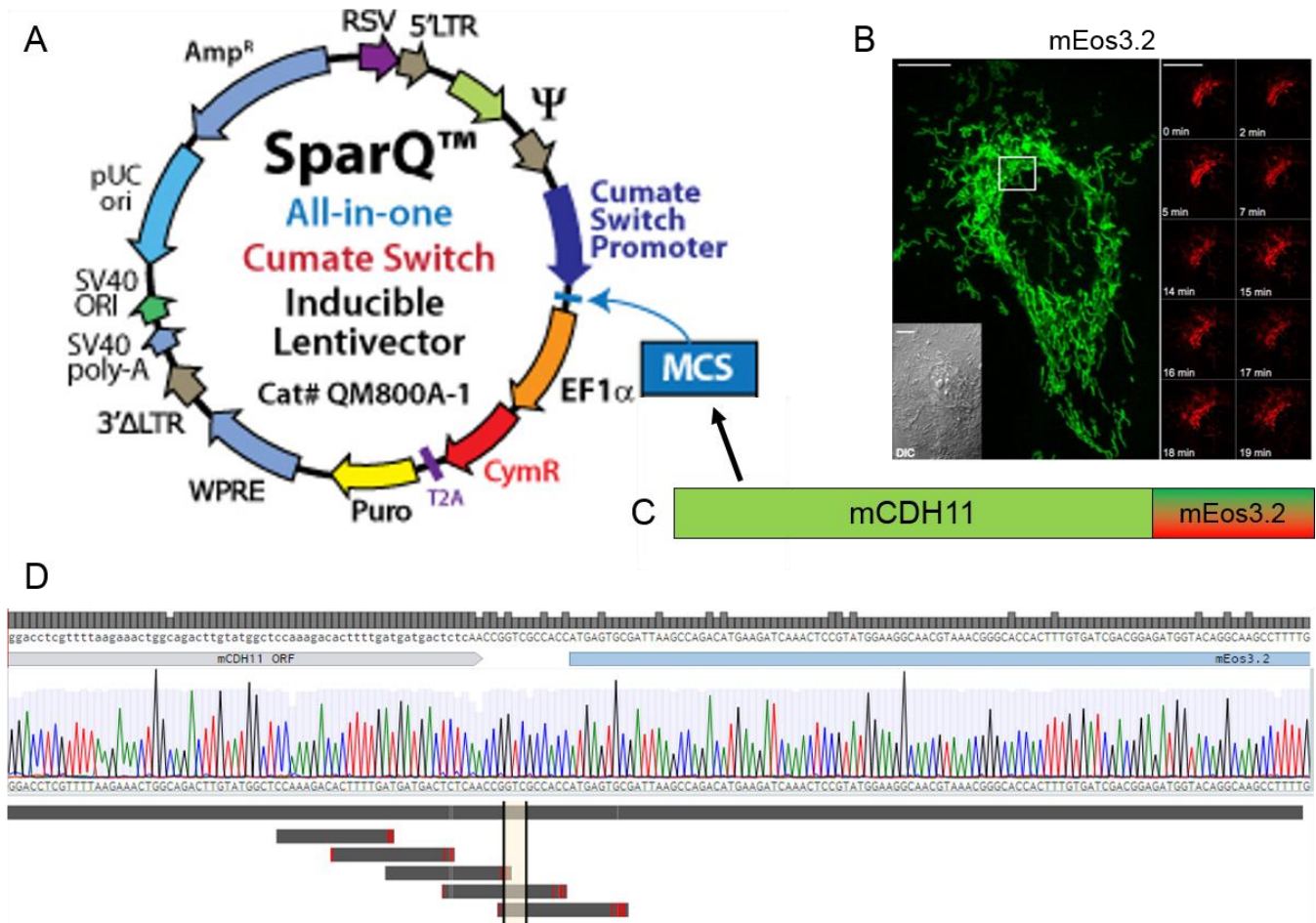
Figure 7.1 – Design of Cumate-mCDH11-mEos3.2 vector. An inducible, titratable, mEos3.2-tagged murine CDH11 vector was generated by utilizing the SparQ cumate system (**A**) and inserting mCDH11 tagged with a photoactivatable protein, mEos3.2 (**B-C**). The sequence was verified and the mCDH11 ORF through mEos3.2 start codon is displayed (**D**). Scale bars in B are 10 μm on left and 5 μm on right. B adapted from [232].

7.3 – Acknowledgements

We thank Mark J. Vander Roest for help in the creative vector design.

CHAPTER 8

Impact and Future Directions

___

8.1 – Societal Impact

The overarching theme of these projects was to better understand the contribution of CDH11 to CAVD. To approach this, we tackled three primary questions. First, how does blocking CDH11 function *in vivo* affect aortic valve health? Second, what is CDH11 doing to the resident valvular cells to prevent calcification? Third, are the valve interstitial cells inherently different between the four cardiac valves, and does this contribute to the discrepancies in calcification prevalence of each valve? Together, this work gives us a more complete understanding of CDH11's mode of action in CAVD.

To investigate the *in vivo* consequences of reducing CDH11 in CAVD, we employed a murine model of heritable, and possibly idiopathic, disease. Mutations in Notch1 in humans are a cause of bicuspid aortic valves, which are much more prone to aortic stenosis [171]. Luckily, Notch1 haploinsufficiency in mice also predisposes them to CAVD [160]. When we aged *Notch1$^{+/-}$* mice on a high-fat/high-cholesterol diet, their aortic valve velocity was markedly higher than *Notch1$^{+/+}$* (WT) values [208]. We then demonstrated that the addition of CDH11 haploinsufficiency resulted in WT-level velocities, indicating that reduction of CDH11 expression prevents CAVD. More promising, we demonstrated an effect in diseased, *Notch1$^{+/-}$*, mice treated with a functional blocking antibody against CDH11 (SYN0012) [208]. Mice treated systemically

with the CDH11 blocking antibody had much lower maximum aortic flow velocities and higher ejection fraction velocity ratios. This corroborative evidence motivated a deeper understanding of the mechanism by which CDH11 deletion prevents CAVD.

Since AVICs are believed to mediate CAVD and diseased human leaflets had higher CDH11 expression, we investigated the role of CDH11 in AVICs. The most common hypothesis of calcification progression is the dystrophic pathway. Briefly, it involves TGF-β1-induced transdifferentiation of AVICs into myofibroblasts, which are characterized by increased contractility, collagen deposition, and CDH11 and αSMA expression. These more active cells have increased intracellular and intercellular tension, resulting from αSMA and CDH11, respectively, and upon exposure to strain, can tear. This induces apoptosis-mediated cell death and the beginning of a CN. Our investigation of CDH11 in AVICs revealed a complex story wherein CDH11 normally regulates αSMA and focal adhesions, maintaining a balance in intracellular, intercellular, and cell-substrate tension, but can be overridden by disease initiators (TGF-β1 and strain) to increase inflammatory signaling (IL-6) and contractility. This key role of IL-6 in CAVD has not been well studied and provides a potential therapeutic target.

To address the question of nature versus nurture, we isolated VICs from all four cardiac valves and characterized their phenotypes. The dramatically higher prevalence of aortic valve pathologies suggested that if VIC biology is inherently different between the cardiac valves, the AVICs would demonstrate higher levels of myofibroblast markers. However, we determined that there are no significant differences between the contractility, CDH11 expression, or αSMA expression of the VICs. There was a correlation between αSMA expression and contractility, but

this was independent of valve source. Investigation of VIC phenotype also focused on the plasticity of these cells. Given that CDH11 and αSMA are myofibroblast markers and any disease-promoting subpopulation would likely have one or both of these proteins, WT AVICs were evaluated on their expression via FACS. Since CDH11 is a transmembrane protein and clearly regulates αSMA expression, it was the ideal candidate for sorting. After sorting by CDH11 expression, WT AVICs were expanded, controlling for seeding density, and re-analyzed. Within five days, there were no differences in αSMA, and within 28 days, CDH11 expression had evened out. It thus appears that the VICs are somewhat plastic – they can transition between phenotypes, but it takes a substantial amount of time. This implies that if we were able to target the disease-initiating cells, treatment could occur on the order of monthly instead of daily doses.

Finally, we have created a powerful genetic tool for study of CDH11 in the future. Namely, the inducible and titratable cumate vector containing mEos3.2-tagged murine CDH11 can be infected into a variety of cells, but should be evaluated in L cells. L cells are murine fibroblasts that contain all of the catenin machinery to allow cadherins to function, but no cadherins. Thus, infection with the Cumate-mCDH11-mEos3.2 vector would allow independent study of CDH11's effect on fibroblasts.

This work has substantially progressed our understanding of the contributions of CDH11 to VIC biology and CAVD, and the importance of valve environment compared to VIC biology versus valve environment to disease progression.

8.2 – Future Directions

The work presented here significantly deepens our understanding of CDH11 mechanobiology in CAVD. We have shown relevance for reducing CDH11 function *in vivo*, we have partially clarified its mechanism, and we have a better understanding of VIC phenotype. However, more work is necessary to understand the mechanism of CDH11 blockade. We have focused on AVICs because they are believed to be mediators of CN formation. However, the *in vivo* studies were knockdowns since conception. Therefore, there could be important contributions to valve health originating from other cells. AVECs line the valves and can secrete a variety of signaling factors to influence AVIC behavior. A good next step would be an *in vitro* co-culture model with AVICs embedded in a gel and AVECs seeded on top. Within this system, one could perturb CDH11 expression in either or both cell types as well as characterize the effects IL-6 has on AVEC secretory profiles. Of note, isolation of murine AVECs is not trivial. We have attempted this with some success, but the small valve size coupled with the propensity of AVICs to proliferate much more quickly makes it difficult to obtain a pure endothelial population. This would likely require rounds of clonal expansion and cell sorting (i.e. for CD31).

Another cell population important to CAVD are immune cells, particularly macrophages and T cells [233]. Interestingly, IL-6 may regulate the balance between M1 (pro-inflammatory) and M2 (anti-inflammatory) macrophages. IL-6 knockout mice had fewer M2 macrophages in their skin [234]. We also know that M2-polarized macrophages secrete increased IL-6 [235], providing a positive feedback mechanism for M2 polarization. Very little data exists surrounding T cells and CAVD, but a recent study identified a role for CD8+ cells in preventing calcium resorption and thereby leading to calcification [236]. Also, IL-6 is known to cause differentiation

of CD4+ T cells into Th-17 cells, pro-inflammatory T-helper cells [237]. Whether IL-6 promoting contraction in the AVICs, leading to an anti-inflammatory macrophage phenotype, or promoting a pro-inflammatory T cell phenotype is most important to CAVD progression remains to be tested. Investigating CAVD in IL-6 knockout mice or using anti-IL-6 therapeutics like tocilizumab in murine models could clarify IL-6's dominant mode of action.

This work also supports investigation of Chi3l1, or YKL-40, as a potential biomarker. YKL-40 has recently been proposed as a biomarker for other cardiovascular diseases and seems sensitive to specific conditions, for example, higher plasma levels were associated with ischemic stroke, but not myocardial infarction [175]. This would be a straightforward clinical trial, as it would involve only echocardiograms (which are likely being performed on CAVD patients anyway) and blood draws.

Another clinical trial supported by this work is the inhibition of CDH11 function. This is actually already underway, but for the treatment of rheumatoid arthritis. The humanized version of SYN0012, RG6125, is a monoclonal antibody that blocks CDH11 and is currently in phase II clinical trials [238]. Assuming it receives FDA approval, the next step should be a trial to evaluate its effect on CAVD and then submission as a secondary indication. With the imminent increase in CAVD prevalence, there is a continuously growing motivation to provide effective noninvasive therapeutics.

STATISTICAL ANALYSIS

AVICs were obtained from littermate, or at least cousin-mate, controls to minimize animal-dependent effects. Only AVICs, PVICs, MVICs, and TVICs from the same mouse were compared. The data were reported as the mean of all replicates, and error was reported as the standard error of the mean (sample sizes < 30) unless otherwise noted. Comparisons between groups were made using One-way ANOVA and post-hoc Holm Sidak tests in SigmaPlot Version 11.0 and a p-value < 0.05 was considered significant. If the data were determined to be non-normal, non-parametric tests were employed to determine statistical differences.

PROTECTION OF RESEARCH SUBJECTS

No human subjects were included in this work and experiments were designed to minimize the number of animals needed to perform the work. Creation of immortalized cultures of VICs decreased variables between cell experiments and lessened the number of animals needed to acquire cells. All of the procedures of this study were performed with the recommended PPE and were all under bio-safety level 2, so there was minimal risk to human researchers. The goal of this research is to give insight into the dynamic process of CDH11 mechanotransduction in valvular cells and offer insights for the development of potential therapeutic strategies.

APPENDIX A

Antibodies Used for Protein Visualization

Table A.1 – Antibodies used for protein visualization. Source and concentration information for various antibodies used in this work. WB indicates western blot; IF indicates immunofluorescence; FACS indicates fluorescence-activated cell sorting.

Target antigen	Vendor or Source	Catalog #	Working concentration
αSMA	Abcam	5694	WB: 1:1000
αSMA-Cy3	Sigma	6198	IF: 1:400
αSMA-647	Novus	NBP2-34522AF647	FACS: 1:500
αTubulin	Vanderbilt MCBR Core	Lot #2	WB: 1:1000
β-catenin	BD	610154	WB: 1:1000
Cadherin-1	BD	610182	WB: 1:1000
Cadherin-2	Sigma	2542 (GC-4)	IF: 1:100 WB: 1:1000
Cadherin-5	Abcam	33168	WB: 1:1000
Cadherin-11	Cell Signaling Technologies	4442BF	IF: 1:50 WB: 1:1000
Cadherin-11	Michael Brenner (Mouse IgG1)	23C6	FACS: 1.25 µg/ml
IgG1-PE	BioLegend	406607	FACS: 1.25 µg/ml
IL-6	Abcam	6672	IF: 1:50
Pan-Cadherin	Invitrogen	PA5-16766	WB: 1:100
p120-catenin	Life Technologies	339700	WB: 1:1000
STAT3	Cell Signaling Technologies	9139	IF: 1:800
Syndecan-4	Abcam	24511	WB: 1:250
Vinculin	Sigma	V9131 (hVIN-1)	IF: 1:400
488 anti-mouse	Jackson ImmunoResearch	715-545-150	IF: 1:400
647 anti-mouse	Jackson ImmunoResearch	715-605-150	IF: 1:400
647 anti-rabbit	ThermoFisher	A21245	IF: 1:400
680 anti-rabbit	ThermoFisher	A10043	WB: 1:20,000
790 anti-mouse	Jackson ImmunoResearch	115-655-146	WB: 1:10,000

APPENDIX B

Details of Traction Force Microscopy Analysis

Methods for Traction Force Microscopy Image Analysis

Traction Force Microscopy. High-resolution traction force microscopy (TFM) was used to quantify the cell-matrix forces generated by each cell line (CDH11^{OX}, WT, CDH11$^{+/-}$, and CDH11$^{-/-}$). TFM was performed using experimental and computational methods similar to those described previously [213-215]. The details of the methods are described below:

Preparation of Polyacrylamide Gel Substrates. Polyacrylamide (**PAA**) gels embedded with fibronectin were adhered to glass coverslips for TFM analysis as described previously [219]. Briefly, 35 mm glass-bottom dishes (MatTek P35G-0-14-C) were coated with 0.1 N NaOH for 5 minutes prior to treatment with 3-aminopropyltrimethoxysilane (Sigma-Aldrich 281778) for 10 minutes at room temperature. Following multiple washes with ultrapure water, dishes were treated with 0.5% glutaraldehyde solution (0.5% in 1X PBS; Polysciences 01909) for 30 minutes at room temperature. A polyacrylamide solution consisting of 169 µL ultrapure water, 300 µL 40% acrylamide, and 300 µL 2% bis-acrylamide was combined with 230 µL human plasma fibronectin (1 mg/mL in ultrapure water; Life Technologies 33016-015) and 8 µL of 200 nm red fluorescent microspheres (excitation/emission of 580/605 nm; ThermoFisher F8810). To ensure even polymerization, the solution was then mixed with 1 µL acrylic acid NHS ester (10 mg/ml in ultrapure water; Sigma-Aldrich A8060), 1 µL APS (100 mg/ml in DMSO; Sigma-Aldrich D8418), and 2 µL TEMED (Bio-Rad 161-0800) prior to placement on the glass-bottom dishes (8.48 µL for ~75um thickness gel). This formulation results in a rigid PAA gel (12% acrylamide and 0.6% bis-acrylamide) with an elastic modulus of 22692 Pa [214, 218]. Embedded fluorescent microspheres act as fiducial markers for calculation of the gel displacement field between

deformed and reference images. Cells were plated on PAA gels and incubated in complete media (DMEM supplemented with 10% FBS and 1% PenStrep antibiotic) overnight to allow for adequate attachment.

Image Acquisition. Prior to imaging, cells were placed in pre-warmed L-15 medium and equilibrated for at least one hour in an environmental microscope chamber at 37 °C with high humidity. Cell positions were recorded using an automatic stage. Phase contrast images showing cell boundaries and fluorescent images showing the corresponding bead distribution (deformed) just below the gel surface were acquired using a Nikon Eclipse TE2000-E inverted microscope with a 40X 0.75 NA Plan Fluor objective (0.162 µm/pix). Following acquisition of all deformed images, cells were detached from the PAA gel using Triton-X 100 (Alfa Aesar A16046). After 5 minutes, fluorescent images of the reference (undeformed) bead distribution at the same spatial locations were acquired for each cell, allowing for calculation of the cell-induced gel displacement.

To reduce the mechanical effects from neighboring cells and the underlying glass coverslip, image acquisition was restricted to flat, isolated cells on a smooth section of the PAA gel (without inclusions or wrinkling) that had >25µm thickness. Single cells and contacting cell doublets were included in the current study.

Calculation of Bead Displacements. Displacement fields were calculated from corresponding deformed/undeformed bead distribution images using a subpixel correlation by image interpolation (SCII) approach [213]. Briefly, potential bead locations in each image were identified based on fitted Gaussian profiles in order to reduce the influence of fluorescence intensity variations on the quality of image correlation. The $(2L + 1) \times (2L + 1)$ pixel intensity window surrounding each bead in the reference image I_U was matched with a corresponding

intensity window in the deformed image I_D using a correlation-based image tracking procedure. When using a SCII approach for point tracking, linearly preinterpolated windows around each bead location were compared using a normalized cross correlation coefficient S for each pixel coordinate (x_o, y_o),

$$S(Ru_x, Ru_y)\big|_{x_o,y_o} = \frac{\sum_{i,j=-RL}^{RL}\left(I_U^R(i,j)\big|_{x_o,y_o} - \overline{I_U}\right)\left(I_D^R(i+Ru_x,j+Ru_y)\big|_{x_o,y_o} - \overline{I_D}\right)}{\sqrt{\sum_{i,j=-RL}^{RL}\left(I_U^R(i,j)|_{x_o,y_o} - \overline{I_U}\right)^2}\sqrt{\sum_{i,j=-RL}^{RL}\left(I_D^R(i,j)|_{x_o,y_o} - \overline{I_D}\right)^2}} \quad , \tag{1}$$

where u_x and u_y denote directional pixel step sizes, L is related to the template window size in pixels, R denotes a refinement factor (typically $R = 10$), and i and j denote neighboring pixel values between $-RL$ and $+RL$. Overbars denote the mean intensity value of the current template window. The preinterpolated images I_U^R and I_D^R are constructed as a bilinear interpolation of the original pixel intensities such that

$$I^R(i,j) = (1-x)(1-y) \times I(i_R, j_R) + x(1-y) \times I(i_R + 1, j_R)$$
$$+ (1-x)y \times I(i_R, j_R + 1) + xy \times I(i_R + 1, j_R + 1) \tag{2}$$

where $i_R = i/R - x$ and $j_R = j/R - y$ and x and y are the fractional part of i/R and j/R, respectively. Subpixel resolution is achieved by computing the maximum of a parabolic fit to the pixel neighborhood surrounding the pixel location with the highest correlation coefficient value [213]. Global translational offsets between images were corrected by subtracting the median of all identified bead displacements. Following image correlation, bead displacements were interpolated onto a regular grid for traction reconstruction. All bead displacement calculations were performed using a set of computational tools provided in an open-source TFM analysis package [213].

Traction Force Reconstruction. Cell-dependent displacement fields were combined with known mechanical properties of the rigid PAA gel to identify surface traction forces using a regularized Fourier Transform Traction Cytometry (reg-FTTC) framework. Briefly, as in [215], for a homogeneous, isotropic, linear, elastic material, the in-plane displacement $\mathbf{u}(\mathbf{x})$, where $\mathbf{x}$ is the 2D spatial coordinate $\mathbf{x} = (x, y)$, is related to in-plane traction $\mathbf{T}(\mathbf{x}')$ via the Green's function $\mathbf{G}(\mathbf{x}, \mathbf{x}')$, such that

$$\mathbf{u}(\mathbf{x}) = \int_{\Omega} \mathbf{G}(\mathbf{x} - \mathbf{x}')\mathbf{T}(\mathbf{x}')d\mathbf{x}' \ , \tag{3}$$

where Ω denotes the domain within the cell boundary and $\mathbf{x}'$ denotes any spatial coordinate where tractions are generated. Given a known displacement field, identification of the corresponding traction field requires inversion of Eq. 3. For sufficiently thick solids, the material can be approximated as an isotropic elastic half space and Eq. 3 can be solved using the Boussinesq solution to Green's function [216]. While the solution to this linear system of equations is computationally expensive in the spatial domain, Fourier transformation has become increasingly useful due to the property that convolution in the spatial domain becomes multiplication in the Fourier domain [217]. Thus, Eq. 3 becomes

$$\widetilde{\mathbf{u}}(\mathbf{k}) = \widetilde{\mathbf{G}}(\mathbf{k})\widetilde{\mathbf{T}}(\mathbf{k}) \ , \tag{4}$$

where $\sim$ denotes a Fourier transformed quantity and $\mathbf{k}$ represents the spatial coordinate, or wave vector, in the Fourier domain such that $\mathbf{k} = (k_x, k_y)$. The Boussinesq solution $\widetilde{\mathbf{G}}(\mathbf{k})$ can be expressed as (in tensor form)

$$\widetilde{\mathbf{G}}(\mathbf{k}) = \frac{2(1 + v)}{Ek^3}\begin{pmatrix} (1 - v)k^2 + vk_y^2 & -vk_xk_y \\ -vk_xk_y & (1 - v)k^2 + vk_x^2 \end{pmatrix} \ , \tag{5}$$

where E and v are the Young's modulus and Poisson's ratio of the PAA gel, and k denotes the magnitude of the $\mathbf{k}$ such that $k = sqrt(k_x^2 + k_y^2)$. It has been shown that the Fourier transform alone does not provide an accurate traction reconstruction [222]. Indeed, a reasonable solution to the ill-defined inverse identification of traction forces on the surface of the PAA gel, requires that a regularization parameter λ be used to optimize the equation

$$\min\left\{\left\|\widetilde{\mathbf{G}}\widetilde{\mathbf{T}} - \widetilde{\mathbf{u}}\right\|^2 + \lambda^2\left|\widetilde{\mathbf{T}}\right|^2\right\} \quad , \tag{6}$$

where double brackets denote the L2-norm and single brackets denote the L1-norm. Using a 0th order Tikhonov regularization, the value of λ defines a threshold below which contributions from traction singularities do not affect the solution. Larger values of λ often result in smoother traction fields due to the bias toward minimizing the solution norm ($\left|\widetilde{\mathbf{T}}\right|^2$) whereas small values of λ lead to more discontinuous tractions due to the bias toward minimizing the residual norm ($\left\|\widetilde{\mathbf{G}}\widetilde{\mathbf{T}} - \widetilde{\mathbf{u}}\right\|^2$) [220].

While there are multiple known methods for identifying an appropriate regularization parameter value – from the chi-curve [222], the L-curve [220], or from a Bayesian maximum a posteriori estimator of the traction [221, 239, 240] – here, λ was chosen based on optimal L1-regularization of the L-curve [213]. Values of λ were independently determined for each cell with an average value of $\lambda = 2.89 \times 10^{-4}$ over all cells. Following optimization of Eq. 6 with the optimal value of λ, traction forces in the spatial domain were recovered by inverse Fourier transform. All traction force reconstructions were performed using a set of computational tools provided in an open-source TFM analysis package [213].

Mechanical Metrics. Given the reconstructed traction fields in the spatial domain, the total force exerted by each cell was quantified as an integral of the traction magnitude over the bounded cell area [223]. Specifically,

$$|F| = \int_{\Omega} |\mathbf{T}(\mathbf{x})| d\mathbf{x} \equiv \iint_{\Omega} \sqrt{T_x(x,y)^2 + T_y(x,y)^2} \, dxdy \quad , \tag{7}$$

where $T_x(x,y)$ and $T_y(x,y)$ denote components of the local traction vector $\mathbf{T}(\mathbf{x})$ at any spatial location $\mathbf{x} = (x,y)$ contained with the cell boundary Ω. Cell area A was defined as the number of pixels in or on the cell boundary and was scaled based on a known pixel calibration of $dx = dy = 0.162$ μm/pix. The cell area A (in μm²) was used to normalize total force measurements (in nN) such that all normalized measurements have a unit of kPa, similar to stress.

Additionally, for cell doublets, cell-cell interaction forces were estimated from the traction imbalance that arises due to partitioning of the traction field along the cell-cell contact border [224]. Briefly, cell-cell interfaces were identified in phase contrast images and used to partition the total boundary into two separate cell boundaries. The components of the resultant force vector $\mathbf{F}_i = (F_{x,i}, F_{y,i})$ within each cell boundary Ω_i were computed as

$$F_{x,i} = \iint_{\Omega_i} T_{x,i}(x,y)dxdy, \quad F_{y,i} = \iint_{\Omega_i} T_{y,i}(x,y)dxdy \quad , \tag{9}$$

for $i = 1, 2$. Since the cell doublet is in mechanical equilibrium prior to partitioning of the traction field, subdivision of the cell boundary should result in equal and opposite forces between cells. Differences between resultant force vectors $\mathbf{F}_1$ and $\mathbf{F}_2$ must therefore be attributed to forces acting at the cell-cell interface. We estimated the cell-cell interaction force vector $\mathbf{F}_{cc}$ as

$$\mathbf{F}_{cc} = \frac{\mathbf{F}_1 - \mathbf{F}_2}{2} \quad ,$$
(10)

where the cell-cell interaction force magnitude was computed as $|\mathbf{F}_{cc}| = sqrt(F_{cc,x}^2 + F_{cc,y}^2)$. Analogous to the total force, measured cell-cell interaction forces (in nN) were normalized by contact border length (in μm) such that all normalized measurements have a unit of nN/μm, similar to tension.

Focal Adhesion Immunofluorescence Analysis

Focal Adhesion Immunofluorescence Analysis

Image Quantification. Immunofluorescence staining for vinculin was performed in fixed cells to identify locations of focal adhesions. Acquired images were processed, using custom Matlab scripts, to quantify the number and length of focal adhesions in each field of view (n = 7 per group). Briefly, grayscale fluorescence images were preprocessed to correct for non-uniform background intensity prior to global contrast enhancement. Background was corrected by subtraction of the corresponding grayscale morphological opening operation with a disk of 10 pixel radius. Remaining background was further reduced by application of a Gaussian filter with $\sigma = 3$. Preprocessed images underwent adaptive thresholding to generate a binary mask highlighting potential focal adhesion locations. Focal adhesion boundaries were extracted from binary masks, and the boundaries in contact with image borders, nuclei borders, or with low median intensity values (based on Otsu's method) were excluded from further analysis. Candidate boundaries were then assessed for potential contacting adhesions and, when applicable, were separated using a previously described object separation algorithm based on the convex hull and watershed transform [211]. Finally, individual boundaries were extracted and focal adhesion length was defined as the major axis length of the corresponding best-fit ellipse to each boundary (>250 per image).

Statistics. Distributions of focal adhesion properties (number and length) were assessed for normality using the one-sample Kolmogorov-Smirnov test. All metrics were found to follow a lognormal distribution, thus statistical differences between groups were assessed using a non-

parametric Kruskal-Wallis test with post-hoc Conover-Iman tests for multiple comparisons. Comparisons with p-values < 0.05 were considered significant.
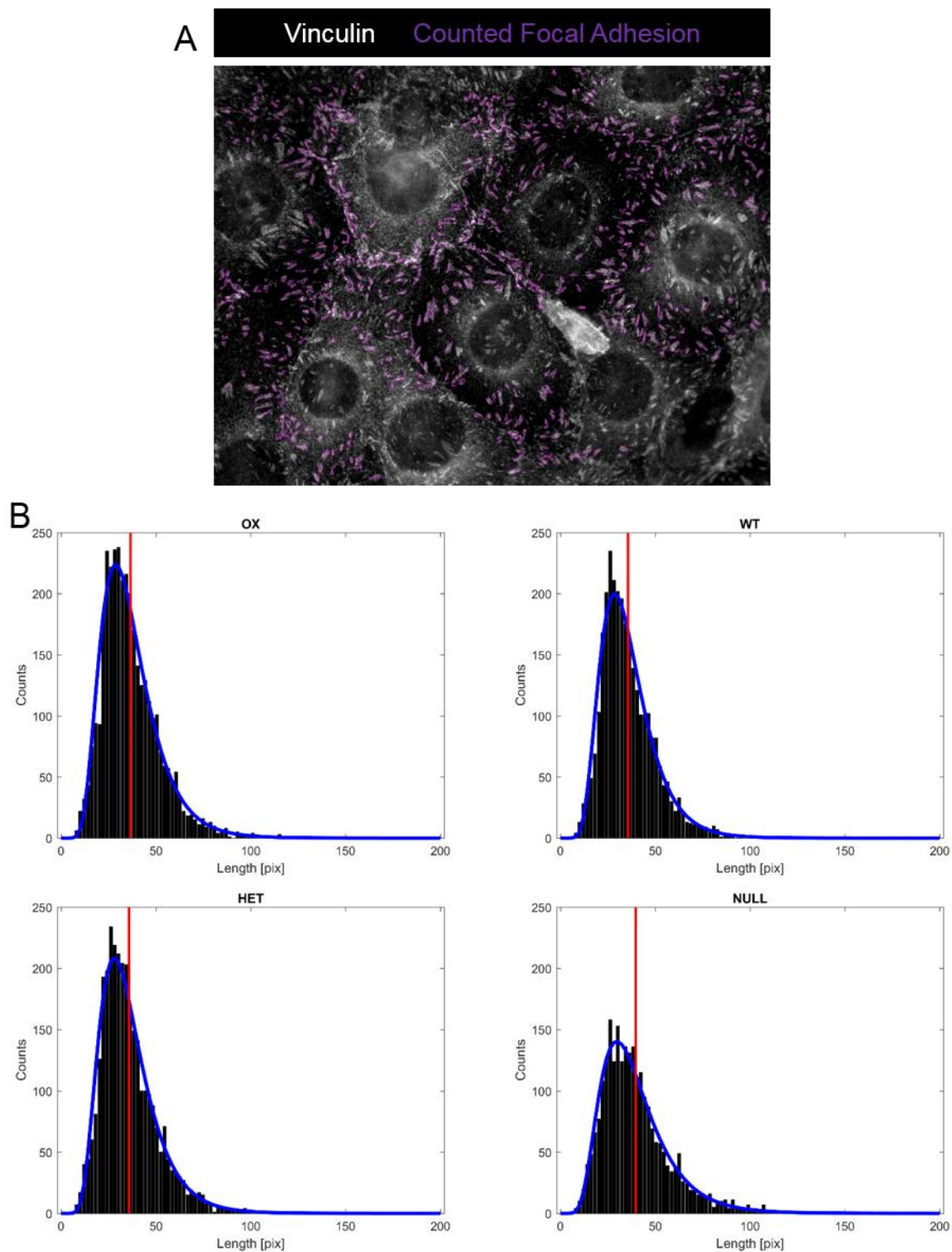
Figure C.1 – Quantification of focal adhesion length and number from immunofluorescence. Vinculin-stained AVICs imaged at 60X were processed with custom code to identify focal adhesions, as outlined in purple (**A**). Lognormal fits (in blue) and means (in red) were identified for each AVIC line (**B**).

APPENDIX D

Generation of the CDH11^{OX} Lines

Generation of the CDH11^{OX} Lines

Vector Design. Human CDH11 was cloned from PC-3 cells (ATCC CRL-1435) with introduction of a NotI site upstream of the start codon and a BamHI site after the stop codon. This was then subcloned into TA cloning vector pGEM-T-EASY. After sequence confirmation, the CDH11 was amplified with an AgeI site added on the 3' end with stop codon disruption and inserted again into TA cloning vector pGEM-T-EASY. After screening of clones, the human CDH11 cDNA was excised with SacII and AgeI and inserted into SacII/AgeI cut pLL-Cherry in frame with the mCherry tag. This vector was verified with sequencing (Figure D.1A).

AVIC Infection. After transfection into HEK293FT cells with the VSV-G and pAX2 vectors to produce viral particles, supernatants were harvested and concentrated using LentiX Concentrator (Clontech 631232). WT AVICs were exposed to the concentrated viral particles and then sorted for mCherry-positive cells via FACS (Figure D.1B). This population was then run in a western blot and stained for CDH11. The CDH11^{OX} line displays the expected ~120 kDa endogenous CDH11 band and a ~140 kDa band that is the expected molecular weight with the added mCherry tag (~28 kDa alone) (Figure D.1C). Also note that the CDH11$^{+/-}$ and CDH11$^{-/-}$ lines display a band at ~100 kDa, consistent with the non-functional form's molecular weight [209]. Proper localization was confirmed by immunofluorescence whereby unstained cells were imaged with a TxRed filter on an Olympus BX53 microscope. The pLL-CDH11-mCherry construct is properly trafficked to the cell membrane, where it appears to participate in adherens junctions with neighboring cells (Figure D.1D). Additionally, cells stained for CDH11 show co-

localization with the mCherry tag (Figure D.1E). These data demonstrate successful infection

and localization of mCherry-tagged CDH11 indicative of normal function.
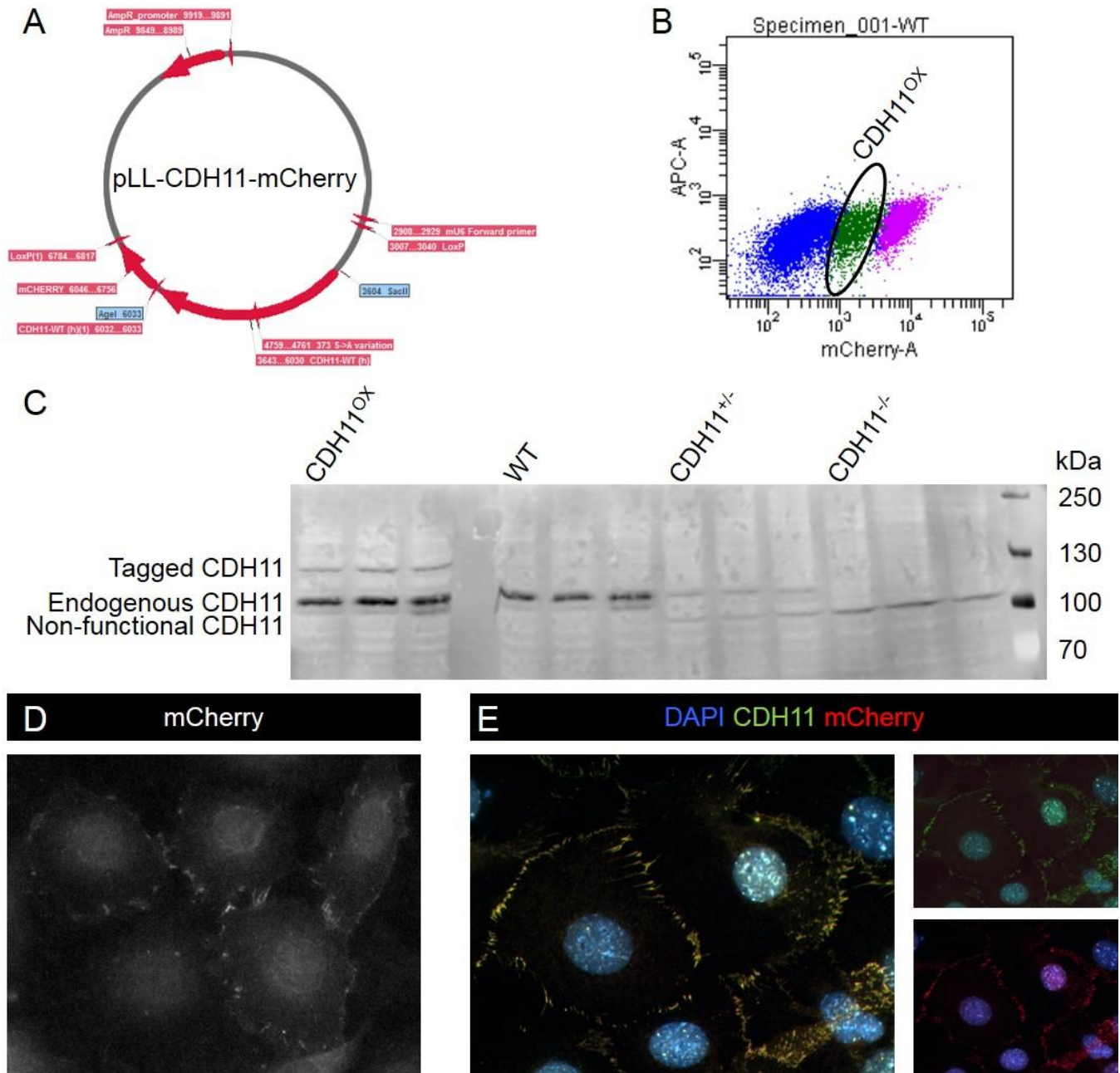
Figure D.1 – Strategy for and validation of CDH11^{OX} generation. Human CDH11 was cloned into a pLL-mCherry plasmid (**A**) and then infected into WT AVICs. FACS sorting for mCherry-positive cells (**B**) yielded a population of WT AVICs overexpressing CDH11. Infection (**C**) and localization (**D-E**) were validated via western blot and immunofluorescence, respectively.

REFERENCES

1. Benjamin, E.J., et al., *Heart Disease and Stroke Statistics-2018 Update: A Report From the American Heart Association.* Circulation, 2018.

2. Reece, T.B., et al., *Rethinking the ross procedure in adults.* The Annals of thoracic surgery, 2014. **97**(1): p. 175-81.

3. Reinohl, J., et al., *Effect of Availability of Transcatheter Aortic-Valve Replacement on Clinical Practice.* The New England journal of medicine, 2015. **373**(25): p. 2438-47.

4. Nkomo, V.T., et al., *Burden of valvular heart diseases: a population-based study.* Lancet, 2006. **368**(9540): p. 1005-11.

5. Osnabrugge, R.L., et al., *Aortic stenosis in the elderly: disease prevalence and number of candidates for transcatheter aortic valve replacement: a meta-analysis and modeling study.* Journal of the American College of Cardiology, 2013. **62**(11): p. 1002-12.

6. Danielsen, R., et al., *The prevalence of aortic stenosis in the elderly in Iceland and predictions for the coming decades: the AGES-Reykjavik study.* International journal of cardiology, 2014. **176**(3): p. 916-22.

7. Rajamannan, N.M., et al., *Calcific aortic valve disease: not simply a degenerative process: A review and agenda for research from the National Heart and Lung and Blood Institute Aortic Stenosis Working Group. Executive summary: Calcific aortic valve disease-2011 update.* Circulation, 2011. **124**(16): p. 1783-91.

8. Coffey, S., B. Cox, and M.J. Williams, *The prevalence, incidence, progression, and risks of aortic valve sclerosis: a systematic review and meta-analysis.* Journal of the American College of Cardiology, 2014. **63**(25 Pt A): p. 2852-61.

9. Association, A.H. *Options for Heart Valve Replacement.* 2016 [cited 2018 February 15]; Available from: http://www.heart.org/HEARTORG/Conditions/More/HeartValveProblemsandDisease/Options-for-Heart-Valve-Replacement_UCM_450816_Article.jsp#.WoZUXFWnGUI.

10. Rosenhek, R., et al., *Statins but not angiotensin-converting enzyme inhibitors delay progression of aortic stenosis.* Circulation, 2004. **110**(10): p. 1291-5.

11. Novaro, G.M., et al., *Effect of hydroxymethylglutaryl coenzyme a reductase inhibitors on the progression of calcific aortic stenosis.* Circulation, 2001. **104**(18): p. 2205-9.

12. Bellamy, M.F., et al., *Association of cholesterol levels, hydroxymethylglutaryl coenzyme-A reductase inhibitor treatment, and progression of aortic stenosis in the community.* Journal of the American College of Cardiology, 2002. **40**(10): p. 1723-30.

13. Kumbhani, D.J., *Simvastatin and Ezetimibe in Aortic Stenosis (SEAS).* The American College of Cardiology's Cardiosource, 2008.

14. Rosenhek, R., *The controversial indications for ACE-Inhibitors in valvular heart disease.* E-Journal of Cardiology Practice, 2005. **4**(13).

15. Bull, S., et al., *A prospective, double-blind, randomized controlled trial of the angiotensin-converting enzyme inhibitor Ramipril In Aortic Stenosis (RIAS trial).* European heart journal cardiovascular Imaging, 2015. **16**(8): p. 834-41.

16.   Thanassoulis, G., *Lipoprotein (a) in calcific aortic valve disease: from genomics to novel drug target for aortic stenosis.* Journal of Lipid Research, 2016. **57**(6): p. 917-24.

17.   Thanassoulis, G., *Early Aortic Valve Lipoprotein(a) Lowering Trial (EAVaLL)*, 2016, NIH.

18.   Chen, J.J., et al., *CT angiography of the cardiac valves: normal, diseased, and postoperative appearances.* Radiographics : a review publication of the Radiological Society of North America, Inc, 2009. **29**(5): p. 1393-412.

19.   Kapelouzou, A., et al., *Serum and tissue biomarkers in aortic stenosis.* Global cardiology science & practice, 2015. **2015**(4): p. 49.

20.   Small, A., et al., *Biomarkers of Calcific Aortic Valve Disease.* Arteriosclerosis, thrombosis, and vascular biology, 2017. **37**(4): p. 623-632.

21.   Cowell, S.J., et al., *A randomized trial of intensive lipid-lowering therapy in calcific aortic stenosis.* The New England journal of medicine, 2005. **352**(23): p. 2389-97.

22.   Imai, K., et al., *C-Reactive protein predicts severity, progression, and prognosis of asymptomatic aortic valve stenosis.* American Heart Journal, 2008. **156**(4): p. 713-8.

23.   Novaro, G.M., et al., *Clinical factors, but not C-reactive protein, predict progression of calcific aortic-valve disease: the Cardiovascular Health Study.* Journal of the American College of Cardiology, 2007. **50**(20): p. 1992-8.

24.   Kubota, N. and D. David Messika-Zeitoun, *P650Influence of fetunin-a level on progression of calcific aortic valve stenosis The COFRASA - GENERAC Study.* European heart journal cardiovascular Imaging, 2016. **17**(suppl_2): p. ii130-ii136.

25.   Bowler, M.A. and W.D. Merryman, *In vitro models of aortic valve calcification: solidifying a system.* Cardiovasc Pathol, 2015. **24**(1): p. 1-10.

26.   Arjunon, S., et al., *Aortic valve: mechanical environment and mechanobiology.* Ann Biomed Eng, 2013. **41**(7): p. 1331-46.

27.   Schroer, A.K. and W.D. Merryman, *Mechanobiology of myofibroblast adhesion in fibrotic cardiac disease.* J Cell Sci, 2015. **128**(10): p. 1865-75.

28.   Center, U.o.M.M. *U.S. Aortic Stenosis Disease Prevalence & Treatment Statistics*. 2013; Available from: http://umm.edu/programs/services/heart-center-programs/cardiothoracic-surgery/valve-surgery/facts.

29.   Roger, V.L., et al., *Heart disease and stroke statistics--2012 update: a report from the American Heart Association.* Circulation, 2012. **125**(1): p. e2-e220.

30.   Lindroos, M., et al., *Prevalence of aortic valve abnormalities in the elderly: an echocardiographic study of a random population sample.* J Am Coll Cardiol, 1993. **21**(5): p. 1220-5.

31.   Aging, A.o., *Projected Future Growth of the Older Population*, D.o.H.H. Services, Editor 2000.

32.   Hermans, H., et al., *Statins for calcific aortic valve stenosis: into oblivion after SALTIRE and SEAS? An extensive review from bench to bedside.* Curr Probl Cardiol, 2010. **35**(6): p. 284-306.

33.   Kodali, S.K., et al., *Two-year outcomes after transcatheter or surgical aortic-valve replacement.* N Engl J Med, 2012. **366**(18): p. 1686-95.

34.   Li, C., S. Xu, and A.I. Gotlieb, *The progression of calcific aortic valve disease through injury, cell dysfunction, and disruptive biologic and physical force feedback loops.* Cardiovasc Pathol, 2013. **22**(1): p. 1-8.

35. Chester, A.H. and P.M. Taylor, *Molecular and functional characteristics of heart-valve interstitial cells.* Philos Trans R Soc Lond B Biol Sci, 2007. **362**(1484): p. 1437-43.

36. Ku, C.H., et al., *Collagen synthesis by mesenchymal stem cells and aortic valve interstitial cells in response to mechanical stretch.* Cardiovasc Res, 2006. **71**(3): p. 548-56.

37. Cloyd, K.L., et al., *Characterization of porcine aortic valvular interstitial cell 'calcified' nodules.* PLoS One, 2012. **7**(10): p. e48154.

38. Jian, B., et al., *Progression of aortic valve stenosis: TGF-beta1 is present in calcified aortic valve cusps and promotes aortic valve interstitial cell calcification via apoptosis.* Ann Thorac Surg, 2003. **75**(2): p. 457-65; discussion 465-6.

39. Rajamannan, N.M., et al., *Human aortic valve calcification is associated with an osteoblast phenotype.* Circulation, 2003. **107**(17): p. 2181-4.

40. Guerraty, M. and E.R. Mohler III, *Models of aortic valve calcification.* J Investig Med, 2007. **55**(6): p. 278-83.

41. Mohler, E.R., 3rd, et al., *Bone formation and inflammation in cardiac valves.* Circulation, 2001. **103**(11): p. 1522-8.

42. Monzack, E.L. and K.S. Masters, *Can valvular interstitial cells become true osteoblasts? A side-by-side comparison.* J Heart Valve Dis, 2011. **20**(4): p. 449-63.

43. Chen, J.H. and C.A. Simmons, *Cell-matrix interactions in the pathobiology of calcific aortic valve disease: critical roles for matricellular, matricrine, and matrix mechanics cues.* Circ Res, 2011. **108**(12): p. 1510-24.

44. Kaden, J.J., et al., *Inflammatory regulation of extracellular matrix remodeling in calcific aortic valve stenosis.* Cardiovasc Pathol, 2005. **14**(2): p. 80-7.

45. Yip, C.Y., et al., *Calcification by valve interstitial cells is regulated by the stiffness of the extracellular matrix.* Arterioscler Thromb Vasc Biol, 2009. **29**(6): p. 936-42.

46. Gu, X. and K.S. Masters, *Regulation of valvular interstitial cell calcification by adhesive peptide sequences.* J Biomed Mater Res A, 2010. **93**(4): p. 1620-30.

47. Hutcheson, J.D., et al., *Cadherin-11 regulates cell-cell tension necessary for calcific nodule formation by valvular myofibroblasts.* Arterioscler Thromb Vasc Biol, 2013. **33**(1): p. 114-20.

48. Walker, G.A., et al., *Valvular myofibroblast activation by transforming growth factor-beta: implications for pathological extracellular matrix remodeling in heart valve disease.* Circ Res, 2004. **95**(3): p. 253-60.

49. Chen, J., et al., *Biophysical analysis of dystrophic and osteogenic models of valvular calcification.* J Biomech Eng, 2015. **137**(2): p. 020903.

50. Wang, H., L.A. Leinwand, and K.S. Anseth, *Roles of transforming growth factor-beta1 and OB-cadherin in porcine cardiac valve myofibroblast differentiation.* FASEB J, 2014. **28**(10): p. 4551-62.

51. Liu, A.C., V.R. Joag, and A.I. Gotlieb, *The emerging role of valve interstitial cell phenotypes in regulating heart valve pathobiology.* Am J Pathol, 2007. **171**(5): p. 1407-18.

52. Paruchuri, S., et al., *Human pulmonary valve progenitor cells exhibit endothelial/mesenchymal plasticity in response to vascular endothelial growth factor-A and transforming growth factor-beta2.* Circ Res, 2006. **99**(8): p. 861-9.

53. Balachandran, K., et al., *Cyclic strain induces dual-mode endothelial-mesenchymal transformation of the cardiac valve.* Proc Natl Acad Sci U S A, 2011. **108**(50): p. 19943-8.

54.   Sewell-Loftin, M.K., et al., *Myocardial contraction and hyaluronic acid mechanotransduction in epithelial-to-mesenchymal transformation of endocardial cells.* Biomaterials, 2014. **35**(9): p. 2809-15.

55.   Mohler, E.R., 3rd, et al., *Identification and characterization of calcifying valve cells from human and canine aortic valves.* J Heart Valve Dis, 1999. **8**(3): p. 254-60.

56.   Kaden, J.J., et al., *Expression of bone sialoprotein and bone morphogenetic protein-2 in calcific aortic stenosis.* J Heart Valve Dis, 2004. **13**(4): p. 560-6.

57.   Cheng, S.L., et al., *Msx2 promotes osteogenesis and suppresses adipogenic differentiation of multipotent mesenchymal progenitors.* Journal of Biological Chemistry, 2003. **278**(46): p. 45969-45977.

58.   Yang, X.P., et al., *Bone morphogenic protein 2 induces Runx2 and osteopontin expression in human aortic valve interstitial cells: Role of Smad1 and extracellular signal-regulated kinase 1/2.* Journal of Thoracic and Cardiovascular Surgery, 2009. **138**(4): p. 1008-1015.

59.   Chen, J.H., et al., *Identification and characterization of aortic valve mesenchymal progenitor cells with robust osteogenic calcification potential.* Am J Pathol, 2009. **174**(3): p. 1109-19.

60.   Wang, H., et al., *Characterization of cell subpopulations expressing progenitor cell markers in porcine cardiac valves.* PLoS One, 2013. **8**(7): p. e69667.

61.   Deck, J.D., *Endothelial cell orientation on aortic valve leaflets.* Cardiovasc Res, 1986. **20**(10): p. 760-7.

62.   Manduteanu, I., et al., *Calf Cardiac Valvular Endothelial-Cells in Culture - Production of Glycosaminoglycans, Prostacyclin and Fibronectin.* Journal of Molecular and Cellular Cardiology, 1988. **20**(2): p. 103-118.

63.   Nathan, C., *Nitric-Oxide as a Secretory Product of Mammalian-Cells.* Faseb Journal, 1992. **6**(12): p. 3051-3064.

64.   Gossl, M., et al., *Role of Circulating Osteogenic Progenitor Cells in Calcific Aortic Stenosis (vol 60, pg 1945, 2012).* Journal of the American College of Cardiology, 2012. **60**(24): p. 1945-1953.

65.   Egan, K.P., et al., *Role for Circulating Osteogenic Precursor Cells in Aortic Valvular Disease.* Arteriosclerosis Thrombosis and Vascular Biology, 2011. **31**(12): p. 2965-2971.

66.   Freeman, R.V. and C.M. Otto, *Spectrum of calcific aortic valve disease - Pathogenesis, disease progression, and treatment strategies.* Circulation, 2005. **111**(24): p. 3316-3326.

67.   Cote, N., et al., *Inflammation Is Associated with the Remodeling of Calcific Aortic Valve Disease.* Inflammation, 2013. **36**(3): p. 573-581.

68.   New, S.E.P. and E. Aikawa, *Molecular Imaging Insights Into Early Inflammatory Stages of Arterial and Aortic Valve Calcification.* Circulation Research, 2011. **108**(11): p. 1381-1391.

69.   Wallby, L., et al., *Inflammatory Characteristics of Stenotic Aortic Valves: A Comparison between Rheumatic and Nonrheumatic Aortic Stenosis.* Cardiol Res Pract, 2013: p. 895215.

70.   Chang, M.Y., et al., *Oxidized low density lipoproteins regulate synthesis of monkey aortic smooth muscle cell proteoglycans that have enhanced native low density lipoprotein binding properties.* Journal of Biological Chemistry, 2000. **275**(7): p. 4766-4773.

71.   Swindle, M.M., et al., *Swine as models in biomedical research and toxicology testing.* Vet Pathol, 2012. **49**(2): p. 344-56.

72.   de Smet, B.J., et al., *The atherosclerotic Yucatan animal model to study the arterial response after balloon angioplasty: the natural history of remodeling.* Cardiovasc Res, 1998. **39**(1): p. 224-32.

73.   Simmons, C.A., et al., *Spatial heterogeneity of endothelial phenotypes correlates with side-specific vulnerability to calcification in normal porcine aortic valves.* Circ Res, 2005. **96**(7): p. 792-9.

74.   Johnson, C.M., M.N. Hanson, and S.C. Helgeson, *Porcine cardiac valvular subendothelial cells in culture: cell isolation and growth characteristics.* J Mol Cell Cardiol, 1987. **19**(12): p. 1185-93.

75.   Mulholland, D.L. and A.I. Gotlieb, *Cell biology of valvular interstitial cells.* Can J Cardiol, 1996. **12**(3): p. 231-6.

76.   Wang, L., et al., *Factors influencing the oxygen consumption rate of aortic valve interstitial cells: application to tissue engineering.* Tissue Eng Part C Methods, 2009. **15**(3): p. 355-63.

77.   Cushing, M.C., J.T. Liao, and K.S. Anseth, *Activation of valvular interstitial cells is mediated by transforming growth factor-beta 1 interactions with matrix molecules.* Matrix Biology, 2005. **24**(6): p. 428-437.

78.   Pho, M., et al., *Cofilin is a marker of myofibroblast differentiation in cells from porcine aortic cardiac valves.* Am J Physiol Heart Circ Physiol, 2008. **294**(4): p. H1767-78.

79.   Clark-Greuel, J.N., et al., *Transforming growth factor-beta1 mechanisms in aortic valve calcification: increased alkaline phosphatase and related events.* Ann Thorac Surg, 2007. **83**(3): p. 946-53.

80.   Kim, K.M., et al., *Calcification in aging canine aortic valve.* Scan Electron Microsc, 1986(Pt 3): p. 1151-6.

81.   Aupperle, H. and S. Disatian, *Pathology, protein expression and signaling in myxomatous mitral valve degeneration: comparison of dogs and humans.* J Vet Cardiol, 2012. **14**(1): p. 59-71.

82.   Hsu, H.H., O. Tawfik, and F. Sun, *Mechanism of dystrophic calcification in rabbit aortas: temporal and spatial distributions of calcifying vesicles and calcification-related structural proteins.* Cardiovasc Pathol, 2004. **13**(1): p. 3-10.

83.   Rajamannan, N.M., et al., *Experimental hypercholesterolemia induces apoptosis in the aortic valve.* J Heart Valve Dis, 2001. **10**(3): p. 371-4.

84.   Hsu, H.H., et al., *Induction of calcification in rabbit aortas by high cholesterol diets: roles of calcifiable vesicles in dystrophic calcification.* Atherosclerosis, 2002. **161**(1): p. 85-94.

85.   Swiatek, P.J., et al., *Notch1 is essential for postimplantation development in mice.* Genes Dev, 1994. **8**(6): p. 707-19.

86.   Nus, M., et al., *Diet-induced aortic valve disease in mice haploinsufficient for the Notch pathway effector RBPJK/CSL.* Arterioscler Thromb Vasc Biol, 2011. **31**(7): p. 1580-8.

87.   Hjortnaes, J., et al., *Arterial and aortic valve calcification inversely correlates with osteoporotic bone remodelling: a role for inflammation.* Eur Heart J, 2010. **31**(16): p. 1975-84.

88.   Nakashima, Y., et al., *ApoE-deficient mice develop lesions of all phases of atherosclerosis throughout the arterial tree.* Arterioscler Thromb, 1994. **14**(1): p. 133-40.

89.   Sanan, D.A., et al., *Low density lipoprotein receptor-negative mice expressing human apolipoprotein B-100 develop complex atherosclerotic lesions on a chow diet: no accentuation by apolipoprotein(a).* Proc Natl Acad Sci U S A, 1998. **95**(8): p. 4544-9.

90.   Awan, Z., et al., *The LDLR deficient mouse as a model for aortic calcification and quantification by micro-computed tomography.* Atherosclerosis, 2011. **219**(2): p. 455-62.

91.   Treuting, P.M. and S.M. Dintzis, *Comparative Anatomy and Histology: A Mouse and Human Atlas*. 1 ed2011: Elsevier.

92.   Branchetti, E., et al., *Antioxidant enzymes reduce DNA damage and early activation of valvular interstitial cells in aortic valve sclerosis.* Arterioscler Thromb Vasc Biol, 2013. **33**(2): p. e66-74.

93.   Galeone, A., et al., *Aortic valvular interstitial cells apoptosis and calcification are mediated by TNF-related apoptosis-inducing ligand.* Int J Cardiol, 2013. **169**(4): p. 296-304.

94.   Kaden, J.J., et al., *Receptor activator of nuclear factor kappaB ligand and osteoprotegerin regulate aortic valve calcification.* J Mol Cell Cardiol, 2004. **36**(1): p. 57-66.

95.   Kaden, J.J., et al., *Influence of receptor activator of nuclear factor kappa B on human aortic valve myofibroblasts.* Exp Mol Pathol, 2005. **78**(1): p. 36-40.

96.   Latif, N., et al., *Expression of smooth muscle cell markers and co-activators in calcified aortic valves.* Eur Heart J, 2014.

97.   Yang, X., et al., *Pro-osteogenic phenotype of human aortic valve interstitial cells is associated with higher levels of Toll-like receptors 2 and 4 and enhanced expression of bone morphogenetic protein 2.* J Am Coll Cardiol, 2009. **53**(6): p. 491-500.

98.   Yu, Z., et al., *Tumor necrosis factor-alpha accelerates the calcification of human aortic valve interstitial cells obtained from patients with calcific aortic valve stenosis via the BMP2-Dlx5 pathway.* J Pharmacol Exp Ther, 2011. **337**(1): p. 16-23.

99.   Zeng, Q., et al., *Cross-talk between the Toll-like receptor 4 and Notch1 pathways augments the inflammatory response in the interstitial cells of stenotic human aortic valves.* Circulation, 2012. **126**(11 Suppl 1): p. S222-30.

100.   Lommi, J.I., et al., *High-density lipoproteins (HDL) are present in stenotic aortic valves and may interfere with the mechanisms of valvular calcification.* Atherosclerosis, 2011. **219**(2): p. 538-44.

101.   Acharya, A., et al., *Inhibitory role of Notch1 in calcific aortic valve disease.* PLoS One, 2011. **6**(11): p. e27743.

102.   Benton, J.A., H.B. Kern, and K.S. Anseth, *Substrate properties influence calcification in valvular interstitial cell culture.* J Heart Valve Dis, 2008. **17**(6): p. 689-99.

103.   Benton, J.A., et al., *Statins block calcific nodule formation of valvular interstitial cells by inhibiting alpha-smooth muscle actin expression.* Arterioscler Thromb Vasc Biol, 2009. **29**(11): p. 1950-7.

104.   Butcher, J.T. and R.M. Nerem, *Porcine aortic valve interstitial cells in three-dimensional culture: Comparison of phenotype with aortic smooth muscle cells.* Journal of Heart Valve Disease, 2004. **13**(3): p. 478-485.

105.   Butcher, J.T. and R.M. Nerem, *Valvular endothelial cells regulate the phenotype of interstitial cells in co-culture: effects of steady shear stress.* Tissue Eng, 2006. **12**(4): p. 905-15.

106.   Fisher, C.I., J. Chen, and W.D. Merryman, *Calcific nodule morphogenesis by heart valve interstitial cells is strain dependent.* Biomech Model Mechanobiol, 2013. **12**(1): p. 5-17.

107.   Hutcheson, J.D., et al., *5-HT(2B) antagonism arrests non-canonical TGF-beta1-induced valvular myofibroblast differentiation.* J Mol Cell Cardiol, 2012. **53**(5): p. 707-14.

108.   Kennedy, J.A., et al., *Inhibition of calcifying nodule formation in cultured porcine aortic valve cells by nitric oxide donors.* Eur J Pharmacol, 2009. **602**(1): p. 28-35.

109.   Richards, J., et al., *Side-specific endothelial-dependent regulation of aortic valve calcification: interplay of hemodynamics and nitric oxide signaling.* Am J Pathol, 2013. **182**(5): p. 1922-31.

110

110.   Tseng, H., et al., *A three-dimensional co-culture model of the aortic valve using magnetic levitation.* Acta Biomater, 2014. **10**(1): p. 173-82.

111.   Yip, C.Y., et al., *Inhibition of pathological differentiation of valvular interstitial cells by C-type natriuretic peptide.* Arterioscler Thromb Vasc Biol, 2011. **31**(8): p. 1881-9.

112.   Cai, Z.J., et al., *Endoplasmic Reticulum Stress Participates in Aortic Valve Calcification in Hypercholesterolemic Animals.* Arteriosclerosis Thrombosis and Vascular Biology, 2013. **33**(10): p. 2345-2354.

113.   Merryman, W.D., et al., *Viscoelastic properties of the aortic valve interstitial cell.* J Biomech Eng, 2009. **131**(4): p. 041005.

114.   Merryman, W.D., et al., *Correlation between heart valve interstitial cell stiffness and transvalvular pressure: implications for collagen biosynthesis.* Am J Physiol Heart Circ Physiol, 2006. **290**(1): p. H224-31.

115.   Connolly, J.M., et al., *Triglycidylamine crosslinking of porcine aortic valve cusps or bovine pericardium results in improved biocompatibility, biomechanics, and calcification resistance: chemical and biological mechanisms.* Am J Pathol, 2005. **166**(1): p. 1-13.

116.   Shao, J.S., et al., *Msx2 promotes cardiovascular calcification by activating paracrine Wnt signals.* J Clin Invest, 2005. **115**(5): p. 1210-20.

117.   Rajamannan, N.M., et al., *Atorvastatin inhibits hypercholesterolemia-induced calcification in the aortic valves via the Lrp5 receptor pathway.* Circulation, 2005. **112**(9 Suppl): p. I229-34.

118.   Schroer, A.K., L.M. Ryzhova, and W.D. Merryman, *Network Modeling Approach to Predict Myofibroblast Differentiation.* Cellular and Molecular Bioengineering, 2014. **7**(3): p. 446-459.

119.   Rusanescu, G., R. Weissleder, and E. Aikawa, *Notch signaling in cardiovascular disease and calcification.* Curr Cardiol Rev, 2008. **4**(3): p. 148-56.

120.   Chang, S.K., et al., *Cadherin-11 regulates fibroblast inflammation.* Proc Natl Acad Sci U S A, 2011. **108**(20): p. 8402-7.

121.   Kawaguchi, H., et al., *Distinct effects of PPARgamma insufficiency on bone marrow cells, osteoblasts, and osteoclastic cells.* J Bone Miner Metab, 2005. **23**(4): p. 275-9.

122.   Rajamannan, N.M., et al., *Atorvastatin inhibits calcification and enhances nitric oxide synthase production in the hypercholesterolaemic aortic valve.* Heart, 2005. **91**(6): p. 806-10.

123.   Wipff, P.J., et al., *Myofibroblast contraction activates latent TGF-beta1 from the extracellular matrix.* J Cell Biol, 2007. **179**(6): p. 1311-23.

124.   Cushing, M.C., et al., *Fibroblast growth factor represses Smad-mediated myofibroblast activation in aortic valvular interstitial cells.* FASEB J, 2008. **22**(6): p. 1769-77.

125.   Sewell-Loftin, M.K., et al., *A novel technique for quantifying mouse heart valve leaflet stiffness with atomic force microscopy.* J Heart Valve Dis, 2012. **21**(4): p. 513-20.

126.   Merryman, W.D., et al., *The effects of cellular contraction on aortic valve leaflet flexural stiffness.* J Biomech, 2006. **39**(1): p. 88-96.

127.   Haskett, D., et al., *Microstructural and biomechanical alterations of the human aorta as a function of age and location.* Biomech Model Mechanobiol, 2010. **9**(6): p. 725-36.

128.   Merryman, W.D., *Mechano-potential etiologies of aortic valve disease.* Journal of Biomechanics, 2010. **43**(1): p. 87-92.

129.   Akat, K., M. Borggrefe, and J.J. Kaden, *Aortic valve calcification: basic science to clinical practice.* Heart, 2009. **95**(8): p. 616-23.

130.   Cooke, J.P., *Flow, NO, and atherogenesis.* Proc Natl Acad Sci U S A, 2003. **100**(3): p. 768-70.

131.   Ng, C.P., B. Hinz, and M.A. Swartz, *Interstitial fluid flow induces myofibroblast differentiation and collagen alignment in vitro.* J Cell Sci, 2005. **118**(Pt 20): p. 4731-9.

132.   Kunz-Schughart, L.A., et al., *Three-dimensional tissue structure affects sensitivity of fibroblasts to TGF-beta 1.* Am J Physiol Cell Physiol, 2003. **284**(1): p. C209-19.

133.   Balachandran, K., et al., *Elevated cyclic stretch induces aortic valve calcification in a bone morphogenic protein-dependent manner.* Am J Pathol, 2010. **177**(1): p. 49-57.

134.   Simmons, C.A., et al., *Mechanical stimulation and mitogen-activated protein kinase signaling independently regulate osteogenic differentiation and mineralization by calcifying vascular cells.* J Biomech, 2004. **37**(10): p. 1531-41.

135.   Merryman, W.D., et al., *Synergistic effects of cyclic tension and transforming growth factor-beta1 on the aortic valve myofibroblast.* Cardiovasc Pathol, 2007. **16**(5): p. 268-76.

136.   Institute, M. *Cadherins.* MB Info 2014 October 2014 [cited 2016 February]; Available from: http://www.mechanobio.info/modules/go-0007155/04_go-0007155.

137.   Ilvesaro, J.M., P.T. Lakkakorpi, and H.K. Vaananen, *Inhibition of bone resorption in vitro by a peptide containing the cadherin cell adhesion recognition sequence HAV is due to prevention of sealing zone formation.* Exp Cell Res, 1998. **242**(1): p. 75-83.

138.   Hanakawa, Y., et al., *Different effects of dominant negative mutants of desmocollin and desmoglein on the cell-cell adhesion of keratinocytes.* J Cell Sci, 2000. **113 (Pt 10)**: p. 1803-11.

139.   Tanoue, T. and M. Takeichi, *New insights into Fat cadherins.* J Cell Sci, 2005. **118**(Pt 11): p. 2347-53.

140.   Morishita, H. and T. Yagi, *Protocadherin family: diversity, structure, and function.* Curr Opin Cell Biol, 2007. **19**(5): p. 584-92.

141.   Oas, R.G., et al., *p120-catenin and beta-catenin differentially regulate cadherin adhesive function.* Mol Biol Cell, 2013. **24**(6): p. 704-14.

142.   Benjamin, J.M., et al., *AlphaE-catenin regulates actin dynamics independently of cadherin-mediated cell-cell adhesion.* J Cell Biol, 2010. **189**(2): p. 339-52.

143.   Silvis, M.R., et al., *alpha-catenin is a tumor suppressor that controls cell accumulation by regulating the localization and activity of the transcriptional coactivator Yap1.* Sci Signal, 2011. **4**(174): p. ra33.

144.   Nanes, B.A., et al., *p120-catenin binding masks an endocytic signal conserved in classical cadherins.* The Journal of cell biology, 2012. **199**(2): p. 365-80.

145.   Anastasiadis, P.Z., et al., *Inhibition of RhoA by p120 catenin.* Nat Cell Biol, 2000. **2**(9): p. 637-44.

146.   Perez, T.D., et al., *Immediate-early signaling induced by E-cadherin engagement and adhesion.* J Biol Chem, 2008. **283**(8): p. 5014-22.

147.   Shewan, A.M., et al., *Myosin 2 is a key Rho kinase target necessary for the local concentration of E-cadherin at cell-cell contacts.* Mol Biol Cell, 2005. **16**(10): p. 4531-42.

148.   Klezovitch, O. and V. Vasioukhin, *Cadherin signaling: keeping cells in touch.* F1000Res, 2015. **4**(F1000 Faculty Rev): p. 550.

149. Vinyoles, M., et al., *Multivesicular GSK3 sequestration upon Wnt signaling is controlled by p120-catenin/cadherin interaction with LRP5/6.* Mol Cell, 2014. **53**(3): p. 444-57.

150. Ortiz, A., et al., *Angiomotin is a novel component of cadherin-11/beta-catenin/p120 complex and is critical for cadherin-11-mediated cell migration.* FASEB J, 2015. **29**(3): p. 1080-91.

151. Noss, E.H., et al., *Evidence for cadherin-11 cleavage in the synovium and partial characterization of its mechanism.* Arthritis research & therapy, 2015. **17**: p. 126.

152. McGuire, J.K., Q. Li, and W.C. Parks, *Matrilysin (matrix metalloproteinase-7) mediates E-cadherin ectodomain shedding in injured lung epithelium.* The American journal of pathology, 2003. **162**(6): p. 1831-43.

153. Ribeiro, A.S., et al., *Extracellular cleavage and shedding of P-cadherin: a mechanism underlying the invasive behaviour of breast cancer cells.* Oncogene, 2010. **29**(3): p. 392-402.

154. Herren, B., et al., *Cleavage of beta-catenin and plakoglobin and shedding of VE-cadherin during endothelial apoptosis: evidence for a role for caspases and metalloproteinases.* Molecular biology of the cell, 1998. **9**(6): p. 1589-601.

155. Steinhusen, U., et al., *Cleavage and shedding of E-cadherin after induction of apoptosis.* The Journal of biological chemistry, 2001. **276**(7): p. 4972-80.

156. Noe, V., et al., *Release of an invasion promoter E-cadherin fragment by matrilysin and stromelysin-1.* Journal of cell science, 2001. **114**(Pt 1): p. 111-118.

157. McCusker, C., et al., *Extracellular cleavage of cadherin-11 by ADAM metalloproteases is essential for Xenopus cranial neural crest cell migration.* Molecular biology of the cell, 2009. **20**(1): p. 78-89.

158. Gama, A. and F. Schmitt, *Cadherin cell adhesion system in canine mammary cancer: a review.* Veterinary medicine international, 2012. **2012**: p. 357187.

159. Dakshanamurthy, S., et al., *Predicting new indications for approved drugs using a proteochemometric method.* J Med Chem, 2012. **55**(15): p. 6832-48.

160. Chen, J., et al., *Notch1 Mutation Leads to Valvular Calcification Through Enhanced Myofibroblast Mechanotransduction.* Arteriosclerosis, thrombosis, and vascular biology, 2015. **35**(7): p. 1597-605.

161. Sung, D.C., et al., *Cadherin-11 Overexpression Induces Extracellular Matrix Remodeling and Calcification in Mature Aortic Valves.* Arteriosclerosis, thrombosis, and vascular biology, 2016. **36**(8): p. 1627-37.

162. Okazaki, M., et al., *Molecular cloning and characterization of OB-cadherin, a new member of cadherin family expressed in osteoblasts.* J Biol Chem, 1994. **269**(16): p. 12092-8.

163. Uhlen, M., et al., *Proteomics. Tissue-based map of the human proteome.* Science, 2015. **347**(6220): p. 1260419.

164. Uhlen, M., et al., *Towards a knowledge-based Human Protein Atlas.* Nature biotechnology, 2010. **28**(12): p. 1248-50.

165. Assefnia, S., et al., *Cadherin-11 in poor prognosis malignancies and rheumatoid arthritis: common target, common therapies.* Oncotarget, 2014. **5**(6): p. 1458-74.

166. Pittet, P., et al., *Fibrogenic fibroblasts increase intercellular adhesion strength by reinforcing individual OB-cadherin bonds.* J Cell Sci, 2008. **121**(Pt 6): p. 877-86.

167. Langhe, R.P., et al., *Cadherin-11 localizes to focal adhesions and promotes cell-substrate adhesion.* Nature communications, 2016. **7**: p. 10909.

168.   Oh, E.S., A. Woods, and J.R. Couchman, *Syndecan-4 proteoglycan regulates the distribution and activity of protein kinase C.* The Journal of biological chemistry, 1997. **272**(13): p. 8133-6.

169.   Longley, R.L., et al., *Control of morphology, cytoskeleton and migration by syndecan-4.* Journal of cell science, 1999. **112 (Pt 20)**: p. 3421-31.

170.   Woods, A., et al., *Syndecan-4 binding to the high affinity heparin-binding domain of fibronectin drives focal adhesion formation in fibroblasts.* Archives of Biochemistry and Biophysics, 2000. **374**(1): p. 66-72.

171.   Garg, V., et al., *Mutations in NOTCH1 cause aortic valve disease.* Nature, 2005. **437**(7056): p. 270-4.

172.   Hadji, F., et al., *Altered DNA Methylation of Long Noncoding RNA H19 in Calcific Aortic Valve Disease Promotes Mineralization by Silencing NOTCH1.* Circulation, 2016. **134**(23): p. 1848-1862.

173.   Pedersen, B.K., A. Steensberg, and P. Schjerling, *Muscle-derived interleukin-6: possible biological effects.* The Journal of physiology, 2001. **536**(Pt 2): p. 329-37.

174.   Burgmaier, M., et al., *Serum levels of C-peptide are associated with coronary artery calcification in patients with rheumatoid arthritis.* Rheumatology international, 2015. **35**(9): p. 1541-7.

175.   Kjaergaard, A.D., et al., *Role of inflammatory marker YKL-40 in the diagnosis, prognosis and cause of cardiovascular and liver diseases.* Critical reviews in clinical laboratory sciences, 2016. **53**(6): p. 396-408.

176.   Tran, H.T., et al., *Chitinase 3-like 1 synergistically activates IL6-mediated STAT3 phosphorylation in intestinal epithelial cells in murine models of infectious colitis.* Inflammatory bowel diseases, 2014. **20**(5): p. 835-46.

177.   Dubinski, A. and Z. Zdrojewicz, *[The role of interleukin-6 in development and progression of atherosclerosis].* Polski merkuriusz lekarski : organ Polskiego Towarzystwa Lekarskiego, 2007. **22**(130): p. 291-4.

178.   Nishimoto, N., *Interleukin-6 in rheumatoid arthritis.* Current opinion in rheumatology, 2006. **18**(3): p. 277-81.

179.   Smith, P.C., et al., *Interleukin-6 and prostate cancer progression.* Cytokine & growth factor reviews, 2001. **12**(1): p. 33-40.

180.   Emery, P., et al., *IL-6 receptor inhibition with tocilizumab improves treatment outcomes in patients with rheumatoid arthritis refractory to anti-tumour necrosis factor biologicals: results from a 24-week multicentre randomised placebo-controlled trial.* Annals of the rheumatic diseases, 2008. **67**(11): p. 1516-23.

181.   Nishimoto, N., et al., *Humanized anti-interleukin-6 receptor antibody treatment of multicentric Castleman disease.* Blood, 2005. **106**(8): p. 2627-32.

182.   Yokota, S., et al., *Efficacy and safety of tocilizumab in patients with systemic-onset juvenile idiopathic arthritis: a randomised, double-blind, placebo-controlled, withdrawal phase III trial.* Lancet, 2008. **371**(9617): p. 998-1006.

183.   Ozawa, Y., et al., *Regulation of posttranscriptional modification as a possible therapeutic approach for retinal neuroprotection.* Journal of Ophthalmology, 2011. **2011**: p. 506137.

184.   Byon, C.H., et al., *Oxidative stress induces vascular calcification through modulation of the osteogenic transcription factor Runx2 by AKT signaling.* J Biol Chem, 2008. **283**(22): p. 15319-27.

185.   Liberman, M., et al., *Oxidant generation predominates around calcifying foci and enhances progression of aortic valve calcification.* Arterioscler Thromb Vasc Biol, 2008. **28**(3): p. 463-70.

186.   Miller, J.D., et al., *Dysregulation of antioxidant mechanisms contributes to increased oxidative stress in calcific aortic valvular stenosis in humans.* J Am Coll Cardiol, 2008. **52**(10): p. 843-50.

187.   Al-Aly, Z., et al., *Aortic Msx2-Wnt calcification cascade is regulated by TNF-alpha-dependent signals in diabetic Ldlr-/- mice.* Arterioscler Thromb Vasc Biol, 2007. **27**(12): p. 2589-96.

188.   Caira, F.C., et al., *Human degenerative valve disease is associated with up-regulation of low-density lipoprotein receptor-related protein 5 receptor-mediated bone formation.* J Am Coll Cardiol, 2006. **47**(8): p. 1707-12.

189.   Bertazzo, S., et al., *Nano-analytical electron microscopy reveals fundamental insights into human cardiovascular tissue calcification.* Nature Materials, 2013. **12**(6): p. 576-83.

190.   Otero, E.U., et al., *Raman spectroscopy for diagnosis of calcification in human heart valves.* Spectroscopy-an International Journal, 2004. **18**(1): p. 75-84.

191.   Tzang, O., et al., *Detection of microcalcification in tissue with Raman spectroscopy.* Cardiovascular Engineering and Technology, 2011. **2**(3): p. 228-33.

192.   Brockbank, K.G. and Y.C. Song, *Mechanisms of bioprosthetic heart valve calcification.* Transplantation, 2003. **75**(8): p. 1133-5.

193.   Chemistry, R.S.o. *Atomic absorption spectroscopy.* [cited 2014 07]; Available from: http://www.kau.edu.sa/Files/130002/Files/6785_AAs.pdf.

194.   Gregory, C.A., et al., *An Alizarin red-based assay of mineralization by adherent cells in culture: comparison with cetylpyridinium chloride extraction.* Anal Biochem, 2004. **329**(1): p. 77-84.

195.   Utah, U.o. *von Kossa's Method - Calcium.* [cited 2014 07]; Available from: http://library.med.utah.edu/WebPath/HISTHTML/MANUALS/VONKOSSA.PDF.

196.   Bonewald, L.F., et al., *von Kossa staining alone is not sufficient to confirm that mineralization in vitro represents bone formation.* Calcif Tissue Int, 2003. **72**(5): p. 537-47.

197.   Rungby, J., et al., *The von Kossa reaction for calcium deposits: silver lactate staining increases sensitivity and reduces background.* Histochem J, 1993. **25**(6): p. 446-51.

198.   ThermoScientific. *Calcium Reagent Arsenazo III.* 2010 [cited 2014 07].

199.   Janssen, J.W. and A.R. Helbing, *Arsenazo III: an improvement of the routine calcium determination in serum.* Eur J Clin Chem Clin Biochem, 1991. **29**(3): p. 197-201.

200.   Coulter, B. *Calcium oCPC.* 2009 [cited 2014 07]; Available from: https://www.beckmancoulter.com/wsrportal/techdocs?docname=/cis/BAOSR6x13/%25%25/EN_CALCIUM%20(oCPC).pdf.

201.   Delogne, C., et al., *Characterization of the calcification of cardiac valve bioprostheses by environmental scanning electron microscopy and vibrational spectroscopy.* J Microsc, 2007. **228**(Pt 1): p. 62-77.

202.   Erni, R., et al., *Atomic-resolution imaging with a sub-50-pm electron probe.* Phys Rev Lett, 2009. **102**(9): p. 096101.

203.   Hafner, B. *Energy Dispersive Spectroscopy on the SEM: A Primer.* [cited 2014 07]; Available from: http://www.charfac.umn.edu/instruments/eds_on_sem_primer.pdf.

204.   abcam. *Alkaline Phosphatase Assay Kit (Colorimetric) ab83369.* [cited 2014 07]; Available from: http://www.abcam.com/alkaline-phosphatase-assay-kit-colorimetric-ab83369.html.

205. Grases, F., O. Sohnel, and M. Zelenkova, *Ultrafine structure of human aortic valve calcific deposits.* J Cytol Histol, 2014. **5**(2): p. 214.

206. Jastrzebska, M., et al., *Supramolecular structure of human aortic valve and pericardial xenograft material: atomic force microscopy study.* J Mater Sci Mater Med, 2008. **19**(1): p. 249-56.

207. Merryman, W.D. and C.R. Clark, *Lnc-ing NOTCH1 to Idiopathic Calcific Aortic Valve Disease.* Circulation, 2016. **134**(23): p. 1863-1865.

208. Clark, C.R., et al., *Targeting Cadherin-11 Prevents Notch1-Mediated Calcific Aortic Valve Disease.* Circulation, 2017. **135**(24): p. 2448-2450.

209. Kawaguchi, J., et al., *Targeted disruption of cadherin-11 leads to a reduction in bone density in calvaria and long bone metaphyses.* Journal of bone and mineral research : the official journal of the American Society for Bone and Mineral Research, 2001. **16**(7): p. 1265-71.

210. Horikawa, K., et al., *Adhesive subdivisions intrinsic to the epithelial somites.* Developmental biology, 1999. **215**(2): p. 182-9.

211. Wienert, S., et al., *Detection and segmentation of cell nuclei in virtual microscopy images: a minimum-model approach.* Scientific reports, 2012. **2**: p. 503.

212. Schneider, C.A., W.S. Rasband, and K.W. Eliceiri, *NIH Image to ImageJ: 25 years of image analysis.* Nature methods, 2012. **9**(7): p. 671-5.

213. Han, S.J., et al., *Traction microscopy to identify force modulation in subresolution adhesions.* Nature methods, 2015. **12**(7): p. 653-6.

214. Jerrell, R.J. and A. Parekh, *Cellular traction stresses mediate extracellular matrix degradation by invadopodia.* Acta biomaterialia, 2014. **10**(5): p. 1886-96.

215. Sabass, B., et al., *High resolution traction force microscopy based on experimental and computational advances.* Biophysical journal, 2008. **94**(1): p. 207-20.

216. Dembo, M. and Y.L. Wang, *Stresses at the cell-to-substrate interface during locomotion of fibroblasts.* Biophysical journal, 1999. **76**(4): p. 2307-16.

217. Butler, J.P., et al., *Traction fields, moments, and strain energy that cells exert on their surroundings.* American journal of physiology. Cell physiology, 2002. **282**(3): p. C595-605.

218. Alexander, N.R., et al., *Extracellular matrix rigidity promotes invadopodia activity.* Current biology : CB, 2008. **18**(17): p. 1295-1299.

219. Jerrell, R.J. and A. Parekh, *Polyacrylamide gels for invadopodia and traction force assays on cancer cells.* Journal of visualized experiments : JoVE, 2015(95): p. 52343.

220. Hansen, P.C., *Analysis of Discrete Ill-Posed Problems by Means of the L-Curve.* Siam Review, 1992. **34**(4): p. 561-580.

221. Plotnikov, S.V., et al., *High-resolution traction force microscopy.* Methods in cell biology, 2014. **123**: p. 367-94.

222. Schwarz, U.S., et al., *Calculation of forces at focal adhesions from elastic substrate data: the effect of localized force and the need for regularization.* Biophysical journal, 2002. **83**(3): p. 1380-94.

223. Reinhart-King, C.A., M. Dembo, and D.A. Hammer, *The dynamics and mechanics of endothelial cell spreading.* Biophysical journal, 2005. **89**(1): p. 676-89.

224. Maruthamuthu, V., et al., *Cell-ECM traction force modulates endogenous tension at cell-cell contacts.* Proceedings of the National Academy of Sciences of the United States of America, 2011. **108**(12): p. 4708-13.

225. Ltd., M. *Four Parameter Logistic Curve.* [online data analysis tool] [cited 2018 January 22]; Available from: http://www.myassays.com/four-parameter-logistic-curve.assay.

226. Chang, S.K., et al., *Cadherin-11 regulates fibroblast inflammation.* Proceedings of the National Academy of Sciences of the United States of America, 2011. **108**(20): p. 8402-7.

227. Yan, C., et al., *Stat3 downstream gene product chitinase 3-like 1 is a potential biomarker of inflammation-induced lung cancer in multiple mouse lung tumor models and humans.* PLoS One, 2013. **8**(4): p. e61984.

228. Rathcke, C.N. and H. Vestergaard, *YKL-40--an emerging biomarker in cardiovascular disease and diabetes.* Cardiovascular diabetology, 2009. **8**: p. 61.

229. Yokokawa, M., K. Takeyasu, and S.H. Yoshimura, *Mechanical properties of plasma membrane and nuclear envelope measured by scanning probe microscope.* Journal of microscopy, 2008. **232**(1): p. 82-90.

230. Wirrig, E.E., et al., *COX2 inhibition reduces aortic valve calcification in vivo.* Arteriosclerosis, thrombosis, and vascular biology, 2015. **35**(4): p. 938-47.

231. Liu, A.C. and A.I. Gotlieb, *Characterization of cell motility in single heart valve interstitial cells in vitro.* Histol Histopathol, 2007. **22**(8): p. 873-82.

232. Zhang, M., et al., *Rational design of true monomeric and bright photoactivatable fluorescent proteins.* Nature methods, 2012. **9**(7): p. 727-9.

233. Hutcheson, J.D., E. Aikawa, and W.D. Merryman, *Potential drug targets for calcific aortic valve disease.* Nature reviews. Cardiology, 2014. **11**(4): p. 218-31.

234. Luckett-Chastain, L., et al., *IL-6 influences the balance between M1 and M2 macrophages in a mouse model of irritant contact dermatitis.* Journal of Immunology, 2016. **196**.

235. Casella, G., et al., *IL4 induces IL6-producing M2 macrophages associated to inhibition of neuroinflammation in vitro and in vivo.* Journal of Neuroinflammation, 2016. **13**.

236. Nagy, E., et al., *Interferon-gamma Released by Activated CD8(+) T Lymphocytes Impairs the Calcium Resorption Potential of Osteoclasts in Calcified Human Aortic Valves.* The American journal of pathology, 2017. **187**(6): p. 1413-1425.

237. Zhou, L., et al., *IL-6 programs T(H)-17 cell differentiation by promoting sequential engagement of the IL-21 and IL-23 pathways.* Nature immunology, 2007. **8**(9): p. 967-74.

238. Roche. *Research & Development Pipeline.* 2018 February 1, 2018 [cited 2018 February 16]; Available from: https://www.roche.com/research_and_development/who_we_are_how_we_work/pipeline.htm.

239. Soine, J.R., et al., *Model-based traction force microscopy reveals differential tension in cellular actin bundles.* PLoS computational biology, 2015. **11**(3): p. e1004076.

240. Dembo, M., et al., *Imaging the traction stresses exerted by locomoting cells with the elastic substratum method.* Biophysical journal, 1996. **70**(4): p. 2008-22.